



TECHNISCHE
UNIVERSITÄT
WIEN

Vienna University of Technology

DISSERTATION

Unravelling the relationship between surface chemistry and oxygen exchange kinetics of (La,Sr)CoO_{3-δ} thin film cathodes

ausgeführt zum Zwecke der Erlangung des akademischen Grades
eines Doktors der technischen Wissenschaften
unter der Leitung von

Univ. Prof. Dipl.-Phys. Dr. Jürgen Fleig

am Institut für Chemische Technologien und Analytik
im Fachbereich Elektrochemie

eingereicht an der Technischem Universität Wien
von

Dipl.-Ing. Ghislain M. Rupp

Hütteldorferstrasse 131/17
1140 Wien

Wien, 14. Juli 2016

Abstract

Solid oxide fuel cells (SOFCs) are expected to substantially contribute to tomorrow's electrical energy production and may become an important technology to ease the transition from fossil fuels to renewable resources such as biomass. Current applications include combined heating and power (CHP) systems for companies or housing complexes as well as portable power supply and typically operate at 700 – 1000 °C. The high operating temperatures restrict the choice of materials used, complicate production, decrease the durability of the components because of undesired side reactions, and therefore hamper a broad commercialization. However, realization of intermediate temperature SOFCs operating at 400 – 600 °C demands cathode materials that are highly active for the oxygen reduction reaction (ORR). Several mixed ionic electronic conductors (MIECs) including $\text{La}_{0.6}\text{Sr}_{0.4}\text{CoO}_{3-\delta}$ (LSC) prove suitable for this task but suffer from degradation of the electrochemical kinetics when subjected to operating temperatures, even on short-time scales (hours, days). This degradation is correlated to changes of the surface composition and structure and its analysis requires methods that are specifically adapted to the underlying complex chemical phenomena.

In this thesis, relationships between surface cation composition and the kinetics of the ORR of LSC model thin films are revealed. A combination of low energy ion scattering (LEIS) measurements and an innovative approach for determination of the surface stoichiometry of solids by on-line inductively coupled plasma – mass spectrometry (ICP-MS) allowed quantitative determination of the surface termination of these thin films. These experiments showed that formation of a Sr-rich surface layer is an equilibrium property of LSC and that significant Sr diffusion takes place above 550°C. Further, a new tool was developed to manipulate thin film electrode surfaces by deposition of different oxides while in-situ measuring the ORR activity: In-situ Impedance spectroscopy inside a pulsed laser deposition chamber (IPLD). Thus, key parameters influencing the ORR kinetics were found and insights into the degradation mechanism of LSC thin films were gained. Particularly, it could be shown that even a single laser pulse applied to a SrO target, i.e. growth of a 4% fraction of a SrO monolayer on an LSC surface, severely decreases the ORR kinetics. This indicates that only a few sites of as-prepared LSC films are highly active for oxygen exchange and additional Sr cations do not randomly cover the surface but specifically deactivate those active sites. Further, a strong enhancement of the ORR kinetics was found, when decorating the surface with Co-oxides.

As an alternative cathode material $\text{La}_{0.6}\text{Ba}_{0.4}\text{CoO}_{3-\delta}$ (LBC) was investigated. An extraordinarily high catalytic activity for the oxygen exchange was discovered and an in-depth impedance analysis revealed the influence of the dopant size ($\text{Ba}^{2+} > \text{Sr}^{2+}$) in $\text{LaCoO}_{3-\delta}$ on the oxygen exchange activity, chemical capacitance and electronic conductivity.

Finally, the electrochemical properties of a single crystal of $\text{La}_{0.95}\text{Sr}_{0.05}\text{Ga}_{0.95}\text{Mg}_{0.05}\text{O}_{3-\delta}$ (LSGM), one of the most promising electrolyte materials for intermediate SOFC, were analyzed by AC experiments with ion blocking electrode. The excellent agreement between equivalent circuit model and experimental data allowed determination of the ionic and electronic conductivity, the chemical capacitance and the oxygen chemical diffusion coefficient from a single impedance spectrum.

Kurzfassung

Festoxid-Brennstoffzellen sind eine vielversprechende Technologie für die zukünftige Bereitstellung elektrischer Energie, die vor allem den Übergang von fossilen Brennstoffen zu erneuerbaren Energien, wie zum Beispiel Biomasse, erleichtern wird. Anwendung findet die Festoxid-Brennstoffzelle in kombinierten Strom-Wärme Erzeugersystemen für größere Betriebe und Wohnanlagen, sowie in mobilen Stromerzeugern. Die hohe Betriebstemperatur von 700 – 1000 °C limitiert jedoch die Auswahl an eingesetzten Materialien, kompliziert die Produktion und verringert die Lebensdauer der Komponenten aufgrund unerwünschter Nebenreaktionen und behindert so eine breite Vermarktung. Die Entwicklung von Festoxid-Brennstoffzellen mit einer Arbeitstemperatur von 400 – 600 °C verlangt Kathodenmaterialien mit einer hohen Aktivität für die Sauerstoffreduktions-Reaktion (ORR). Einige gemischtleitende Oxide, darunter $\text{La}_{0.6}\text{Sr}_{0.4}\text{CoO}_{3-\delta}$ (LSC), würden diese Anforderung erfüllen aber weisen eine zunehmende Verschlechterung der Sauerstoffaustausch-Kinetik auf, wenn sie auch nur für einen kurzen Zeitraum (Stunden, Tage) Betriebstemperaturen ausgesetzt sind. Diese Verschlechterung wird durch Änderungen der Oberflächenzusammensetzung und Struktur bewirkt und bedarf spezifisch angepasster Analysemethoden für die Aufklärung.

Im Rahmen dieser Arbeit wurde die Beziehung zwischen der Oberflächenkationen-zusammensetzung und der Sauerstoffreduktionskinetik von LSC Dünnschichten untersucht. Eine Kombination von niederenergetischer Ionenstreu-spektroskopie und ein innovativer Ansatz für die Bestimmung der Oberflächenstöchiometrie von Festkörpern mittels online induktiv gekoppelter Plasma Massenspektrometrie (ICP-MS) ermöglichte eine quantitative Bestimmung der Oberflächenterminierung von LSC Dünnschichten und die Kinetik der Kationendiffusion zu untersuchen. Eine Sr-reiche und Co-arme wasserlösliche Terminierung konnte auf frisch abgeschiedenen LSC Dünnschichten dadurch bestimmt werden. Außerdem wurde eine neue Methode für die Manipulation von Dünnschichtoberflächen entwickelt, die gleichzeitig die Messung der Sauerstoffreduktionsaktivität erlaubt: In-situ Impedanzspektroskopie innerhalb einer Laserdepositionsanlage (IPLD). Wichtige Leitparameter für die Sauerstoffreduktionskinetik konnten auf diese Weise ermittelt und Einblicke in den Degradationsmechanismus von LSC Dünnschichten gewonnen werden. Der Beschuss eines SrO Targets mit einem einzigen Laserpuls und die daraus folgende Dekoration der LSC Elektrode mit 4 % einer SrO Monolage führte zu einer beträchtlichen Verschlechterung der Sauerstoffreduktionsaktivität. Aus diesen Experimenten

konnte geschlossen werden, dass nur wenige stark katalytisch aktive Plätze für die elektrochemische Reaktion auf der LSC Oberfläche existieren und diese gezielt von Sr Kationen blockiert werden. Des Weiteren wurde eine starke Verbesserung der Sauerstoffreduktionskinetik durch die gezielte Modifikation der Oberfläche mit Co-Oxiden gefunden.

Als alternatives Kathodenmaterial wurde $\text{La}_{0.6}\text{Ba}_{0.4}\text{CoO}_{3-\delta}$ untersucht. Eine sehr hohe katalytische Aktivität für den Sauerstoffaustausch wurde entdeckt und eine detaillierte Impedanzstudie ermöglichte es, den Einfluss der Dotierelementgröße ($\text{Ba}^{2+} > \text{Sr}^{2+}$) in $\text{LaCoO}_{3-\delta}$ auf die katalytischen Eigenschaften, die chemische Kapazität und die elektronische Leitfähigkeit aufzuzeigen.

Schließlich wurden Einkristalle aus $\text{La}_{0.95}\text{Sr}_{0.05}\text{Ga}_{0.95}\text{Mg}_{0.05}\text{O}_{3-\delta}$ (LSGM), einem vielversprechenden Elektrolytmaterial für SOFCs mit niedrigen Arbeitstemperaturen, mittels Impedanzspektroskopie unter Verwendung von ionisch blockierenden Elektroden charakterisiert. Die hervorragende Übereinstimmung zwischen theoretisch existierenden Ersatzschaltbildmodellen und den experimentell erhaltenen Daten erlaubte es, die ionische und elektronische Leitfähigkeit, die chemische Kapazität und den chemischen Sauerstoffdiffusionskoeffizienten aus einem einzigen Impedanzspektrum zu ermitteln.

Table of contents

Abstract	III
Kurzfassung	V
1 Introduction	1
2 Correlating surface cation composition and thin film microstructure to the electrochemical performance of LSC electrodes	7
2.1 Introduction	7
2.2 Experimental	8
2.2.1 Thin film preparation	8
2.2.2 Electrochemical characterization	9
2.2.3 Chemical characterization	9
2.2.4 Microstructural investigations	10
2.3 Results	11
2.3.1 In-situ ICP-OES on-line analysis	11
2.3.2 Chemical surface composition dependence on preparation	14
2.3.3 Electrochemical performance dependence on preparation	19
2.3.4 Comparison of surface composition and electrochemical properties	21
2.4 Conclusions	24
3 Dynamic etching of soluble surface layers with on-line ICP-MS detection – a novel approach for determination of complex metal oxide surface cation stoichiometry	25
3.1 Introduction	25
3.2 Experimental	27
3.2.1 Reagents and standard solutions	27
3.2.2 Sample synthesis and preparation	27
3.2.3 Instrumentation	28
3.2.4 Dynamic etching procedure with on-line ICP-OES or ICP-MS detection	31
3.3 Results	32
3.3.1 Method development	32
3.3.2 Element selective detection using ICP-MS	34
3.3.3 Analytical performance	35
3.3.4 Analysis of surface treated thin films - comparison with LEIS	38
3.4 Conclusions	41

4	Surface chemistry of $\text{La}_{0.6}\text{Sr}_{0.4}\text{CoO}_{3-\delta}$ thin films and its impact on the oxygen surface exchange resistance	42
4.1	Introduction	42
4.2	Experimental	43
4.2.1	Thin film preparation	43
4.2.2	Microstructural characterization	44
4.2.3	Electrical characterization and annealing	44
4.2.4	Low-energy ion scattering (LEIS)	45
4.2.5	On-line ICP-MS	46
4.3	Results	47
4.3.1	Structural characterization.....	47
4.3.2	Surface cation chemistry and performance of as-deposited LSC thin films	48
4.3.3	Annealing of as-deposited thin films	50
4.3.4	Surface treatment of as-deposited thin films	53
4.3.5	Influence of the termination layer on the ORR.....	57
4.4	Conclusions	61
5	Impedance spectroscopy during PLD revealing large changes of the oxygen reduction activity by small amounts of cations.....	62
5.1	Introduction	62
5.2	Experimental	63
5.2.1	Target preparation and characterization	63
5.2.2	Sample preparation.....	65
5.2.3	Electrochemical characterization - IPLD.....	66
5.2.4	Chemical characterization – ICP and XPS	67
5.3	Results	68
5.4	Conclusions	76
5.5	Appendix	77
5.5.1	Decoration with “La” and “Sr (sc)” and detailed impedance interpretation	77
5.5.2	Decoration with porous LSC to estimate CE influence.....	78
5.5.3	Stability of the LSC electrochemical performance	80
5.5.4	LSC compositions measured by XPS before and after decoration.....	81
5.5.5	LSC surface imaged by FESEM before and after decoration.....	82

6	The superior properties of $\text{La}_{0.6}\text{Ba}_{0.4}\text{CoO}_{3-\delta}$ thin film electrodes for oxygen exchange in comparison to $\text{La}_{0.6}\text{Sr}_{0.4}\text{CoO}_{3-\delta}$	84
6.1	Introduction	84
6.2.	Experimental	85
6.2.1	Thin film preparation	85
6.2.2	Structural characterization.....	86
6.2.3	Electrochemical measurements.....	86
6.3.	Results	87
6.3.1	Structural characterization.....	87
6.3.2	Initial AC measurements and equivalent circuit model	89
6.3.3	Time dependent AC measurements.....	93
6.3.4	Temperature dependent AC measurements	95
6.3.5	$p\text{O}_2$ dependent AC measurements.....	98
6.3.6	Van der Pauw – electronic conductivity.....	101
6.4.	Conclusions	103
7	Electronic and ionic conductivity of $\text{La}_{0.95}\text{Sr}_{0.05}\text{Ga}_{0.95}\text{Mg}_{0.05}\text{O}_{3-\delta}$ (LSGM) single crystals.....	104
7.1	Introduction	104
7.2	Experimental	105
7.2.1	LSGM single crystal synthesis and substrate preparation	105
7.2.2	Sample preparation for AC impedance measurements.....	106
7.2.3	Sample preparation for Hebb-Wagner type polarization	106
7.2.4	Structural characterization.....	107
7.2.5	Sample setup and electrochemical measurements.....	107
7.3	Results	108
7.3.1	Structural characterization.....	108
7.3.2	Equivalent circuit model	109
7.3.3	Temperature dependence of the impedance spectra shape.....	110
7.3.4	Temperature dependence of the materials parameters	114
7.3.5	Oxygen partial pressure dependence	117
7.3.6	Hebb-Wagner type polarization.....	120
7.4	Conclusions	122
8.	Summary	123
	Bibliography	127
	List of abbreviations.....	136

List of symbols.....	138
Scientific publications	140
Conference contributions	142
Curriculum vitae	143
Acknowledgments.....	145

1 Introduction

The world's continuously increasing demand of energy strongly determines politics, economy and research of the 21st century. For the past three centuries the growing energy demand has been satisfied by fossil fuels such as coal, oil and gas. The development of the world's economy since the industrial revolution strongly improved standards of living, life expectancy, infrastructure and communication. At the same time the world population increasingly expanded and also the understanding that these benefits should not be privileges of a few. However, rapid economy growth based on cheap fossil fuels is only possible at the expenses of the environment and firing much of what is left will inevitably lead to an economic and environmental collapse. Hence, new technologies as part of a sustainable energy solution are urgently needed^{1,2}.

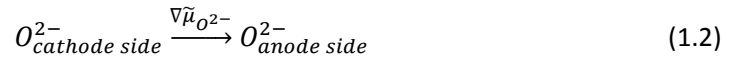
Solid oxide fuel cells (SOFC) are predicted to be part of this new energy era because of their high efficiency for the direct conversion of fuel to electricity. Further, the advantage of fuel flexibility, ranging from pure hydrogen to hydrocarbons or biomass, is one of the most attractive features. SOFCs therefore represent a link between conventional and future electrical energy production. Potential applications include combined heating and power (CHP) systems for companies or housing complexes as well as auxiliary power units (APU) for trucks and airplanes. Another important application in future energy concepts will be a combination with solid oxide electrolysis cells (SOEC) that would also allow to chemically store excess energy produced by wind or solar power plants, since the demand of electrical energy has always to match the supply. Despite all its benefits, SOFC technology is also demanding and a broad commercialization will only be realizable when important key factors such as durability, manufacturing cost and modularization are optimized³⁻⁶.

Solid oxide fuel cells are composed of all solid state materials, usually ceramics. These allow to operate the fuel cells at very high temperatures and primarily characterize the difference between SOFCs and other fuel cell designs. An SOFC can be divided into three components – cathode, electrolyte and anode – as shown in Fig. 1.1. It is continuously supplied by an oxidant (O₂, air) on the cathode side and fuel on the anode side (H₂, CH₄). Gas chamber separation in conventional SOFCs and a gas-tight electrolyte hinder intermixing of the gas supply and build up a chemical oxygen potential μ_{O} gradient across the electrolyte – the driving force for the operation⁷.

Hence, oxygen from the gas is reduced and incorporated at the cathode side



oxygen ions are transported through the electrolyte in a gradient of the oxide ion electrochemical potential $\nabla \tilde{\mu}_{O^{2-}}$



and oxidized by the fuel at the anode side according to



The spatial separation of ionic and electronic charges by the electrolyte allows to direct the electron flow through an external circuit and a consumer. For the application, multiple cells are connected in series by so called interconnects, since a single cell only generates less than 1 V. The interconnect is a critical component that has to fulfill a series of difficult requirements at the same time such as a very high electronic and low ionic conductivity, stability in oxidizing and reducing atmospheres at SOFC operating temperatures and a thermal coefficient similar to the other cell materials⁸. The net reaction of the SOFC when using hydrogen as fuel is exothermic and shows a decreasing efficiency for increasing temperatures. However, higher operating temperatures are necessary to increase the reaction kinetics and lower polarization and ohmic cell losses.

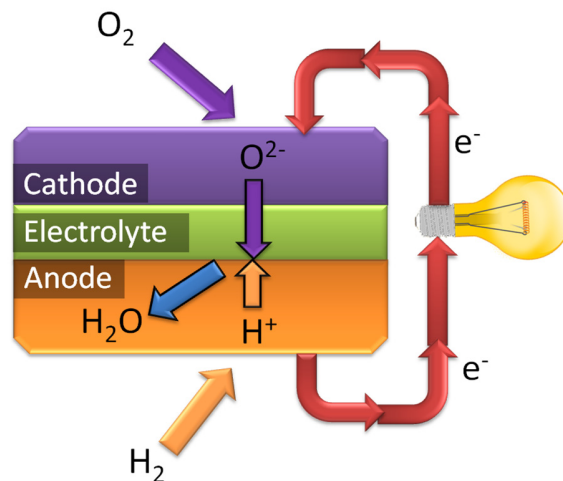


Fig. 1.1 Working principle of an solid oxide fuel cell.

The complete SOFC cell design depends on the conditions for the application such as the type of fuel, stationary or mobile application, required minimum lifetime, size constrictions. Small quantities of anode-supported (by SOFCpower SPA⁹, Kyocera¹⁰, Delphi¹¹), electrolyte-supported (by Bloom Energy¹², Staxera-Sunfire¹³, cathode-supported (by Siemens-Westinghouse¹⁴) and metal-supported (by Ceres Power¹⁵) cells have been introduced to the market and are mostly under permanent supervision for further optimization. Most of these developed SOFCs are operated between 700 – 1000 °C and consist of similar materials: An yttria stabilized zirconia (YSZ) and/or gadolinium doped ceria (GDC) electrolyte, a porous Ni-YSZ cermet anode and a porous strontium doped lanthanum manganite (LSM) cathode. The high operating temperatures restrict the choice of materials used, complicate production, decrease the durability of the components because of undesired side reactions and therefore hinder a broad commercialization. Hence, SOFC research strongly focuses on the reduction of the operating temperatures.

An investigation on a state of the art SOFC with a 150 µm thick YSZ electrolyte, a porous Ni-YSZ anode and a porous YSZ-LSM cathode revealed that at 700 °C the cathode overpotential (56 % of the total resistance) limits the power output¹⁶. At lower temperatures the resistive contributions of the LSM cathode to the total resistance increase even further due to the comparatively high activation energy of 1.3 – 1.6 eV¹⁶⁻¹⁸ for the oxygen reduction reaction (ORR), eq 1.1. Hence, to archive the long-time goal of SOFCs operating at intermediate temperatures of 400 – 600 °C new cathode materials and structures have to be developed.

Mixed ionic and electronic conducting (MIEC) perovskite-type oxides such as Ba_{1-x}Sr_xCo_{1-y}Fe_yO_{3-δ} (BSCF)¹⁹, La_{0.6}Sr_{0.4}CoO_{3-δ} (LSC)²⁰, La_{1-x}Sr_xCo_{1-y}Fe_yO_{3-δ} (LSCF)²¹, La_{0.6}Sr_{0.4}FeO_{3-δ} (LSF)²², Sm_{1-x}Sr_xCoO_{3-δ} (SSC)²¹, SrFeO_{3-δ} (SFO)²³, SrTi_{1-y}Fe_yO_{3-δ} (STF)²³ are promising alternatives to the conventionally applied LSM or LSM/YSZ composite cathodes. A major advantage of these materials is their high ionic conductivity that allows oxygen transport within the electrode and therefore extends the electrochemical active area from the previous triple-phase-boundary (LSM-YSZ-air) to the entire surface (electrode-air) of the cathodes. Kyocera, Delphi and Ceres have already made serious advances in the development of SOFCs using LSCF cathodes²⁴. Nonetheless, further improvement is expected by the employment of LSC, SSC or BSCF cathodes, since they show much faster kinetics for the ORR. However, degradation of the electrochemical kinetics under operating conditions currently impede their application and further knowledge on the ORR and the degradation mechanism itself are needed to answer the most prominent questions in SOFC cathode research:

What determines the ORR kinetics and what are the MIEC key properties that influence the ORR?

The simple reaction written in eq. 1.1 is by far more complex than it appears at first glance. Multiple elementary steps are involved in the ORR and a possible reaction pathway for the oxygen incorporation into a MIEC is exemplarily shown in Fig. 1.2. Here, oxygen is adsorbed on the surface in a monodendate coordination, is reduced by a single electron transfer and the superoxide ion is bidendate coordinated before it accepts another electron to form a peroxide ion ($O_2^{2-}(\text{ad})$). Then, reaction occurs with an oxygen vacancy of the MIEC followed by dissociation. The remaining adsorbed oxygen atom is again reduced in two steps before it is also incorporated into the crystal lattice of the cathode material²⁵.

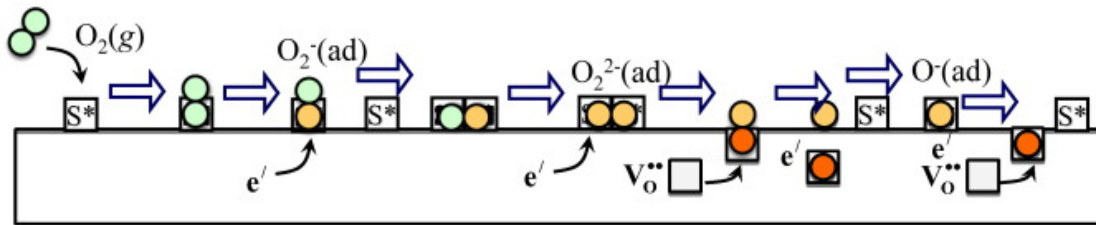


Fig. 1.2 Possible reaction pathway for the oxygen reduction and incorporation reaction of a mixed ionic and electronic conductor (MIEC)²⁵, S^* being adsorption site.

The pathway itself and its sequence should not be taken for granted but rather point out the large variety of involved elementary steps from which each one might determine the ORR. Oxygen partial pressure dependencies of electrode kinetics measured by impedance spectroscopy (IS) or secondary ion mass spectrometry (SIMS) are compared to theoretical rate laws²⁵⁻²⁷, but rarely give unambiguous proves of the rate determining step. A correlation between the ORR kinetics and the ionic conductivity of a large set of different cathode materials (LSM, LSCF, BSCF) was found by R. Merkle, J. Maier and co-workers²⁸. Thus, they proposed that oxygen vacancy concentration and possibly oxygen vacancy migration are involved in the rate determining step. However, almost at the same time W. Jung and H. Tuller found evidence that in fact the charge transfer determines the ORR kinetics by investigating differently doped STF cathodes²³. Further investigations are urgently needed, since understanding of the ORR and its key properties will give guidelines for the development of highly active electrodes and also give knowledge on the degradation mechanism.

What triggers and determines the degradation of the electrochemical kinetics?

Even on a short time scale (hours, days) Sr doped perovskite-type thin film electrodes suffer from a severe decrease of the ORR, which not only impedes the commercialization of such thin film electrodes in devices but also hinders research to deconvolute the complex mechanism of surface exchange in perovskite-type oxide electrodes. Many studies already connected degradation of the electrochemical kinetics to a Sr enrichment in this surface region in various perovskite-type materials such as $(\text{La,Sr})\text{MnO}_{3-\delta}$ ^{29,30}, $(\text{La,Sr})(\text{Co,Fe})\text{O}_{3-\delta}$ ³¹⁻³³, $\text{Sr}(\text{Ti,Fe})\text{O}_{3-\delta}$ ^{34,35} and $(\text{Ba,Sr})(\text{Co,Fe})\text{O}_{3-\delta}$ ³⁶ upon elevated temperatures or polarization of these electrodes. Sr is assumed to segregate to the surface and form SrO/SrOH/SrCO₃, depending on the atmosphere of the annealing conditions, e.g. air or pure O₂. A variety of poisons, such as SO₂, CO₂³⁷⁻³⁹ and Si or Cr sources^{40,41} in the vicinity of a perovskite sample in wet atmosphere, were already shown to enhance the Sr segregation and degradation. However, also in poison-free atmosphere Sr surface segregation takes place. B. Yildiz and co-workers proposed two key driving forces responsible for this phenomena in La_{0.8}Sr_{0.2}MnO_{3-δ} thin films^{42, 43}: Elastic and electrostatic interactions between dopant and perovskite lattice. Elastic driving forces are related to the size mismatch of dopant cations in comparison to the host cation (La³⁺). Larger dopants (Ba²⁺ > Sr²⁺ > Ca²⁺) were found to increase the number of segregated surface particles at elevated temperatures because the lattice “pushes” the cations to the free surface in order to reduce the free energy of the system. Further, a higher oxygen vacancy (V_O^{••}) concentration at the surface of perovskites is predicted by computational studies⁴⁴ and therefore provides an electrostatic driving force for the negatively charged dopants (A_{La}[•]). Primarily, surface sensitive analytical techniques such as X-ray photoelectron spectroscopy (XPS)^{32, 33, 37, 45, 46}, secondary ion mass spectrometry (SIMS)^{31, 47} and low energy ion scattering (LEIS)⁴⁸ have been employed to investigate the surface region of perovskite-type oxides and its influence on the oxygen exchange kinetics. However, quantitative experimental data on the correlation of dopant segregation and ORR kinetics under well-defined electrode and atmosphere conditions are still missing and could give detailed insights into the degradation mechanism.

In this thesis, La_{0.6}Sr_{0.4}CoO_{3-δ} thin film model electrodes were prepared by pulsed laser deposition (PLD) to tackle the open questions raised above. In chapter 2 an innovative approach is presented that allows quantitative determination of the surface stoichiometry of complex metal oxide (CMO) thin films. The procedure is based on treatment of the sample surface with different etching solutions, followed by on-line analysis of the derived eluates using inductively coupled plasma – optical emission spectroscopy (ICP-OES). This method was also successfully applied for

investigations of the degradation mechanism of screen-printed porous LSCF electrodes⁴⁹ (not included in this thesis). Improvements of reproducibility and sensitivity of this method using inductively coupled plasma – mass spectroscopy (ICP-MS), are detailed in chapter 3 and rendered it possible to analyze well-defined dense LSC thin films. In chapter 4, low energy ion scattering (LEIS) technique was used in combination with our optimized technique to reveal important surface properties and cation diffusion kinetics of LSC. This study demonstrates the impact of different LSC surfaces (Sr rich vs. Sr poor) on the ORR kinetics measured by impedance spectroscopy. A novel tool for the investigations of ORR kinetics is presented in chapter 5: In-situ impedance spectroscopy measurements inside the PLD chamber. Here, the LSC thin film surface was deliberately decorated with well-defined fractions of a Sr- Co and La-oxide monolayer by (PLD) while monitoring the ORR by impedance spectroscopy. New insights on how Sr deteriorates the ORR activity and what actually determines the ORR are gained by this very promising technique.

Chapter 6 presents the extraordinarily high catalytic activity for the ORR of an alternative cathode material: $\text{La}_{0.6}\text{Ba}_{0.4}\text{CoO}_{3-\delta}$ (LBC). A comparison to LSC thin films reveals the influence of the A-site dopant size on the catalytic activity for the ORR, chemical capacitance and electronic conductivity. Finally, in chapter 7, $\text{La}_{0.95}\text{Sr}_{0.05}\text{Ga}_{0.95}\text{Mg}_{0.05}\text{O}_{3-\delta}$ (LSGM) single crystals were investigated by AC impedance spectroscopy using ion blocking electrodes. Application of a generalized transmission line model allowed determination of the ionic and electronic conductivity, the chemical capacitance and the oxygen chemical diffusion coefficient from a single impedance spectrum.

2 Correlating surface cation composition and thin film microstructure to the electrochemical performance of LSC electrodes

This chapter contains in large parts material published as a scientific paper in the Journal of Materials Chemistry A⁵⁰.

2.1 Introduction

Different techniques based on electron (auger electron spectroscopy) and ion (secondary ion mass spectrometry) bombardment as well as X-rays (X-ray photoelectron spectroscopy) revealed surface composition changes of perovskites-type materials such as (La,Sr)MnO₃^{29, 51, 52}, (La,Sr)(Co,Fe)O₃^{31-33, 37, 38, 53} and Sr(Ti,Fe)O₃^{34, 54} upon elevated temperatures or polarization. In particular, Sr enrichment was identified and directly linked to a severe decrease of the oxygen reduction reaction activity^{31, 32, 37, 38, 55}. However, the underlying mechanism for the Sr segregation is not fully understood and fundamental questions are still under debate^{42, 56}: What is the dominant driving force of Sr segregation in thin films? Which steps of the oxygen reduction reaction are hindered? Can this effect be avoided? Further high quality measurements are inevitable to deconvolute the complex interrelationships of cathode materials microstructure, bulk and surface chemistry and electrochemical properties. Recently, a novel method to gather quantitative results on the composition of the near-surface region of La_{0.6}Sr_{0.4}CoO_{3-δ} thin films was introduced³¹: An in-situ solid phase extraction system based on chemical etching was coupled with an inductively coupled plasma-optical emission spectrometer (ICP-OES) giving the advantage of on-line cation quantification by a simple liquid standard calibration.

In this chapter, it is first described how this method can be further improved by using different solvents. Then this technique is applied to analyze cation surface segregations of La_{0.6}Sr_{0.4}CoO_{3-δ} thin films of different thicknesses and the results are correlated with electrochemical film properties. Conclusions on chemical composition of surface and bulk are drawn. Moreover, the on-line in-situ ICP-OES analysis method proves to be a useful method for analyzing open porosity and can be an efficient alternative to ellipsometric porosimetry⁵⁷ or high resolution electron imaging techniques⁵⁸ combined with a rather time consuming evaluation of the images

for surface area calculations^{59, 60}. In the context of this chapter the importance of geometrically well-defined electrodes for electrochemical investigations⁶¹ is again emphasized and consequences are pointed out when this prerequisite is not fulfilled.

2.2 Experimental

2.2.1 Thin film preparation

Targets for deposition of LSC thin films by pulsed laser deposition (PLD) were obtained from powders prepared by Pechini synthesis⁶². La_2O_3 , SrCO_3 and Co powders (all Sigma Aldrich, 99.995 %) were individually dissolved in nitric acid, mixed in appropriate ratios and citric acid (TraceSELECT[®], ≥ 99.9998 %) was added for chelation. A calcination step was performed at 1000 °C, followed by isostatically pressing (~ 150 MPa) of the powder to a pellet and a sintering procedure at 1200 °C for 12 hours in air, thus yielding a LSC target for PLD. The target composition was determined from a deposited thin film, which was completely dissolved in $0.12 \text{ mol}\cdot\text{l}^{-1}$ hydrochloric acid and analyzed by non-dynamic ICP-OES. The target composition was determined to be $\text{La}_{0.62\pm 0.02}\text{Sr}_{0.45\pm 0.02}\text{Co}_{0.95\pm 0.04}\text{O}_{3-6}$.

The LSC thin films were deposited onto (100) oriented, one side epipolished yttria stabilized zirconia (YSZ, 9.5 mol% Y_2O_3 , CrysTec GmbH, Germany) single crystals with a thickness of 0.5 mm and a size of $5\times 5 \text{ mm}^2$. Ablation of the target material was carried out by a KrF ($\lambda = 248 \text{ nm}$) excimer laser (Lambda COMPexPro 201F) operated at a pulse repetition rate of 5 Hz, a pulse duration of 50 ns and a laser fluence of approximately $1.5 \text{ J}\cdot\text{cm}^{-2}$ at the target. The substrate temperature was 450 °C according to a pyrometer (Heitronics KT19.99) with the emissivity of YSZ being set to 0.9 for the pyrometer-relevant wavelength range of 9.6 to 14.1 μm . The atmosphere during deposition consisted of 0.4 or 0.04 mbar oxygen, respectively (resulting samples are abbreviated "450^{0.4}" and "450^{0.04}" in the following). The target-substrate distance was varied between 5.2 and 6.2 cm depending on the atmosphere - lower partial pressure lead to a larger plasma plume and thus to a larger target-substrate distance. After deposition, thin films were cooled in the deposition atmosphere at a cooling rate of $12 \text{ }^\circ\text{C}\cdot\text{min}^{-1}$ to avoid crack formation. The LSC thin film thickness was varied by simply adapting the deposition time (pulse count).

2.2.2 Electrochemical characterization

Circular LSC microelectrodes of 200 μm diameter were fabricated by photolithography and subsequent chemical etching ($0.24 \text{ mol}\cdot\text{l}^{-1}$ hydrochloric acid) of the thin films³¹. For the impedance measurements, an alternating voltage of 10 mV (rms) was applied between a microelectrode and an extended counter electrode made from the same LSC film. Any contribution of the counter electrode to the total electrode resistance could be neglected because of its 500-fold larger electrode area. The impedance was measured by a Novocontrol Alpha A High Performance Frequency Analyzer in the frequency range from 10^6 Hz to 10^{-1} Hz with a resolution of five points per decade. All spectra were recorded at 600 °C oven set temperature in air atmosphere. For a more detailed description of the measurement setup see Ref. ²¹.

2.2.3 Chemical characterization

The near-surface composition of the LSC films as well as their bulk composition was determined by continuous analysis of the eluate resulting from chemical etching. $5\times 5\times 0.5 \text{ mm}^3$ YSZ single crystals with continuous LSC films (without micro-patterning) deposited on one side were installed into a custom-made polytetrafluoroethylene etching compartment, Fig. 3.2, with a volume of 289 μl . Thin film layers were then dissolved in a continuous flow of ultrapure water (produced by Barnstead™ Easypure™ II ($18.2 \text{ M}\Omega\cdot\text{cm}^{-1}$)) or hydrochloric acid (EMSURE® hydrochloric acid 37 % for analysis) solutions of different concentrations ($0.006 - 0.024 \text{ mol}\cdot\text{l}^{-1}$ HCl) and concentrations of the dissolved cations were subsequently analyzed. For all analytical measurements, a Thermo Scientific iCAP 6500 ICP spectrometer was employed, equipped with a peristaltic pump for sample introduction, a quartz torch, an echelle spectrometer, and a charge injection device detector. The RF-power was set to 1200 W, pump rotating speed to 15 rpm. A $0.8 \text{ l}\cdot\text{Ar}\cdot\text{min}^{-1}$ auxiliary and a $12 \text{ l}\cdot\text{Ar}\cdot\text{min}^{-1}$ cooling gas flow were applied. The liquid flow was set to $0.6 \text{ ml}\cdot\text{min}^{-1}$ and the nebulizer gas flow to $0.7 \text{ l}\cdot\text{Ar}\cdot\text{min}^{-1}$. A compact sample introduction system (Apex E - elemental scientific) was installed upstream the ICP-OES, containing a heated cyclonic spray chamber and a peltied cooled desolvation system, thus enhancing the efficiency of the sample introduction system. The following background corrected emission lines were chosen for evaluation: Sr (346.446 nm), La (379.478 nm), Co (228.616 nm; 238.892 nm). A maximum integration time of 1 second for the transient signal was chosen.

The schematic procedure of the standard calibration and the actual thin film analysis is shown in Fig. 2.1. A six-port valve allowed proper switching between load and measurement position in both cases. A constant flow of two internal standards ($0.8 \text{ l}\cdot\text{min}^{-1}$ $0.12 \text{ mol}\cdot\text{l}^{-1}$ HCl, spiked with 1 ppm Cu (Cu-Standard Titrisol®), and $0.6 \text{ l}\cdot\text{min}^{-1}$ 0.5 ppm Mn (Mn-Standard, Titrisol®) spiked $0.24 \text{ mol}\cdot\text{l}^{-1}$ HCl) were applied to overcome non-spectral interferences. For standard calibration (l.h.s., load position (green)), a standard solution (mixture of La (ICP-Multi-Element Standard, Aristar®), Co and Sr (both Plasma Emission Standard, Prolabor®) was injected into a sample loop with $333 \mu\text{l}$ volume, whereas the Mn and Cu spiked solutions were redirected to the Apex E. Once the tube was filled completely with the standard solution, the six-port valve was switched (l.h.s. measurement position (red)). The measurement started and the tube content was pushed into the sample introduction system of the ICP-OES.

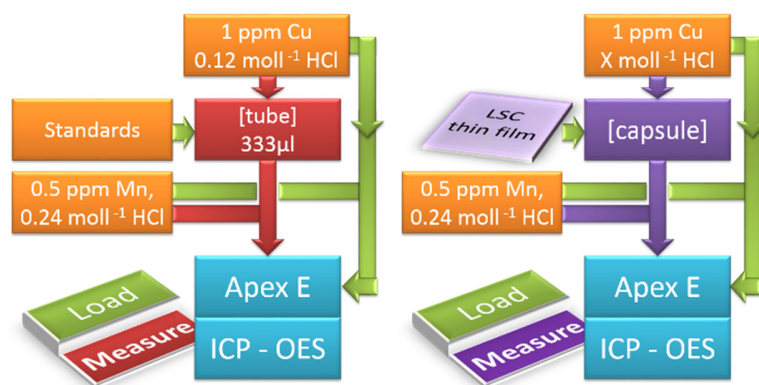


Fig. 2.1 ICP-OES on-line analysis depicting load and measurement position for standard calibration (l.h.s.) and sample analysis (r.h.s.).

2.2.4 Microstructural investigations

Atomic Force Microscopy (AFM) was performed on LSC thin films to analyze the sample topography and to calculate the surface roughness. A Nanoscope® V multimode setup was utilized in tapping mode, equipped with silicon tips. In general, a scan rate of 2 Hz and a resolution of 512×512 pixels over a scan area of $1 \times 1 \mu\text{m}^2$ were chosen. The collected data was evaluated and plotted by Bruker's NanoScope Analysis 1.3 software. A Lyncée Tec Digital Holographic Microscope (DHM) R1101 provided information about the microelectrode thickness and their lateral dimensions. Secondary electron microscopy was performed on a FEI Quanta 200 field emission gun scanning electron microscope equipped with an Everhart-Thornley-Detector. The

microstructure of the thin films was analyzed by Transmission Electron Microscopy (TEM) using an FEI Tecnai F 20 equipped with a field emission gun. Bright field imaging and high angle annular dark field detection (HAADF) were performed at acceleration voltages of 200 kV.

2.3 Results

2.3.1 In-situ ICP-OES on-line analysis

In-situ ICP-OES on-line analysis technique using $0.06 \text{ mol}\cdot\text{l}^{-1}$ hydrochloric acid was already shown to be applicable for investigations of the cation composition of near-surface regions in LSC thin films³¹. First it is demonstrated how to improve the method by exchanging the eluent and/or the eluent concentration and therefore manipulating the solubility of different solid phases. In Fig. 2.2 an ICP-OES etching profile of a freshly deposited $450^{0.4}$ LSC thin film of approx. 160 nm thickness is displayed. During the etching and analysis procedure the eluent was switched several times without interrupting the continuous eluent flux. Fig. 2.2 (top) shows the cation concentration extracted by the different eluents plotted vs. the sum of all the cations detected from the beginning of the measurement (total cation amount). The dominating eluent etching the LSC thin film is also highlighted. An overlap of the different eluent regimes is unavoidable, even for an instantaneous change of the eluent flux from H_2O to $0.012 \text{ mol}\cdot\text{l}^{-1}$ hydrochloric acid (and back). It takes a certain time to completely flush out the previous etching reagent and solute due to wall friction of the tubes and turbulent fluxes in the etching compartment. This is sketched in the top part of Fig. 2.2 but the exact eluent composition during that transition is not known.

A clearer insight into the etching process becomes accessible when relating the calculated molar cation ratio to the total cation amount, Fig. 2.2 (bottom). The first part of the etching profile with ultrapure H_2O is mainly characterized by a high Sr content which will be addressed in detail below, followed by noise due to a strongly decreasing amount of cations in the eluate, partly even below the detection limit. This suggests that only a certain near-surface region of the LSC films is water-soluble. Further this Sr peak endures depending on the etching condition up to 200 seconds. Switching to $0.012 \text{ mol}\cdot\text{l}^{-1}$ hydrochloric acid causes further dissolution of the LSC film and a constant cation composition very close to the LSC target stoichiometry (highlighted by dotted lines) of $\text{La}_{0.58\pm 0.02}\text{Sr}_{0.44\pm 0.04}\text{Co}_{0.97\pm 0.03}\text{O}_{3-\delta}$ is observed. Another change to ultrapure H_2O leads to noise without any significant signal confirming that the water soluble film part is only present at the

surface. The second etching step using diluted hydrochloric acid again reveals the LSC bulk stoichiometry.

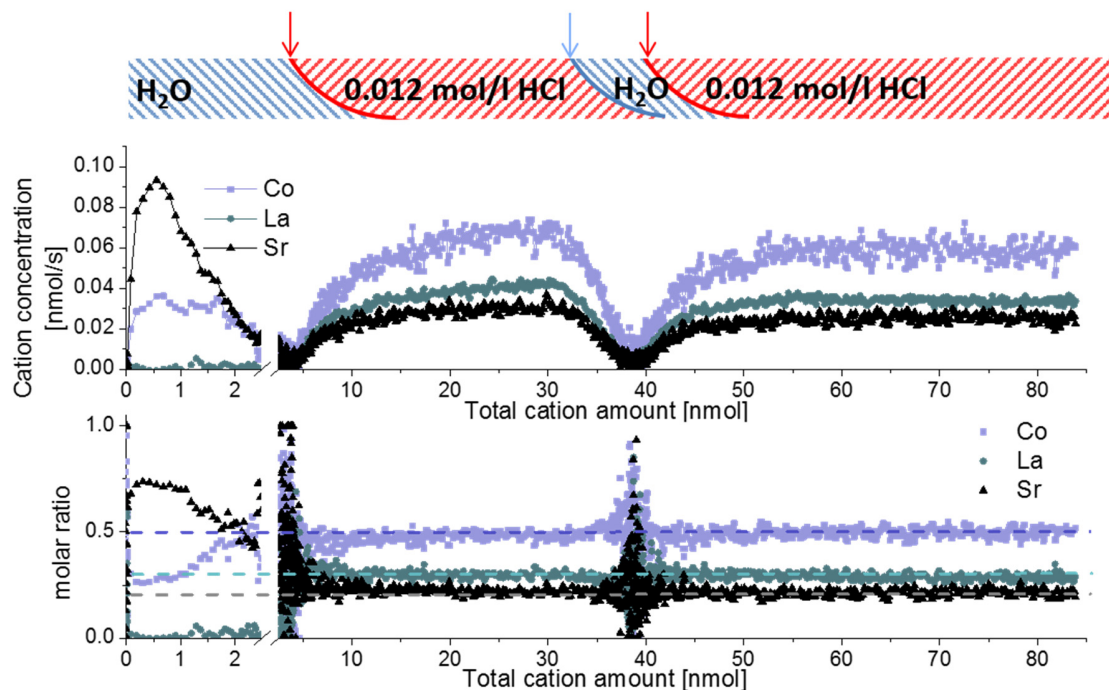


Fig. 2.2 ICP-OES on-line analysis of a $450^{0.4}$ thin film of approx. 160 nm thickness, displaying the concentration of detected cations (top) and the calculated cation molar ratio (bottom) versus the total amount of dissolved cations (corresponding to a depth profile). Applied eluent chronology: H_2O (240 s) \rightarrow 12 $mmol \cdot l^{-1}$ HCl (280 s) \rightarrow H_2O (200 s) \rightarrow 12 $mmol \cdot l^{-1}$ HCl (480 s). The sketch on top displays the sequence of continuous eluent flow, the arrows indicate the moment of eluent change.

Several conclusions can be drawn from these results: 1) a water-soluble surface phase exists on freshly prepared thin films mainly containing Sr but also Co (the latter detected only with low signal to noise ratio); 2) LSC is barely soluble in ultrapure water (below ICP-OES detection limit for La (most sensitive element) in this setup - $20 \mu g \cdot l^{-1}$); 3) preferential dissolution of certain cations of the main LSC phase by hydrochloric acid can be neglected due to the good correspondence of on-line thin film stoichiometry and target stoichiometry. Assuming both a laterally uniform etching process across the whole sample and a dense thin film, one may directly transfer the total cation amount into a thin film depth. For the given example, however, the prerequisite of high density is not fulfilled, see below.

In order to verify that the Sr amount found on the surface is independent of the etch rate and that the amounts determined for ultrapure H_2O are reasonable, another measurement series was conducted: Four freshly deposited $450^{0.4}$ thin films were etched right from the start using 0.006

mol·l⁻¹ HCl, 0.012 mol·l⁻¹ HCl, 0.024 mol·l⁻¹ HCl or ultrapure H₂O, which was exchanged by 0.012 mol·l⁻¹ HCl after 240 seconds. In Fig. 2.3 the amount of Sr found by ICP-OES is plotted against the total cation amount. Linear extrapolation from the range of 15 to 30 nmol to zero cation amount revealed a surplus amount of Sr on the surface. The inset in Fig. 2.3 illustrates that very similar strontium enrichment at the surface, between 1.37 - 1.50 nmol, result for different eluents. Integration of the Sr amount removed from the surface by ultrapure water leads to 1.50 nmol. Hence, all values coincide excellently and pure H₂O can indeed be used to quantify a Sr rich surface phase without dissolving significant amounts of the LSC bulk phase. Based on these results all subsequent ICP-OES measurements were performed using ultrapure water as etching reagent in the beginning, before switching to diluted hydrochloric acid, thus enabling us to separate information on the Sr-rich surface phase from data on LSC bulk material.

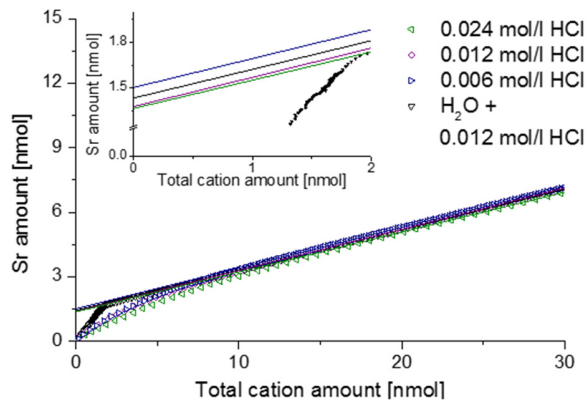


Fig. 2.3 ICP-OES on-line analysis of 450^{0.4} thin films, showing Sr depth profiles depending on the eluent.

2.3.2 Chemical surface composition dependence on preparation

In recent publications it was shown that LSC films prepared at low temperatures can exhibit very low polarization resistances^{31, 63} and that the deposition temperature also affects the amounts of Sr-rich surface phases^{31, 32}. Furthermore it was demonstrated that the microstructure and porosity of $\text{La}_{1-x}\text{Sr}_x\text{Co}_{1-y}\text{Fe}_y\text{O}_{3-\delta}$ (LSCF) films depend on the preparation conditions such as deposition temperature and oxygen partial pressure⁶⁰. In order to further analyze the correlation between Sr segregation, preparation conditions, film porosity and electrochemical properties, two series of $450^{0.4}$ and $450^{0.04}$ thin films of different thicknesses were prepared by pulsed laser deposition. By applying 1,688, 3,375, 6,750 13,500 laser pulses to a LSC64 target film thicknesses of 19 – 127 nm ($450^{0.04}$) and 19 – 167 nm ($450^{0.4}$) resulted. For each deposition pressure and film thickness, four thin films were prepared simultaneously, leading to a total of 32 samples. Two thin films of each of the eight sets were investigated by ICP-OES on-line analysis during chemical etching, one film was used for electrochemical and DHM measurements and one for FESEM and AFM imaging. Owing to problems during photolithography some additional thin films had to be prepared for the impedance measurements and their thickness was once again determined by DHM.

It was not possible to give unambiguous statements on the thin film porosity based on FESEM images, as grain boundaries between the columnar grains are barely distinguishable from cracks and pinholes, see Fig. 2.4. Nevertheless, the visual impression suggested a denser packing of the grains for the $450^{0.04}$ thin films compared to the $450^{0.4}$ thin films.

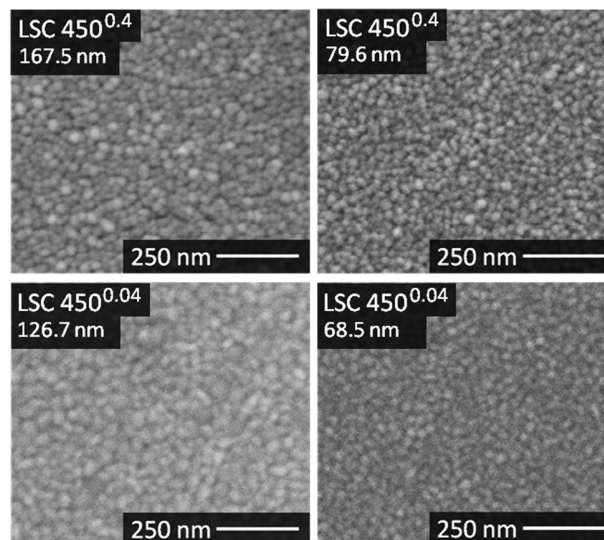


Fig. 2.4 FESEM top-views of the thickest $450^{0.4}$ and $450^{0.04}$ thin films.

The diameter of the LSC columns growing on the substrate surface was estimated from AFM images (Fig. 2.5) and results, together with the roughness, are summarized in Table 2.1. The column diameter increases with increasing film thickness particularly for $450^{0.4}$ thin films, where additionally some protruding grains were found.

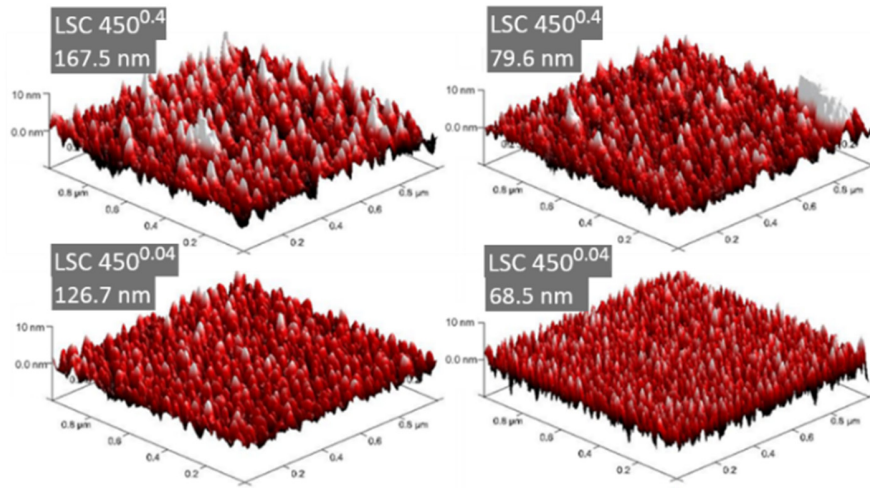


Fig. 2.5 3D-AFM images of the thickest $450^{0.4}$ and $450^{0.04}$ thin films.

Table 2.1 Results of the AFM surface analysis for $450^{0.4}$ and $450^{0.04}$ thin films.

sample type	thickness [nm]	mean grain size [nm]	roughness [nm]	surface / proj. area [%]
$450^{0.4}$	167.5	22.9	2.36	104.96
	79.6	19.1	2.27	104.28
	41.0	14.4	2.12	117.1
	19.3	14.5	1.33	104.96
$450^{0.04}$	126.7	23.9	1.65	103.50
	68.5	16.8	1.94	109,27
	36.4	17.7	1.03	103.24
	19.4	19.8	0.85	102.27

Fig. 2.6 displays etching profiles of all films obtained by ICP-OES and relates the cation molar ratio to the first 20 nmol of total cation amount etched off during the procedure. The time dependence of the Sr amount etched by ultrapure water, and later by HCl, is shown for all films in Fig. 2.7. It can be seen that the Sr removed by ultrapure water levels off after a few ten seconds and the value after 320 seconds (dashed line in Fig. 2.7) was taken as the total amount of strontium extracted by H_2O , i.e. before HCl was added. Results are summarized in Table 2.2.

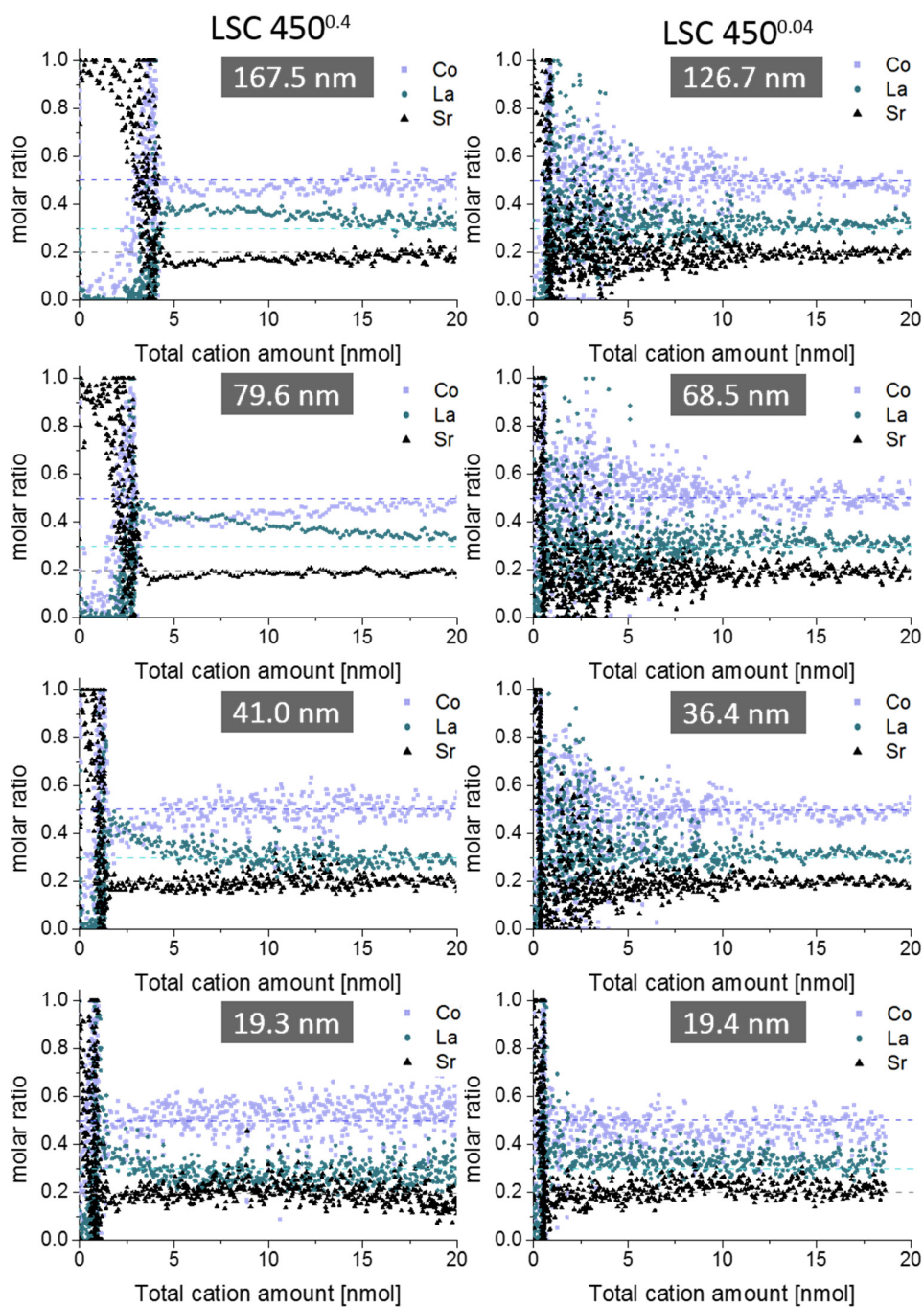


Fig. 2.6 Comparison between ICP-OES on-line depth profiles of differently thin $450^{0.4}$ (l.h.s.) and $450^{0.04}$ films (r.h.s.). Only the first 20 nmol of the total cation amount are displayed, since deviations from the blank bulk stoichiometry (dashed lines) were limited to this depth. Applied eluent chronology: H_2O (200s) \rightarrow $6 \text{ mmol}\cdot\text{l}^{-1}$ HCl (250s) \rightarrow $12 \text{ mmol}\cdot\text{l}^{-1}$ HCl (250s). A compromise had to be reached in terms of eluent concentration in order to obtain sufficient data points per nmol depth for the porous $450^{0.4}$ thin films, and still acceptable noise for the $450^{0.04}$ depth profiles. For the dense $450^{0.04}$ thin film 20 nmol LSC would correspond to a 15.6 nm thick LSC layer.

It is very obvious that for films deposited at 0.4 mbar the Sr amount strongly increases with thickness, between 19.3 nm and 79.6 nm the increase is almost proportional to the film thickness. For films deposited at lower oxygen partial pressures, the variation of Sr amount with film thickness is much smaller and except from the largest thickness even almost negligible. Differences between projected and surface area (Table 2.1) caused by roughness can definitely not explain these differences which therefore deserve further interpretation.

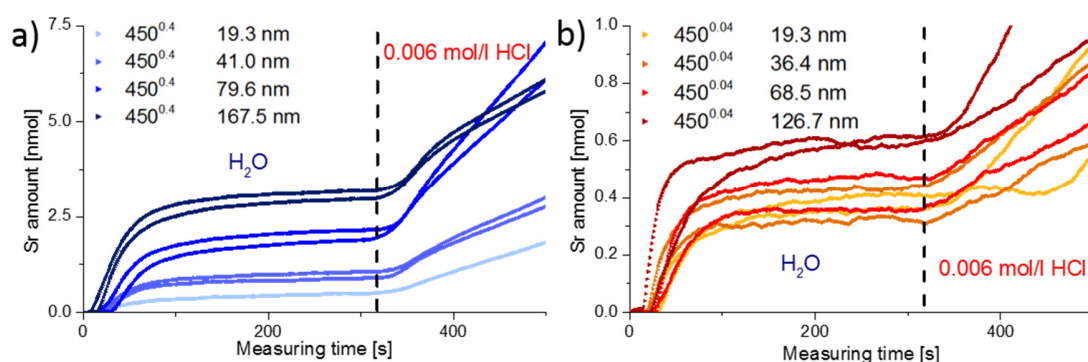


Fig. 2.7 Time-resolved data from spectra of Fig. 2.6. The detected amount of Sr for the 450^{0.4} (a) and 450^{0.04} (b) films of different thicknesses is plotted vs. measuring time. The total water-soluble amount of strontium for each sample is taken from the dashed line and summarized in Table 2.2.

Assuming that the water soluble Sr-enriched phase is homogeneously distributed on the LSC surface it can be expected that the dissolved amount scales with the surface area accessible to the eluent. For films with a porous microstructure the accessible surface area increases with the thickness as long as pores are not closed. This therefore suggests that the much larger Sr amount is due to a six-fold larger surface area for the 167.5nm thick film in comparison to the thinnest 450^{0.4} film. The almost constant Sr amount of 450^{0.04} layers, on the other hand, suggest dense films for lower deposition pressure. Hence, it is concluded that ca. 0.4 nmol Sr exist on a thin film with the lateral dimensions of 0.5 x 0.5 cm².

Based on this considerations it becomes possible to estimate the thickness of the Sr-rich surface phase, provided it homogeneously covers the entire LSC surface. Different heterogeneously or uniformly distributed Sr-rich phases (e.g. SrO, SrOH₂, SrCO₃) were already proposed earlier^{29, 31, 32, 52}. In case of a dense SrO layer covering the entire LSC surface, 0.4 nmol Sr would correspond to 0.32 nm SrO, i.e. 1.2 atomic layers. However, the result could also be interpreted as chemical dissolution of a terminating layer of pure SrO. Assuming the same amount of Sr segregants per area in case of 450^{0.4} layers, our results suggest true surface areas (accessible by the solute) which

are increased due to porosity by a factor of 1.2 for the 19 nm film to 8 for the thickest film, compared to the geometrical sample area. This, however, should also lead to significant differences of the polarization resistances and the corresponding measurements are shown in chapter 2.3.3. As mentioned earlier, also traces of Co were found in the ultrapure H₂O eluate, which suggests that Co is either part of the water soluble Sr-rich phase or forms a second water-soluble phase on top of LSC. Further experiments involving an ICP-MS system and dense LSC thin films are shown in chapter 3 and 4, since the sensitivity of the ICP-OES system is not sufficient to make reliable quantitative statements about the low concentrations of Co (<0.5 mg·l⁻¹) in the H₂O eluate.

Regarding the etching step in HCl, dense thin films suffered from noisy depth profiles, while porous thin films allowed qualitative insights into the first 10 nm of the LSC bulk due to the increased surface area - yielding more cations for detection. In Fig. 2.6, a slight depletion of strontium is found in the near surface region of LSC, removed by 0.006 mol·l⁻¹ HCl acid, which however does by far not correspond to the amount of strontium etched off in the beginning by H₂O. Hence, larger parts of LSC have to be involved in Sr segregation during PLD preparation, which is possible due to sufficiently high cation diffusion coefficients in these thin films, particularly along grain boundaries⁵⁶. Another feature is a Co depletion close to the surface accompanied by a La enrichment thus suggesting a near-surface A-site enrichment (Sr + La)/Co in accordance with XPS measurements³². However, it should be noted that for all thin films the expected LSC stoichiometry is observed after the first 20 nmol of total cation amount.

Table 2.2 Amounts of water-soluble Sr on top of the LSC bulk obtained from data in Fig. 2.7. The 450^{0.4} 19.3 nm thin film was only measured once.

sample type	thickness [nm]	amount of Sr [nmol]
450 ^{0.4}	167.5	3.09 ± 0.14
	79.6	2.03 ± 0.19
	41.0	0.98 ± 0.11
	19.3	0.51
450 ^{0.04}	126.7	0.61 ± 0.01
	68.5	0.42 ± 0.08
	36.4	0.38 ± 0.09
	19.4	0.39 ± 0.03

2.3.3 Electrochemical performance dependence on preparation

AC impedance measurements were carried out on microelectrodes of 200 μm diameter, microstructured by photo-lithography and chemical etching. Several impedance spectra were recorded for each sample to verify reproducibility. Representative spectra are shown in Fig. 2.8, normalized to the nominal (projected) electrode area. The high frequency intercept (>250 kHz) of ca. $3.5 \Omega\text{cm}^2$ found for most impedance spectra can be attributed to oxide ion conduction in the YSZ bulk. Slight differences of the intercept most probably originate from temperature variations between measurements, since samples were heated only from the bottom and the set temperature deviates from the true electrode temperature. Using an Arrhenius-type equation it is rather possible to determine the actual temperature directly at the microelectrode from the YSZ bulk resistance, provided the ionic conductivity of YSZ is known as a function of temperature⁶⁴. The larger frequency intercept value of the 19.3 nm $450^{0.4}$ thin film can be attributed to an increased electronic sheet resistance in LSC. The position of the arc or plateau in the medium frequency range from 250 kHz to 1 kHz varied strongly between the different samples, similar to earlier studies on mixed conducting electrodes⁶⁵. As it is barely affected by long-term annealing experiments at 550 $^{\circ}\text{C}$ and not responding to LSC surface treatments³¹, it is assumed to originate from the O^{2-} transfer across the LSC/YSZ interface, possibly including a contribution of O^{2-} transport through the LSC bulk.

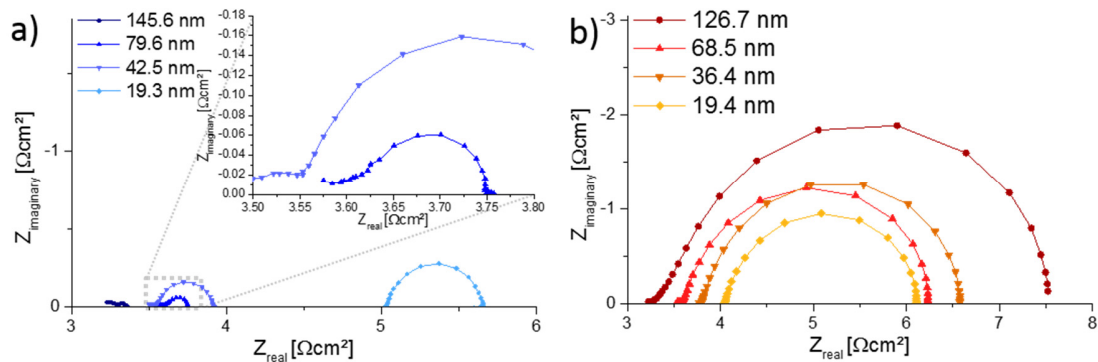


Fig. 2.8 Nyquist plots showing impedance spectra of the $450^{0.4}$ (a) and $450^{0.04}$ (b) films, measured at approx. 550 $^{\circ}\text{C}$ electrode temperature (600 $^{\circ}\text{C}$ set temperature) on microelectrodes of 200 μm diameter. The increased intercept for the 19.3 nm thick film results from an increased electronic sheet resistance.

At lower frequencies (1 kHz to 0.1 Hz) the shape of the impedance spectra became semicircle-like for all thin films and could be fitted to a parallel R-CPE-element (CPE = constant phase element with exponential fitting parameter $n > 0.95$). The resistive element R is attributed to the complex

oxygen surface exchange reaction ($R_{\text{surface exchange}}$) as it is sensitive to surface treatments and increases at low oxygen partial pressures, cf. also Refs.^{31, 66}. The capacitive element corresponds to the chemical capacitance of the film^{65, 67} and depends on the volume of the microelectrode: The resulting values are plotted in Fig. 2.9 and the typical thickness dependence of bulk chemical capacitances can clearly be seen. This chemical capacitor is determined by the properties of the bulk material, since it virtually stores the charge carriers in the perovskite lattice of the LSC. Therefore crystallinity, strain, etc. can be assumed to play an important role and those may differ between the two thin film deposition routes. This might explain the different absolute values for the same thickness of $450^{0.4}$ and $450^{0.04}$ films.

The size of the low-frequency semicircle strongly depends on the thickness of $450^{0.4}$ films. The increasing oxygen exchange resistance with decreasing $450^{0.4}$ film thickness is in accordance with the enlarged surface area of thicker films concluded from Sr amounts on the surface. However, all $450^{0.4}$ thin films exhibit similar peak frequencies due to a decreasing chemical capacitor for thinner films. The $450^{0.04}$ thin films, on the other hand, show only small variations of the surface resistance, particularly between 19.4 and 68.5 nm thicknesses but a change in the peak frequency. This is in accordance with little or no porosity concluded from ICP-OES measurements. A more detailed comparison of Sr amount and surface exchange resistance is given in the following.

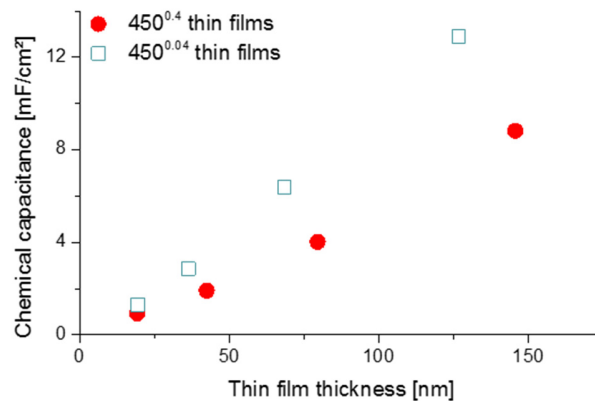


Fig. 2.9 Relation between the chemical capacitance and the film thickness of $450^{0.4}$ and $450^{0.04}$ thin films.

2.3.4 Comparison of surface composition and electrochemical properties

In Fig. 2.10 both the water soluble amount of Sr and $1/R_{\text{surface exchange}}$ are plotted vs. film thickness of (a) LSC $450^{0.4}$ and (b) $450^{0.04}$ thin films. For $450^{0.04}$ films neither clear trends for different thicknesses nor a clear relation between the (only moderate) variation of Sr amount and surface exchange resistance is found. This is in agreement with our assumption of dense $450^{0.04}$ films. However, both curves show a very clear trend for the $450^{0.4}$ thin films and both can be explained by porosity and thus a true surface area depending on the thickness: The larger the thickness (and the true surface area) the larger the inverse surface polarization resistance and the total amount of surface Sr. However, this does not necessarily mean that the entire $450^{0.4}$ films are porous.

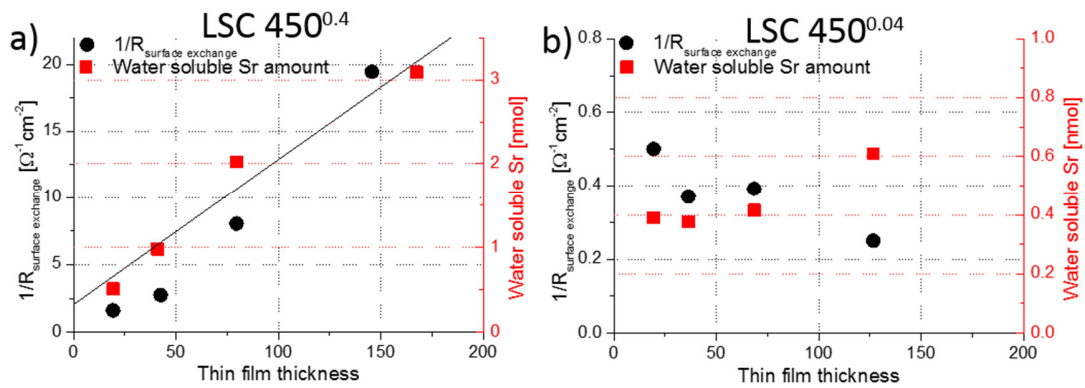


Fig. 2.10 Dependence of the surface exchange resistance (normalized to the nominal surface area) and the water soluble Sr amount on the film thickness of a) $450^{0.4}$ and b) $450^{0.04}$ thin films. For the $450^{0.4}$ thin films both data sets clearly indicate an enhanced surface area.

Rather, preliminary high-angle annular dark field (HAADF) measurements (Fig. 2.11) of the region close to the YSZ|LSC interface suggest density variations perpendicular to the interface⁶⁸. The intensity of the observed signal depends on specimen thickness, atomic number and density. In our case, all factors except from the density are assumed to be rather constant over the film thickness. The data therefore indicate a denser film (<23 nm) close to the YSZ interface. High resolution images of our films (Fig. 2.12) and also of similar LSCF films⁶⁰ revealed dense film regions close to the interface but open porosity for film parts on top of this dense layer.

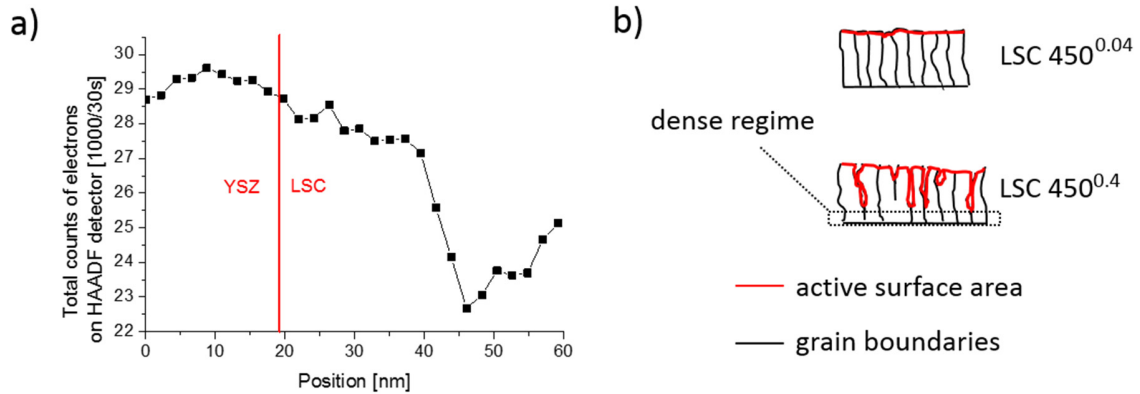


Fig. 2.11 (a) Total counts of electrons detected by HAADF STEM close to the YSZ/LSC interface (dotted line). A decrease, most probably related to pores, is observed after 20 nm of thin film growth. (b) Sketch of LSC thin film microstructure with columnar grains in both cases but pores only for 450^{0.4}.

Therefore, it is assumed that the first ca. 20 nm of 450^{0.4} films are still dense which is also in accordance with similar Sr amounts found for all dense 450^{0.04} films and the 19.3 nm thin 450^{0.4} film. A sketch of the microstructure of both film types, highlighting the active surface area (red), is given in Fig. 2.11b. For a rough estimate of the true surface area in porous 450^{0.4} films the Sr amount β and film thickness d is fitted to eq. (2.1)

$$\beta = \beta_0 + \alpha \cdot (d - 20 \text{ nm}) \quad (2.1)$$

with β_0 being the Sr amount on a dense layer (nominal electrode area) and α representing the total film thickness. The fit line is given in Fig. 2.10a and $\beta_0 = 0.671 \text{ nmol}$ and $\alpha = 0.01725 \text{ nmol/nm}$ are obtained. A 40 nm thick layer (20 nm dense, 20 nm porous) thus exhibits a surface area that is increased compared to the nominal sample area by a factor 1.5. For a 200 nm layer the area increase amounts to 5.6. Microstructural differences of the 450^{0.4} and 450^{0.04} films can be explained in terms of Thornton's well known structure zone model (SZM)⁶⁹ and the so-called "shadow effect"⁷⁰ during deposition. The 450^{0.4} thin film shows characteristics of zone 1 in the SZM, where only limited surface diffusion of deposited particles takes place⁶⁰. At higher oxygen partial pressures, more particle collisions occur during deposition, causing an increased angle distribution of decelerated incoming particles, which amplifies shadowing effects for the 450^{0.4} thin films and thus results in an increased porosity⁷¹. Pores can be expected to form at a certain roughness of the film but not from the very beginning of the film growth, see Fig. 2.12.

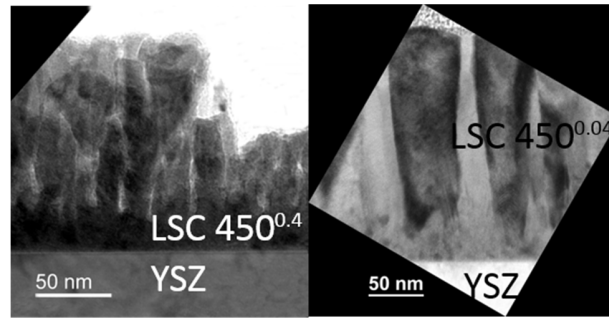


Fig. 2.12 TEM Bright field image of $450^{0.4}$ (l.h.s.) and $450^{0.04}$ (r.h.s.) film.

Based on these results the very low polarization resistance of low temperature deposited LSC films reported in Ref. ⁶³ ($0.1 \Omega\text{cm}^2$ for a 200 nm thin film at 600 °C set temperature) can be further interpreted. In contrast to the first impression, those films were most probably porous since the same deposition parameters were applied and the same electrochemical properties were observed as in this study. Such an assumption is also in accordance with systematic investigations of LSCF thin film growth on YSZ substrates at different substrate temperatures and gas pressures⁶⁰. Hence, differences in electrode resistance between 40 and 200 nm thin films in Ref. ⁶³ can rather be attributed to different electrode surface areas than to surface chemistry variations. In accordance with the estimated surface area increase of a 200 nm film, the polarization resistance related to the true surface area has to be corrected to ca. $0.5 \Omega\text{cm}^2$ at 600 °C set temperature (instead of $0.1 \Omega\text{cm}^2$).

It is finally worth mentioning that the polarization resistance of a LSC film measured at 600 °C is not altered when removing the surface Sr by ultrapure water. This, however, is simply caused by the fact that during heating and thermal equilibration (1 h at 600 °C), before the impedance measurements are started, water soluble Sr is again formed. Quantification by ICP-OES even showed that this newly formed amount of Sr is almost identical to that found for freshly prepared PLD layers. This suggests that already at rather low temperatures and short annealing times a surface reconstruction takes place which leads to the water soluble Sr surface phase.

2.4. Conclusions

By means of an improved on-line in-situ etching procedure with subsequent ICP-OES analysis using different eluents, a water soluble Sr-rich surface phase was found on top of $\text{La}_{0.6}\text{Sr}_{0.4}\text{CoO}_{3-\delta}$ (LSC) thin films, together with traces of Co. Assuming a dense SrO layer, the ca. 0.4 nmol Sr per 0.25 cm^2 found for low pressure (0.04 mbar) deposited films corresponds to 1.2 atomic layers covering the whole LSC surface. For thin films deposited at higher oxygen partial pressures (0.4 mbar) the water soluble Sr amount strongly increased with increasing film thickness. This was related to effective porosity and thus to an increased surface area of thicker films. The influence of this porosity on the surface exchange resistance could be quantified by combining impedance spectroscopy measurements and ICP-OES. It was possible to relate the results of the electrochemical measurements to the true surface area. The lowest surface exchange resistance of LSC seems to be approximately $0.5 \Omega \text{ cm}^2$ at $600 \text{ }^\circ\text{C}$. The dependence of the electrochemical performance of LSC thin films on the oxygen partial pressure during deposition was thus shown to be partly caused by microstructural differences, i.e. effective porosity.

3 Dynamic etching of soluble surface layers with on-line ICP-MS detection – a novel approach for determination of complex metal oxide surface cation stoichiometry

This chapter contains in large parts material published as a scientific paper in the Journal of Analytical Atomic Spectrometry⁷² with equal contribution of first and second author.

3.1 Introduction

Complex metal oxides (CMOs) are key materials in an increasing number of applications. Among the numerous crystal structures adopted by CMOs, those in the perovskite-type (ABO_3) family have received the greatest attention followed by spinel-type (AB_2O_4) and pyrochlore-type ($A_2B_2O_7$) structures. The growing interest over the past decades for these and other structures can be attributed to the functional diversity due to the wide range of properties that they can adopt⁷³. For example, in the fields of solid state electrochemistry and heterogeneous catalysis, complex metal oxides are attractive alternatives to expensive noble metal catalysts⁷⁴⁻⁷⁶. For both disciplines, excellent knowledge of the structure and composition of the investigated material at the reaction sites, i.e. in most applications the solid/gas phase boundary (surface), is required for understanding reaction mechanisms and tailoring properties. Nanoscaled systems (e.g. nanoparticles, thin films) may not only improve functionalities but are also indispensable to increase the surface/bulk ratio for a detailed analysis of the region of interest. Particularly, thin film model systems, mostly deposited by physical and chemical vapor deposition techniques, offer the possibilities for using a large variety of analytical methods to characterize the surface and near surface region as well as depth profiling the layers beneath.

Imaging methods, such as atomic force and scanning tunneling microscopy, are widely used to characterize the structure of the termination layer. For the analysis of the chemical composition, X-ray photoelectron spectroscopy (XPS) and Auger electron spectroscopy (AES) or ion bombardment techniques such as secondary ion mass spectrometry (SIMS), Rutherford backscattering (RBS) and low energy ion scattering (LEIS) are often applied⁷⁷. However, quantification of the exact surface composition by these techniques is non-trivial. Alternative methods for quantitative analysis of thin films are glow-discharge mass spectrometry (GDMS)^{78, 79}

or laser-ablation inductively coupled plasma mass spectrometry (LA-ICP-MS)^{80,81}. These and other well-established techniques also enable the analysis of depth profiles with sufficient sensitivity and depth resolution.

Application of these analytical tools has already shown that for complex metal oxides the structure and composition at and close to the surface frequently differ from the bulk. Elastic and electrostatic forces may drive segregation of dopants to the surface of CMOs^{42, 82}, reactions between gas phase and solid may lead to the formation of secondary phases^{83,84}, and exsolution of metallic particles on the surface of perovskites is found under reducing conditions^{85, 86}, to mention only a few examples. These changes are crucial for the (electro-)catalytic activity of the materials and their analysis requires methods that are specifically adapted to these complex phenomena. One example of a particularly challenging situation is given for the perovskite-type CMO $\text{La}_{0.6}\text{Sr}_{0.4}\text{CoO}_{3-\delta}$ (LSC). LSC is a promising cathode material for intermediate temperature solid oxide fuel cells due its high activity for the surface oxygen exchange⁸⁷⁻⁸⁹. However, degradation of the surface activity under various conditions is reported in the literature and several correlations to structural and/or compositional changes of the electrode surface have been reported^{90, 91}. Chemical investigations on thin LSC films using XPS, SIMS and inductively coupled plasma – optical emission spectrometry (ICP-OES) already revealed an accumulation of Sr at the electrode surface, which may be responsible for the deactivation of the oxygen reduction reaction^{31, 32, 53}. Furthermore, Cai et al.³² proposed a secondary Sr phase such as $\text{SrO}/\text{Sr}(\text{OH})_2$ at the surface based on different binding energies found for Sr 3d electrons using XPS. Nonetheless, by XPS it is non-trivial to qualitatively (and almost impossible to quantitatively) deconvolute Sr surface species from Sr in the LSC lattice. Accordingly, additional analytical methods with complementary information content, e.g. not only on ionic binding situations but also on phases, are therefore highly desirable.

Recently, Kubicek et al.³¹ presented a novel tool for surface chemistry analysis to overcome limitations of conventional depth profiling techniques. There, the surface of LSC thin films was etched with dilute HCl, and the eluate containing the dissolved cations was then analyzed on-line by ICP-OES. In contrast to classic batch-wise extraction procedures, this approach provides time resolved information on the availability and solubility of any dissolved species. Application of a slightly modified etching procedure allowed the verification of a Sr enriched region at the surface of porous LSC thin films, see chapter 2. However, limitations in sensitivity and reproducibility of analysis prevented the determination of surface cation stoichiometry as well as the measurement

of dense LSC thin films. Thus, further methodological development of the dynamic etching procedure is compulsory; in particular, to enable the investigations required for a better understanding of Sr segregation and the underlying physical and chemical phenomena.

In this chapter it is shown how this approach with dynamic etching can be continuously optimized. With the use of ICP-MS for element-selective on-line detection significant improvements in sensitivity were achieved. Adaption of the flow-injection system allowed consecutive etching of the sample with different solutions, thereby enabling a differentiation between water soluble and acid soluble LSC constituents. Moreover, improvements in accuracy and reproducibility of analysis could be obtained by changing material, design and volume of the etching cartridge. Achieved advancements allowed reliable measurement of the LSC thin film surface and near-surface cation composition, providing quantitative information about changes in the LSC stoichiometry. Applicability of the developed procedure for the analysis of dense LSC thin films was demonstrated by excellent agreement of the findings with results from low-energy ion scattering (LEIS) measurements.

3.2 Experimental

3.2.1 Reagents and standard solutions

High purity water was prepared using an Easypure water system (Thermo, USA, resistivity 18 M Ω ·cm) and used throughout the entire study. Nitric acid (65 %) and hydrochloric acid (37 %) was purchased from Merck (Darmstadt, Germany) with p.a. grade. Certified stock solutions (1000 mg·L⁻¹) of La, Sr and Co as well as Cu and Mn were procured from Merck (Darmstadt, Germany) and used for the preparation of calibration standards or as internal standards by dilution with 0.012 mol·L⁻¹ HCl.

3.2.2 Sample synthesis and preparation

The LSC target for PLD was obtained from stoichiometric mixtures of La₂O₃, SrCO₃, Co (99.995 % Trace Select, Sigma Aldrich, Steinheim, Germany) powders and prepared by Pechini synthesis⁶² as described in chapter 2.2.1. LSC thin films with a thickness of 200 nm were deposited onto (100) oriented 9.5 mol% yttria stabilized zirconia (YSZ) substrates (5x5x0.5 mm³) the deposition procedure and parameters are given in chapter 6.2.1.

3.2.3 Instrumentation

An iCAP 6500 series ICP-OES spectrometer (Thermo Scientific, USA) was used for method development. Sample introduction was performed using an APEX E high efficiency sample introduction system with a Meinhard concentric nebuliser and a cyclonic spray chamber (ESI Elemental Scientific, USA). Instrumental parameters and evaluated wavelengths used for ICP-OES measurement of thin surface layers are summarized in Table 1 and 2, respectively.

Table 1 Instrumental parameters used for ICP-OES analysis

parameter	value	parameter	value
radio frequency power	1250 W	Nebulizer flow	0.70 l·min ⁻¹
total sample flow rate	1.4 ml·min ⁻¹	Auxiliary flow	0.8 l·min ⁻¹
viewing height	12 mm	Coolant flow	12 l·min ⁻¹

Table 2 Evaluated wavelengths for ICP-OES analysis

element	λ_1 [nm]	λ_2 [nm]	λ_3 [nm]
La	333.749	379.478	419.655
Sr	216.596	346.446	421.552
Co	228.696	238.892	
Cu	224.700	324.754	
Mn	257.610		

ICP-MS analysis was conducted using quadrupole instrumentation (Thermo iCAP Qc, Thermo Scientific, Bremen, Germany). Sample introduction was accomplished employing a Peltier-cooled spray chamber equipped with a concentric quartz glass nebulizer. The instrumental parameters (Table 3) were optimized for maximum ¹¹⁵In signal and a ¹⁴⁰Ce¹⁶O/¹⁴⁰Ce ratio below 1.9 % on a daily basis using a standard tuning solution. The amount of doubly charged ions was measured by the ¹³⁷Ba⁺⁺/¹³⁷Ba⁺ ratio which was below 3 % for all experiments. To minimize the influence of potential instrument induced artifacts, the sample signals were normalized using ⁵⁵Mn as internal standard. Signal quantification was based on external calibration with aqueous standard solutions. Standards and blanks were measured at the beginning, during and at the end of an experimental session.

Table 3 Instrumental parameters used for ICP-MS analysis

parameter	value
total sample flow rate	0.8 mL·min ⁻¹
nebulizer gas flow	0.8 L·min ⁻¹
aux. gas flow	0.8 L·min ⁻¹
cool gas flow	14 L·min ⁻¹
RF power	1550 W
cones	Ni
measured isotopes	⁵⁵ Mn, ⁵⁹ Co, ⁶³ Cu, ⁶⁵ Cu, ⁸⁶ Sr, ⁸⁷ Sr, ¹³⁹ La
dwelt time per isotope	0.010 s
mass resolution	m/Δm = 300

For analysis of time resolved etching profiles a flow-injection (FI) system coupled to an ICP-OES or ICP-MS for element selective on-line detection was used. The applied FI-system consisted of a six port injection valve (VICI, Cheminert C22, USA) equipped with a sample cartridge for insertion of LSC samples. Arrangement of the applied FI-manifold was similar to the one recently described by Limbeck et al.⁹² for the dynamic extraction of water soluble trace metals in airborne particulate matter (Fig. 3.1). In the first part of the work, commercially available Chromafix® SPE columns (Macherey-Nagel, Germany, diameter 12 mm, length 14 mm) equipped with porous quartz frits were employed as sample cartridges. In the final procedure, homemade polytetrafluoroethylene (PTFE) micro-cartridges were used. In both cases the cartridges were connected to the FI-system using conventional luer-fittings, which allowed an easy and fast replacement of the etching compartment. The connections between the individual parts of the FI-system were made with PTFE tubes having an inner diameter of 0.7 mm.

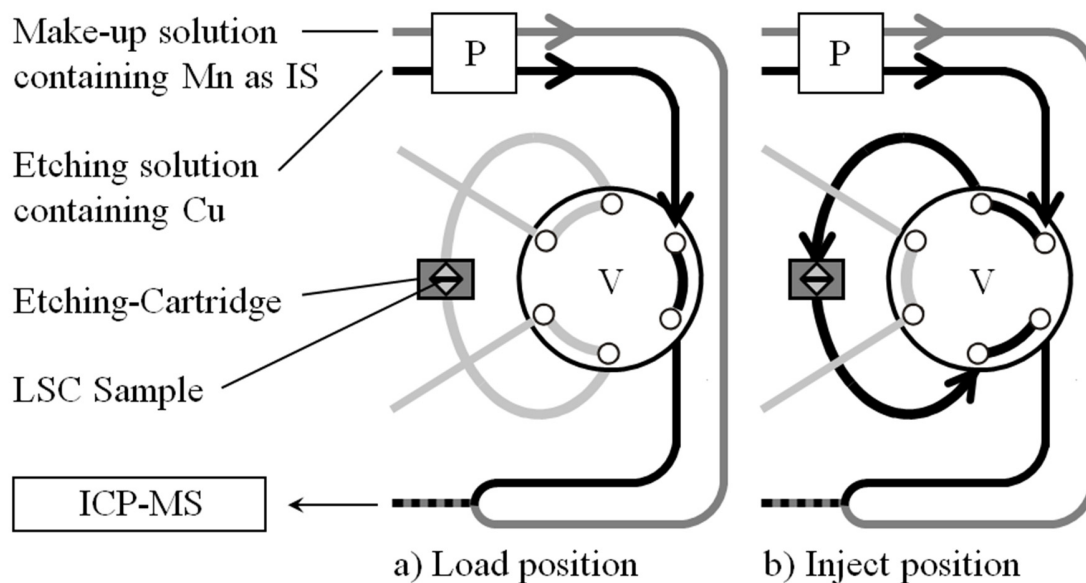


Fig. 3.1 FI Manifold for dynamic etching of LSC thin film samples: P peristaltic pump, V 6-port valve.

LEIS analysis of the LSC thin films were performed using a Qtac100 spectrometer (ION-TOF GmbH, Germany) fitted with a high brightness ion source to provide the primary beam (Hyperion, Oregon Physics, USA). Major advantage of LEIS is that the analyzer beam only probes the first atomic layer. The elemental composition of the surface was analyzed using a 6 keV Ne⁺ beam, which was directed normal to the surface and the kinetic energy distribution of the backscattered ions at 145° (collected over the entire azimuth) was analyzed to obtain the elemental composition of the first monoatomic layer. For depth profiling, a 1 keV Ar⁺ sputtering beam at a sputtering angle of 59 degrees was used. The sputtered area was 1.3 x 1.3 mm², with the central region of 1x1 mm² analyzed by the primary beam. The sputter rate for the depth calibration of the profiles was estimated by measuring the depth of a 300 x 300 μm² crater using laser interferometry (LEXT OLS4000, Olympus, Japan), assuming that the rate was uniform for the LSC thin film. For the quantification of the cation surface coverage, the plateau signals at the end of the depth profiles were used as the reference value for the bulk stoichiometry, as described in Ref. ⁹³.

To measure the impedance of LSC electrodes, a second LSC thin film (same deposition conditions) was deposited on the back side of the YSZ substrate. The impedance was then measured by a Novocontrol Alpha A High Performance Frequency Analyzer with an alternating voltage of 10 mV (rms) in a frequency range of 10⁶ to 10⁻² Hz. A detailed description of the setup can be found in chapter 6.2.3.

3.2.4 Dynamic etching procedure with on-line ICP-OES or ICP-MS detection

The procedure starts with switching the valve in the load position, in this alignment the etching solution (water or dilute HCl including $1.0 \text{ mg}\cdot\text{L}^{-1}$ Cu used as internal standard; flow rate $0.8 \text{ mL}\cdot\text{min}^{-1}$) is directed straight to the mixing device, enabling the removal or insertion of a sample containing etching cartridge. Prior to sample insertion the cartridge was carefully cleaned in an ultrasonic bath of $0.24 \text{ mol}\cdot\text{L}^{-1}$ HCl for 5 minutes to remove impurities remaining from the last measurement. After integration of a sample containing cartridge, the valve is switched back into the inject position and ICP-OES measurement is started. The etching solution introduced into the etching compartment initiates the etching process of the LSC film. The material dissolved by the etching agent is transported to the mixing device, where the eluate is combined with a make-up solution ($0.24 \text{ mol}\cdot\text{L}^{-1}$ HCl containing $0.5 \text{ mg}\cdot\text{L}^{-1}$ Mn as additional internal standard; flow rate $0.6 \text{ mL}\cdot\text{min}^{-1}$) and mixed thoroughly. The combined liquid flow is then directed into the sample introduction system of the ICP-OES instrument, where the transient elution profiles are measured.

In case of more sensitive ICP-MS detection time resolved intensities for the investigated isotopes were recorded with Qtegra software and exported as .csv files for further data treatment, in particular internal standard correction to overcome potential non-spectral interferences. For interpretation and further discussion the intensity data derived from the etching experiments were converted into absolute masses, which have been removed from the sample surface per time unit. For this purpose calibration functions were determined by analyzing matrix adjusted standard solutions with the same instrumental setup. Standards containing defined amounts of the investigated elements (blank level up to contents of $1000 \text{ }\mu\text{g}\cdot\text{L}^{-1}$) and $10 \text{ }\mu\text{g}\cdot\text{L}^{-1}$ Cu (used as internal standard) were prepared just before use by appropriate dilution of respective stock solutions with $0.012 \text{ mol}\cdot\text{L}^{-1}$ HCl. For analysis, the etching solution used as carrier was replaced with the standard solution to be investigated. Measurement of those standard solutions was performed in the load position solely. In analogy to the analysis of LSC samples, the liquid flow leaving the FI-manifold was mixed with make-up solution; and the combined flow introduced into the detection system. Prior to each ICP-MS analysis the system was purged with the examined standard solution for approximately 30 s, afterwards the signals of the selected isotopes were monitored for 120 s. The signal intensities (in counts per second) obtained for the investigated analytes were normalized using Mn as internal standard and correlated with the injected analyte masses, showing for all elements a linear behavior throughout the investigated mass range.

3.3 Results

3.3.1 Method development

Limitations in reproducibility and accuracy of analysis are considered the main drawbacks of the procedure reported in Ref. {Kubicek, 2011 #43}. Typical sources for these problems are analyte losses and/or memory effects, changes in the carrier flow rate and/or composition, alterations in the nebulizer efficiency as well as variations in the plasma load, causing undesirable fluctuations in the measured signal intensities. Since the investigated elements provide an enhanced solubility at lower sample pH, adsorption losses and/or memory effects are only of concern when pure water is applied as etching agent. In the latter case, material dissolved from the LSC surface could be lost during transport from the sample cartridge into the plasma due to adsorption of dissolved material on different parts of the analytical system (tubings, nebulizer, spray chamber, torch), impeding an accurate measurement of the eluate composition. To minimize the risk of analyte losses and/or memory effects, the sample flow coming from the etching cartridge is mixed on-line with 0.24 mol L^{-1} HCl as a make-up solution. The combined liquid flow is then introduced into the nebulizer unit of the detecting ICP-OES, where the transient etching profiles are measured.

To overcome the difficulties related with the mentioned non-spectral interferences, internal standards were applied. Whereas errors related to the sample introduction system could be compensated with any internal standard, the accurate correction of plasma related effects (e.g. energy transfer) requires the use of elements with excitation and ionization energies comparable to that of the target analytes. Thus, the elements Cu and Mn were selected as internal standards, having emission wavelengths close to that of the investigated LSC constituents. With the use of Mn (constituent of the make-up solution) changes in the sample introduction efficiency as well as plasma load could be monitored and corrected if necessary. Cu as constituent of the etching solution is used to control the liquid flow directed through the FI-manifold including the etching compartment. Moreover, the homogeneity of the solution leaving the mixing device could be controlled, a prerequisite for the accurate and reproducible measurement of etching profiles.

Beside improvement of the measurement step, a continuous optimization of the LSC thin film etching process is also required for reliable determination of distribution profiles. For this purpose an etching compartment is mandatory which delivers the eluent to the whole thin film surface uniformly, enabling homogenous sample dissolution by the eluent. Moreover, the etching compartment should provide fast wash out times to avoid mixing of sample eluates from

successive sample depths, and the absence of any memory effects due to adsorption or release of analytes. The last issue is of special importance since the acidic make-up solution introduced to overcome the problem of analyte losses protects only the sample introduction system located behind the mixing device. Thus in the etching cartridge adsorption losses are still possible, since this part is positioned before the mixing device and therefore operated with etching solution only. In the very first part of this work, where LSC thin films were simply sandwiched between two porous quartz frits and inserted into a SPE cartridge as reported by Kubicek et al.³¹, differentiation between water soluble and acid soluble contents of LSC thin films was hampered. Memory-effects caused by the pH dependent adsorption/desorption of dissolved LSC constituents on the porous frits were found to be the main reason. To overcome the problems associated with the use of commercial SPE cartridges and porous frits as sample holders, a new etching compartment was manufactured, which allows fixation of the LSC sample without the use of any additional substrate. The material chosen for this application was PTFE, giving the advantage of being resistant to strong acids and acetone, which also enables an effective cleaning of the cartridge prior to next use. Particular emphasis was laid on the geometry of the etching compartment (for details see Fig. 3.2), which should prevent movement of the sample during the etching process. The square sample (5x5 mm²) is placed in the funnel shaped etching compartment (corners in contact with the wall) and the liquid can pass the sample along the edges. Moreover, the volume of the compartment was minimized from 984 μL to 289 μL to decrease wash out time, hence lowering peak broadening. With this set-up reproducibility of analysis was improved significantly, since memory effects as well as unexpected fluctuations in the liquid flow could be completely avoided, enabling a reproducible determination of water and acid soluble LSC constituents.

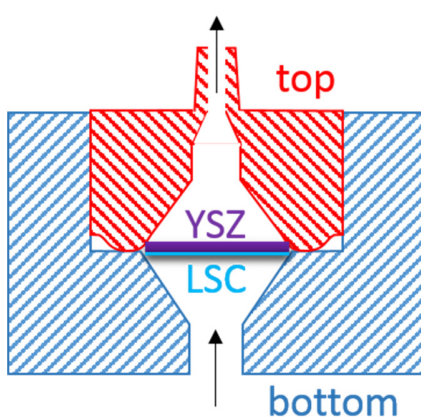


Fig. 3.2 PTFE etching compartment.

3.3.2 Element selective detection using ICP-MS

As demonstrated in Ref. {Kubicek, 2011 #43} the detection power of the ICP-OES employed as detection system is sufficient for the analysis of porous LSC films, but in case of dense LSC films with lower surface area limitations in sensitivity are expected. Compared to porous LSC films, the decreased surface area of dense LSC films results in a reduction of the etching rate, thus the amount of analyte introduced into the ICP per time unit is lower, impeding accurate analysis of the derived eluate. Insufficient detection power hampers also an appropriate characterization of the water soluble LSC phase, thus the stoichiometry determined for the water soluble phase could be erroneous. To overcome the problems related with ICP-OES detection, in all further experiments solely ICP-MS was used for element selective analysis. However, compared to ICP-OES the operating conditions of ICP-MS are different, thus, adaption of the dynamic etching procedure was necessary. In a first step the flow rates of etching and make-up solution were optimized, main purpose of this optimization step was to improve sample introduction efficiency without any deterioration of the etching profiles. Best results were achieved with a combined liquid flow of $1.0 \text{ mL}\cdot\text{min}^{-1}$. For lower flow rates, a further increase in the sensitivity of ICP-MS analysis was observed, but the wash-out behavior of the etching compartment decreased distinctly. The internal standards selected for ICP-OES measurements were also applicable for detection with ICP-MS, since the ionization potentials of the target analytes are comparable (Co) or even lower (La, Sr) to that of the internal standard elements (Cu, Mn). Furthermore, ICP-MS analysis of etching and make-up solution delivered basically no signals on the m/z values used for detection of target analytes, indicating the absence of notable contaminations as well as spectral interferences. Concentrations of the applied internal standards were reduced to $10 \mu\text{g}\cdot\text{L}^{-1}$ (Cu) and $5 \mu\text{g}\cdot\text{L}^{-1}$ (Mn) only.

With the optimized flow rate and the instrumental parameters described in Table 2 a significant increase in sensitivity could be achieved. For signal quantification matrix adjusted standard solutions and integration intervals of 1 s were applied, a more detailed description is presented in the chapter 3.2.3. Compared to ICP-OES, the detection limits ranging from 7 (La at 379.478 nm) to 35 (Co at 228.696 nm) $\mu\text{g}\cdot\text{L}^{-1}$ could be reduced by 2 magnitudes of order using the ICP-MS ($0.03 \mu\text{g}\cdot\text{L}^{-1}$ for ^{139}La , $0.04 \mu\text{g}\cdot\text{L}^{-1}$ for ^{59}Co and $0.15 \mu\text{g}\cdot\text{L}^{-1}$ for ^{86}Sr). With quadrupole ICP-MS instrumentation lower detection limits are usually possible, however, the operating conditions required in this special application (sample uptake rate of $1.0 \text{ mL}\cdot\text{min}^{-1}$, and the measurement of transient signals with integration intervals of 1 s only) resulted in decreased sensitivity. The quality

of the applied chemicals could also contribute to the achieved detection limits, since prevailing impurities might increase the background signals for the target analytes. Thus, with the use of ultrapure grade chemicals further improvements in sensitivity are expected. Nevertheless, the detection limits were low enough to quantify the transient data obtained during each step of the etching process. Fig. 3.3 shows element intensity/time profiles of an LSC thin film first etched with water and then with 0.012 mol·L⁻¹ HCl measured by ICP-MS. The ⁸⁶Sr baseline signals were found to be in the order of 200 cps only, whereas the signal intensity increases to 200.000 cps during water etching before it slowly diminishes to around 2.000 cps and rises again to around 150.000 cps after switching the eluent to diluted HCl. Using the determined calibration functions derived ICP-MS signals were converted into concentrations, which were found to range between some μg·l⁻¹ and several hundred μg·L⁻¹.

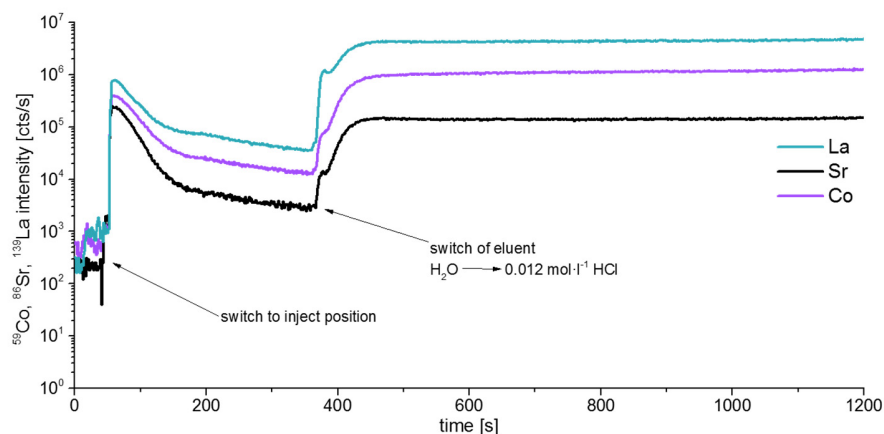


Fig. 3.3 Time resolved ⁵⁹Co, ⁸⁶Sr, ¹³⁹La intensities of LSC thin films analyzed using PTFE compartment and ICP-MS. The eluent was switched from ultrapure H₂O to 0.012 mol·l⁻¹ after ~390 s.

3.3.3 Analytical performance

As already mentioned in the introduction, changes of the surface cation stoichiometry are considered the main reason for degradation of the electrochemical performance of LSC. Thus, special emphasis was dedicated to the reliable analysis of surface and near-surface regions of LSC thin films. For this purpose, a set of LSC thin films was produced using identical PLD conditions. Analysis of water soluble parts of the films was performed with the use of water as etching solution; samples were subsequently treated with 0.012 mol·L⁻¹ HCl to continuously dissolve the remaining acid soluble LSC constituents. Progress of the etching process was monitored by ICP-MS measurement of the derived sample eluates. Obtained etching profiles do not reveal any

obvious differences, indicating that the measurement of LSC thin films is highly reproducible. This is also confirmed by the small variations in the peak areas obtained for the water soluble LSC parts, showing relative standard deviations (n=3) of 1.0 % for Sr, 1.6 % for La and 3.0 % for Co. Similar findings can be found in literature for other FI-ICP-MS procedures reported for a variety of applications including on-line sample extraction⁹⁴, analyte enrichment⁹⁵ and matrix or analyte separation⁹⁶.

Due to the higher sensitivity of the ICP-MS employed as detection system, experiments become feasible which were not possible with the setup described in Ref. ²¹. One scientific task which could thus be addressed is the analysis of dense LSC thin films using water as etching solvent. This results in very low etching rates and thus sample eluates with concentrations not measurable with ICP-OES. To this end, a set of identical dense LSC thin film samples was investigated by means of both detection techniques and treated first with water and subsequently with etching solutions of increased acidity. For further discussion, the intensity/time data received by the detector was converted into molar ratios versus time profiles using the procedure developed for signal quantification. As expected, the ICP-OES signals were close to the respective detection limits, and do not allow a reliable differentiation between parts of LSC with different solubility. Detection by ICP-MS, on the other hand, leads to very precise and reliable profiles for all elements (Fig. 3.4a). From the ICP-MS results, it is evident that significant quantities of Sr but also Co and La were dissolved by the treatment with water. Moreover, the amount of water soluble species at the thin film surface decreased significantly with ongoing reaction time, see also Fig. 3.3. Changing the eluent to 0.012 mol·L⁻¹ HCl resulted in substantially increased signals for Sr, Co and La, until a horizontal plateau of signals (Fig. 3.3) as well as molar ratios (Fig. 3.4a) is observed, indicating a constant etching rate for all thin film constituents.

From the findings presented in Fig. 3.4a, it can be concluded that the near surface region of the LSC thin film contains mainly Sr, while Co and La were only detected in minor amounts. While with ongoing etching time and thus sample depth the absolute ICP-MS signals decreased drastically, the relative contribution of Co and La increased continuously, leading to a rather constant composition of the water soluble part of the LSC sample after approximately 200 s. Compared to the known LSC thin film stoichiometry (dotted line in Fig. 3.4a) this water soluble fraction (between 200 s - 400 s) still exhibits significant differences – in particular a depletion of La and an enhanced contribution of Sr. However, only a very small amount of cations (< 0.3 nmol) is dissolved during this time interval, which is also reflected by the tailing of the water-soluble peak

in Fig. 3.3. With the use of $0.012 \text{ mol}\cdot\text{L}^{-1}$ HCl as etching solution the detected molar ratio changed again, revealing practically the known composition of the LSC thin films.

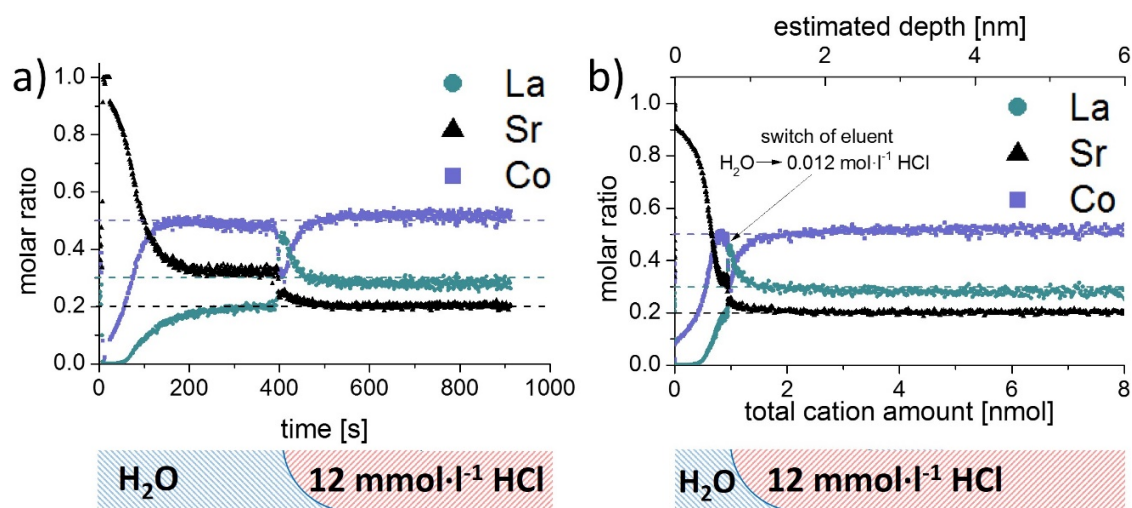


Fig. 3.4 (a) shows the molar ratio of dense LSC thin films vs. measurement time during the dynamical etching procedure and analysis by ICP-MS, including description of applied eluent sequence below the profiles. In (b) the molar ratio is plotted vs. the total cation amount (similar to depth profiles).

Further information becomes available when relating the molar ratios to the total amount of eluted cations instead of time. It can be clearly deduced from the ICP-MS results (Fig. 3.4b), that the water soluble fraction represents only a minor part of the dissolved LSC thin film sample and is largely Sr enriched. Assuming that the LSC sample is dissolved homogeneously (layer by layer) the obtained concentration versus time plots could even be converted into depth profiles with knowledge of the respective etching rates. Application of this methodology would result in depth resolutions reaching the sub-nm range (see top abscissa in Fig. 3.4b) and thus be very competitive to traditional approaches such as GDMS⁹⁷, SIMS⁹⁸ or LA-ICP-MS analysis⁹⁹. However, since preferential dissolution of the LSC thin film material on grain boundaries or defect rich regions will most probably occur, the depth scale should only be considered as a rough estimation.

For demonstration of accuracy and reproducibility four PLD deposition batches of LSC thin films, consisting of four individual samples each (i.e. 16 samples), were either analyzed using the procedure developed or in a conventional batch wise approach by dissolving the entire film. For both procedures, $0.012 \text{ mol}\cdot\text{l}^{-1}$ HCl was chosen as etching solution. The analysis time for the dynamic measurements was extended accordingly to allow monitoring of the whole dissolution process, signal quantification was performed as mentioned before. For batch wise experiments

the samples were treated with the etching solution in closed reaction tubes. After complete dissolution of the LSC thin films, the substrates were removed from the tubes and sample acidity of the derived solutions has been adjusted to $0.12 \text{ mol} \cdot \text{l}^{-1}$ HCl prior to ICP-MS analysis. The results derived for the total cation amounts of the LSC samples were in excellent agreement, revealing only negligible differences between batch experiments and dynamic ICP-MS measurements. Furthermore, for quality assurance the samples derived from batch experiments were also measured using ICP-OES, delivering results practically identical to the ICP-MS findings. Thus, the applicability of the proposed dynamic etching procedure as well as the accuracy of the applied quantification approach is confirmed, in particular when considering that the production of LSC thin films can also generate minor variations in the composition of the investigated sample sets.

3.3.4 Analysis of surface treated thin films - comparison with LEIS

The developed procedure was applied to compare the surface composition of different dense LSC thin films. In order to understand which parts of the films are water soluble and to compare these results to LEIS measurements, the following experiment was performed: Three of six as-deposited LSC thin films were stirred ex-situ for 10 minutes in ultrapure H_2O and blown dry with high purity N_2 . All six thin films were then analyzed by the dynamic ICP-MS etching procedure. Representative time-resolved concentration profiles for all elements are shown in Fig. 3.5a and 3.5b. The only significant difference between the as-deposited and H_2O pretreated thin films is seen in the part of the profile resulting from H_2O etching.

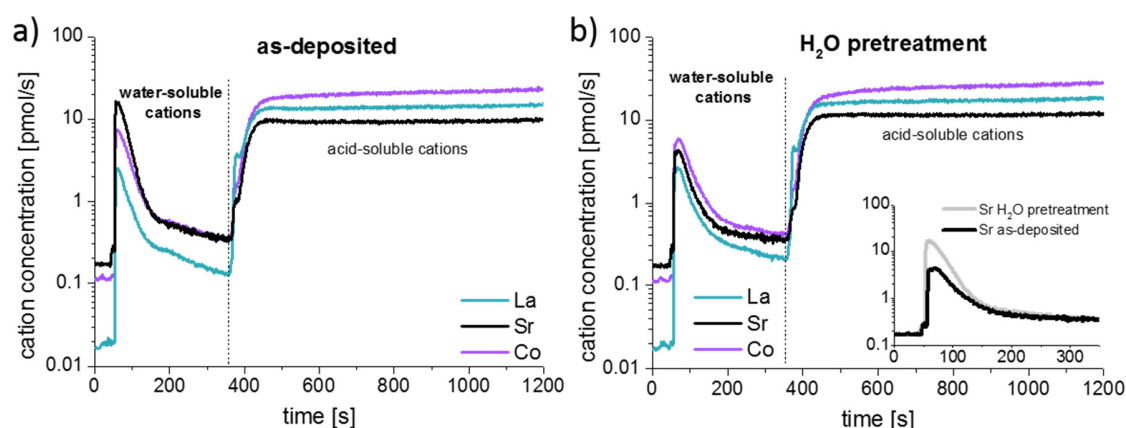


Fig. 3.5 Representative time-resolved ICP-MS concentration profiles for (a) as-deposited LSC thin films and (b) after ex-situ H_2O treatment. Inset in (b) directly compares the Sr concentration in the water-soluble part.

The exact amount of cations etched by water were determined by integration (Fig. 3.5 beginning of the measurement up to the dashed line). The amount of water soluble Sr is decreased by 0.39 ± 0.02 nmol after the H₂O pretreatment, while only minor changes are observed in the La and Co concentration. From the lattice parameter of SrO, it can be calculated that 0.33 nmol Sr would be needed to form one atomic layer of highly water-soluble SrO (100 direction) covering the entire 5x5 mm² surface of the thin film. Accordingly, the additional 0.39 nmol Sr removed from LSC layers without H₂O pretreatment corresponds to approximately 1.2 atomic layers of SrO. The remaining cations dissolved with as well as without H₂O pretreatment would then sum up to about one to two slightly Sr enriched elementary cells of LSC, though inhomogeneous etching might play a role here. This result strongly suggests that the main difference between the surface composition of an as-deposited and a H₂O treated layer is the absence of a strongly Sr-rich layer in the latter case. The fact that also after H₂O pretreatment, in the beginning of the measurement, an increased amount of the LSC lattice is dissolved in water may be explained with the influence of trace gases, e.g. CO₂, SO₂ adsorbed at the sample surface or PTFE compartment.

To confirm the findings from ICP-MS measurements, further LSC thin films were prepared and analyzed by LEIS. Depth profiles over the first 5 nm of the thin films for the Sr/(Sr+La) and Co/(Sr+La) ratio are shown in Fig. 3.6a and 3.6b, respectively. The very first measurement points of the LEIS profiles represent the cation composition of the surface layer. For the as-deposited thin film it can be seen that most of the cation sites in the surface layer are occupied by Sr (81 %), Co and La are thus strongly depleted. An enrichment in Sr and depletion of La is also determined for the first 2 – 3 nm of the LSC thin film, even though the sub-surface shows a Co / (Sr + La) ratio that is already very close to the bulk stoichiometry. After the ex-situ H₂O treatment, the surface layer shows a decreased Sr / (Sr + La) ratio compared to the as-deposited sample, although Co is still depleted. A slight Sr enrichment is again observed beneath the surface.

Both methods, LEIS and ICP-MS, suggest that the LSC lattice has a very Sr rich termination layer. A Sr enriched near-surface region (1-3 nm information depth) was also confirmed by Cai et al. {Cai, 2012 #1081} from XPS measurements on similar LSC thin films. In their work, they also proposed that the LSC lattice is SrO / Sr(OH)₂ terminated, since evidence of SrCO₃ species was not obtained. Also the La enriched and Co depleted surface composition measured by our LEIS study after the ex-situ H₂O treatment finds its counter-part in the ICP-MS experiment: A sharp peak of La together with a depletion of Co is observed after switching from H₂O to diluted hydrochloric acid (Fig. 3.4a and b).

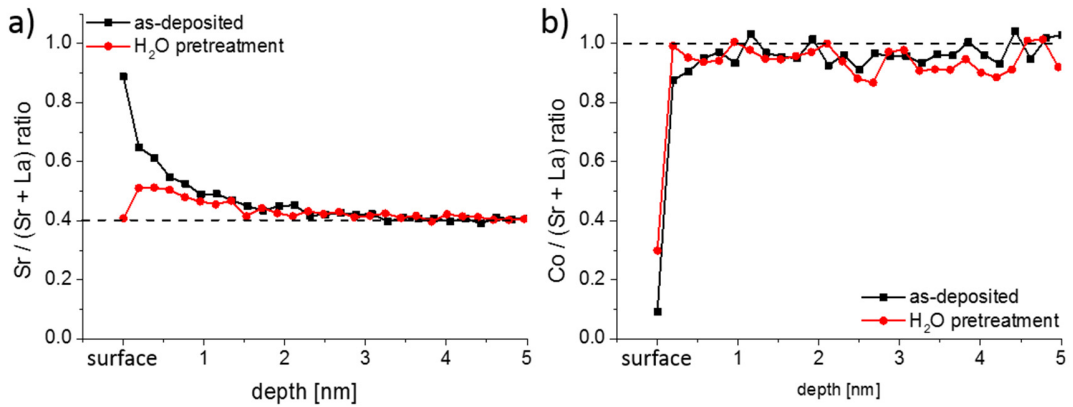


Fig. 3.6 (a) $Sr / (Sr + La)$ and (b) $Co / (Sr + La)$ depth profiles measured by LEIS for as-deposited and ex-situ H_2O treated LSC thin films.

Quantitatively, LEIS results indicate a Sr coverage of 81 % of the surface. ICP-MS, on the other hand, revealed 1.2 atomic layers of SrO. This difference may arise since LEIS probes a 2D projection of the surface and ICP-MS the true surface area (total solid-gas phase boundary) of the sample. The latter is larger due to cracks in the films. In chapter 2 it was shown that this enhanced surface area from open porosity can be even quantified on microporous LSC thin films by this method.

Finally, EIS measurements were conducted on as-deposited and H₂O pretreated samples at 400 °C in 1 mbar pO₂ in order to compare the electrochemical properties (O₂ exchange kinetics); representative spectra are shown in Fig. 3.7. A detailed analysis of such impedance data is given in chapter 4.3.3 and showed that the low frequency arc can be correlated to the oxygen exchange reaction at the LSC surface. It can be seen that the surface treatment does not affect the electrolyte resistance but lowers the electrode resistance by about 50 %. This confirms the detrimental effect of the water-soluble SrO top layer on the oxygen exchange activity.

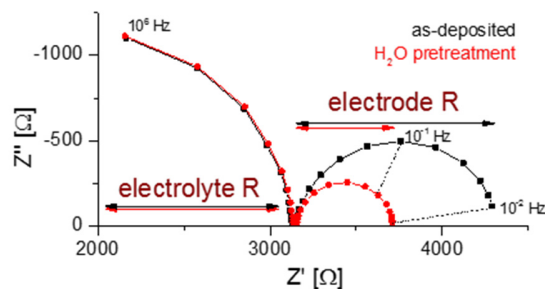


Fig. 3.7 Nyquist plots of the impedance measurements performed at 400 °C in 1 mbar pO₂ for as-deposited and H₂O treated LSC

3.4 Conclusions

The analytical procedure presented in this chapter allows determining the chemical composition of surface and near surface regions of complex metal oxide thin films. Differentiation between water and acid soluble sample constituents was accomplished by preliminary treatment of the sample surface with water, followed by etching with diluted HCl, and element specific on-line analysis of the derived solutions. The required sensitivity was achieved with the use of ICP-MS as detection technique; non-spectral interferences during on-line ICP-MS measurement were corrected by means of internal standards. Stepwise optimization of the etching cartridge resulted in an improved washout behavior and the complete elimination of memory effects. Compared to conventional approaches used for surface analysis of solids such as XRF, SIMS, GDOES or GDMS, laser ablation combined with ICP-OES or ICP-MS, the necessity of appropriate matrix matched standards could be circumvented, since simple aqueous standards could be used for signal quantification. A further benefit of the proposed procedure is the ability to distinguish phases with different solubility, whereas common techniques allow only the measurement of total element contents.

The developed procedure was applied for the analysis of LSC thin films. LEIS and on-line ICP-MS measurements revealed a water-soluble Sr-rich termination layer on freshly deposited dense LSC thin films. Qualitatively and quantitatively, a very good agreement between the results obtained by these two techniques was found. The oxygen exchange rates were measured by impedance spectroscopy and an improvement was determined after removing the water-soluble Sr-rich phase from the surface, suggesting that the LSC surface is blocked or inactivated by the formation of this water soluble Sr-rich phase.

4 Surface chemistry of $\text{La}_{0.6}\text{Sr}_{0.4}\text{CoO}_{3-\delta}$ thin films and its impact on the oxygen surface exchange resistance

This chapter contains in large parts material published as a scientific paper in the Journal of Materials Chemistry A¹⁰⁰.

4.1 Introduction

Primarily, surface sensitive analytical techniques such as X-ray photoelectron spectroscopy (XPS)^{32, 33, 37, 45, 46, 101}, secondary ion mass spectrometry (SIMS)^{31, 47} and low energy ion scattering (LEIS)⁴⁸ have been employed to investigate the surface region of perovskite-type oxides and its influence on the oxygen exchange kinetics. Many of these studies connected degradation of the electrochemical kinetics to a Sr enrichment in this surface region in various perovskite-type materials such as $(\text{La,Sr})\text{MnO}_{3-\delta}$ ^{29,30}, $(\text{La,Sr})(\text{Co,Fe})\text{O}_{3-\delta}$ ³¹⁻³³, $\text{Sr}(\text{Ti,Fe})\text{O}_{3-\delta}$ ^{34,35} and $(\text{Ba,Sr})(\text{Co,Fe})\text{O}_{3-\delta}$ ³⁶ upon elevated temperatures or polarization. A variety of poisons, such as SO_2 , CO_2 ³⁷⁻³⁹ and Si or Cr sources^{40, 41} in the vicinity of a perovskite sample in wet atmosphere, were already shown to enhance the Sr segregation and degradation. On the one hand, thin film electrodes may exhibit excellent electrochemical performance with low polarization resistance^{31, 50, 63, 102, 103}. On the other hand, even on a short time scale (hours, days) stable measurements of the surface exchange rate of thin film electrodes are difficult to achieve, which not only impedes the commercialization of such thin film electrodes in devices but also hinders research to deconvolute the complex mechanism of surface exchange in perovskite-type oxide electrodes.

LEIS offers the possibility to quantitatively measure the cation occupation of the termination layer. Different LEIS studies on perovskite-type oxides with alkaline earth substituted A-sites confirmed a strong preference for termination by A cations with enrichment of Sr and Ba in the termination layers upon annealing at temperatures between 400 and 1000 °C^{93, 104, 105}. A further very surface sensitive tool is slow wet chemical etching and time resolved analysis of the eluate by inductively coupled plasma (ICP) spectrometry^{31, 50}, see also chapter 2 and 3.

This chapter describes composition changes of the surface and bulk (first 20 nm) of $\text{La}_{0.6}\text{Sr}_{0.4}\text{CoO}_{3-\delta}$ thin films analyzed by LEIS and time resolved inductively coupled plasma-mass spectrometry (ICP-MS), see also chapter 3. Effects of annealing and chemical etching on surface properties were

determined. The cation occupation of the termination layer as well as the semi-quantitative composition of the sub surface layers were obtained by LEIS, while time resolved ICP-MS was able to measure the quantitative cation composition of the first 3-4 atomic layers of the LSC thin film. The combination of both methods allows to separate measurement artifacts and simplifies the interpretation. This gives the possibility to directly correlate cation changes with the kinetics of the oxygen surface exchange reaction measured by electrochemical impedance spectroscopy (EIS).

4.2 Experimental

4.2.1 Thin film preparation

Targets for deposition of LSC thin films by pulsed laser deposition (PLD) were synthesized from powders prepared by Pechini synthesis⁶². La_2O_3 , SrCO_3 and Co powders (all Sigma Aldrich, 99.995 %) were individually dissolved in nitric acid, mixed in appropriate ratios and citric acid (TraceSELECT®, 99.9998 %) was added for chelation. A calcination step was performed at 1000 °C, followed by isostatically pressing (~150 MPa) of the powder to a pellet and a sintering procedure at 1200 °C for 12 hours in air, thus yielding a LSC target for PLD. The target composition was determined from a deposited film, which was completely dissolved in 0.12 mol·l⁻¹ hydrochloric acid and analyzed by conventional ICP-OES. The target composition was determined to be $\text{La}_{0.62\pm 0.02}\text{Sr}_{0.41\pm 0.02}\text{Co}_{0.97\pm 0.04}\text{O}_{3-\delta}$.

The LSC thin films were deposited onto (100) oriented yttria stabilized zirconia (YSZ, 9.5 mol% Y_2O_3 , Crystec GmbH, Germany) single crystals with a thickness of 0.5 mm and a size of 5x5 mm². Epitaxy-ready polished substrates were used to prepare symmetrical samples with LSC thin films on both sides of the YSZ for impedance measurements, while LSC was simply deposited on one side of the substrate for the analytical measurements. Ablation of the target material was carried out by a KrF ($\lambda = 248$ nm) excimer laser (Lambda COMPexPro 201F) operated at a pulse repetition rate of 5 Hz, a pulse duration of 50 ns and a laser fluence of approximately 1.5 J·cm⁻² at the target. The atmosphere was set to 4·10⁻² mbar oxygen partial pressure and the substrate was heated to a surface temperature of 550 °C. By applying 6,750 laser pulses to the LSC target, an LSC film of approx. 200 nm thickness was grown on the substrate (substrate to target distance = 6 cm). After deposition the sample was cooled in the deposition atmosphere at a cooling rate of 12 °C·min⁻¹. The substrate was flipped and the PLD procedure was repeated on the back side for the

symmetrical samples. It is noteworthy that the sample surface was never exposed to “cleaning” treatments after deposition in order to avoid any reactions and contamination from solvents.

4.2.2 Microstructural characterization

The PLD target material was analyzed in Bragg Brentano geometry with a X'Pert Powder (PANalytical) diffractometer. A thin film diffraction pattern was obtained using a D8-Discover instrument (Bruker AXS) in parallel beam geometry equipped with a general area detector diffraction system (GADDS) at an accelerating voltage of 45 kV and measuring time of 200 seconds per frame and a step size of $0.2^\circ 2\theta$ per frame. Secondary electron microscopy was performed on a FEI Quanta 200 field emission gun scanning electron microscope equipped with an Everhart-Thornley detector. The microstructure of thin film cross-sections was analyzed by transmission electron microscopy (TEM) using an FEI Tecnai F20 equipped with a field emission gun at acceleration voltages of 200 kV.

4.2.3 Electrical characterization and annealing

All annealing and impedance experiments were performed in a cleaned quartz tube which was evacuated and refilled several times with the desired high purity N_2 (ALPHAGAZ™ 1 >99.999 mol% nitrogen)/ O_2 (ALPHAGAZ™ 1 >99.998 mol% oxygen) mixture (210 or 1 mbar O_2) before the sample was heated. LSC thin films deposited on one side of the electrolyte for surface analytical characterizations were simply placed inside the quartz tube while symmetrical samples (LSC – YSZ – LSC) were sandwiched between two platinum foils for impedance measurements. The electronic connection in the sample holder consisted of Pt wires and a non-encapsulated type S thermoelement was used for temperature measurement. No materials other than Pt, quartz and the sample itself were heated during impedance measurement and annealing. All these precautions were taken in order to obtain electrochemical and compositional measurements that do not suffer from any cathode poisoning. It took approximately 1 hour to heat the sample to the desired temperature (thermal equilibration), then the impedance measurements were started. The impedance was measured by a Novocontrol Alpha A High Performance Frequency Analyzer in the frequency range from 10^6 to 10^{-2} Hz with a resolution of five points per decade and an alternating voltage of 10 mV (rms) applied between the two LSC thin films.

4.2.4 Low-energy ion scattering (LEIS)

Surface and near-surface analysis of the samples was performed by LEIS using a Qtac¹⁰⁰ spectrometer (ION-TOF GmbH, Germany) fitted with a high brightness ion source to provide the primary beam (Hyperion, Oregon Physics, USA). Several noble gas ion beams can be used for the analysis depending on the spectral range to be analysed. Typically, a 3 keV He⁺ beam is used to check the presence of organic contamination on the surface, indicated by a characteristic surface peak at ~846 eV. The cation composition of the surface is analysed using a 6 keV Ne⁺ beam, which provides a better mass resolution for heavy elements. The primary ion beam is directed normal to the surface and the kinetic energy distribution of the backscattered ions at 145° (collected over the entire azimuth) is analysed to obtain the elemental composition of the first monoatomic layer. Depth profiling analysis was performed in a dual beam mode using a 1 keV Ar⁺ sputtering beam at a sputtering angle of 59 degrees. The sputtered area was 1.3 x 1.3 mm² whereas a central region of 1x1 mm² was analysed by the primary beam. The sputter rate for the depth calibration of the profiles was estimated by measuring the depth of a 300x300 μm² crater using laser interferometry, assuming that the rate was uniform for the LSC thin film (the sputtered crater used for this calibration was terminated before reaching the YSZ substrate). For the quantification of the cation surface coverage, the plateau signals at the end of the depth profiles were used as the reference value for the bulk stoichiometry, as described in ref. ⁹³.

Due to the extreme surface sensitivity of the technique, any adventitious contamination from the exposure to air is detrimental for the analysis. The LEIS instrument is fitted with a cleaning stage such that the samples could be cleaned by oxidation of the surface at room temperature prior to the analysis to remove the adsorbates (e.g. H₂) or organic contaminants on the surface. In this process, the surface is cleaned by (chemical) oxidation using a reactive atomic oxygen flux once the sample is introduced at the instrument's load-lock chamber (base pressure around 10⁻⁸ mbar), without further exposure to the atmosphere. The neutral atomic oxygen with almost no kinetic energy is extracted from an RF plasma source (higher energy ionized species from the plasma are not extracted). This beam of oxygen atoms reacts with the hydrocarbons on the surface to form volatile H₂O, CO and CO₂ that are pumped away by the vacuum system. This procedure was proven to be very effective to clean oxide surfaces, like YSZ¹⁰⁶. The oxidation cleaning was performed in several 15 minutes cycles until the surface was free of organic contamination. The effectiveness of the cleaning process was checked by the analysis of the surface with 3 keV He⁺ ions until no carbon peak was detected (peak position at 846 eV) and similar intensities of the rest of the

constituent cations for two consecutive spectra were obtained after a cleaning step (e.g. the La surface peak remained the same intensity before and after the cleaning cycle).

4.2.5 On-line ICP-MS

The near surface composition of the LSC films as well as their bulk composition was determined by time-resolved analysis of the eluate resulting from chemical etching. The samples were installed into a custom-made polytetrafluoroethylene etching compartment with a volume of 289 μl . The LSC layers were then slowly dissolved in a continuous flow of ultrapure water (produced by BarnsteadTM EasypureTM II (18.2 $\text{M}\Omega\cdot\text{cm}^{-1}$)) which was switched to 0.012 $\text{mol}\cdot\text{l}^{-1}$ hydrochloric acid (EMSURE[®] for analysis) after 360 seconds during the time resolved measurement. A second liquid flow of an internal standard, 10 ppb Mn (prepared from Mn-Standard, Titrisol[®]) spiked 0.24 $\text{mol}\cdot\text{l}^{-1}$ hydrochloric acid was merged with the eluate (eluent + dissolved cations) of the sample for correction of instrumental drifts. An external peristaltic pump (Spetec GmbH, Perimax 12) directed the eluent flow through the etching compartment and the total liquid flow towards the iCAPTM Q (ThermoFisher Scientific, Bremen, Germany) ICP-MS spectrometer introduction system, consisting of a Peltier cooled spray chamber (PFA nebulizer and cyclone) and a quartz torch. The liquid flow was set to $\sim 1 \text{ ml}\cdot\text{min}^{-1}$ and the nebulizer gas flow to 1 $\text{l}\cdot\text{Ar}\cdot\text{min}^{-1}$. The RF-power was set to 1550 W, and a 0.8 $\text{l}\cdot\text{Ar}\cdot\text{min}^{-1}$ auxiliary and a 14 $\text{l}\cdot\text{Ar}\cdot\text{min}^{-1}$ cooling gas flow were applied. Before starting the first measurements the setup was optimized with a tuning solution to yield maximum intensity for ^{110}In and a low CeO^+/Ce^+ ratio (<1.9 %). For the measurements of LSC thin films, each isotope (^{55}Mn , ^{59}Co , ^{86}Sr and ^{139}La) was measured using a dwell time of 10 μs . A mixed solution of La (ICP-Multi-Element Standard, Aristar[®]), Co and Sr (both Plasma Emission Standard, Prolabor[®]) was used for standard calibration.

4.3 Results

4.3.1 Structural characterization

The surface morphology of a 210 nm thin LSC film on top of YSZ was investigated by FESEM, see Fig. 4.1. Closely packed grains with a size of 40 - 70 nm are found together with cracks on the surface of the thin film. Crack formation cannot be avoided and is caused by the difference of thermal expansion coefficients between thin film ($\text{LSC64}^{107} = 20.5 \cdot 10^{-6} \text{ K}^{-1}$) and substrate ($\text{YSZ}^{108} = 10.8 \cdot 10^{-6} \text{ K}^{-1}$). It takes place during cooling to room temperature after thin film deposition. TEM cross-sections, Fig. 4.1, confirm the dense packing of columnar grains without any voids in between the grains as expected for the PLD growth conditions^{50,60} used here.

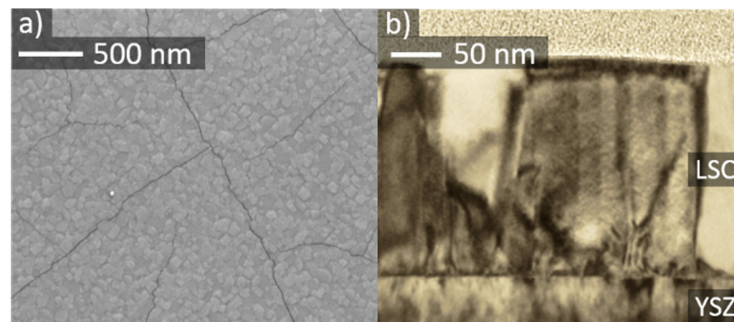


Fig. 4.1 SEM image of a LSC thin film surface (a) and TEM cross-section of a ~210 nm thin LSC film (b).

In Fig. 4.2, patterns over the measured 2θ range are shown for the LSC64 target and the thin film diffraction. All visible peaks of the polycrystalline target diffraction pattern could be assigned to the LSC64 perovskite phase and no sign of impurities was found. The peaks were indexed with respect to the pseudo-cubic structure of the material since the rather small rhombohedral distortion (rhombohedral angle $\alpha_r = 60.36^\circ$) of the crystal lattices could not be measured with the given resolution. The pseudo cubic lattice parameter of LSC ($a_{pc} = 3.842 \pm 0.003 \text{ \AA}$) derived from the polycrystalline target diffraction patterns in good agreement with literature values⁵. The thin film pattern shows the actual thin film growth relative to the (100) YSZ plane. Therefore, the pattern overlaps with the intense (200) and (400) peaks of the substrate. Only YSZ and LSC thin film peaks are found, indicating a phase-pure deposition. Furthermore, it can be seen that the textured film grows preferentially in (100) and (110) direction. Grains grown in (111) direction are also observed. Due to the small size of thin film peaks the out-of-plane lattice parameters of LSC ($a_{pc} = 3.83 \pm 0.01 \text{ \AA}$) can only be deduced with limited accuracy.

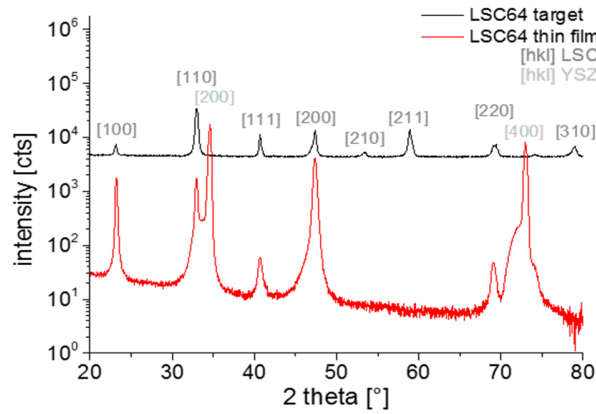


Fig. 4.2 XRD diffraction pattern of LSC target and thin film deposited on YSZ.

4.3.2 Surface cation chemistry and performance of as-deposited LSC thin films

LEIS and ICP-MS were first used to investigate the cation composition of freshly deposited samples. Fig. 4.3 shows the “Sr / A-Site” and “Co / A-site” ratio as a function of depth for an as-deposited sample measured by LEIS. A sputter dose of about $1.5 \cdot 2 \cdot 10^{15}$ ions/cm² was used so it can be assumed that between each analysis cycle (measurement point) approximately 1 atomic layer was removed. However, the sputter process can cause cation intermixing, thus hindering an exact interpretation in terms of atomic layer composition for all layers except the surface layer (i.e. for the first analysis cycle, the analysis beam dose was kept below the static limit, assuring that less than 1 % of the surface is bombarded and minimizing the surface damage). The cation composition of the target is highlighted by the dotted lines.

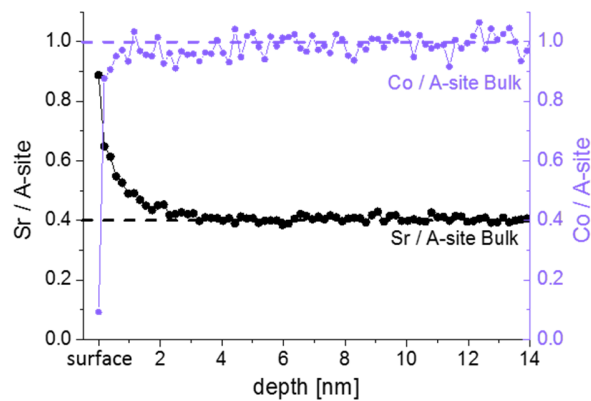


Fig. 4.3 LEIS depth profile of as-deposited LSC thin film showing Sr / A-site and Co / A-site ratio.

It can be seen that in the first 3 nm the cation stoichiometry does not fit to the bulk stoichiometry. A Sr enrichment close to the surface together with a Co depletion is found. Sr segregation may occur during the PLD process (at 600 °C) or the subsequent slow cooling phase since cations are sufficiently mobile at these temperatures as reported in ref. ⁵⁶. Cai et al. also found a Sr-rich and Co-depleted region close to the surface of LSC on as-deposited samples by XPS measurements³². Other authors also reported cation rearrangements at the surface of perovskites during thin film growth^{109, 110}.

The surface layer, represented by the very first measurement point in Fig. 4.3, shows the highest Sr occupancy. 81 % of the surface cation sites are occupied by Sr ions. Furthermore, almost no cobalt is found in the termination layer, while the next measurement points indicate a Co / A-site ratio close to the bulk values of one. The very Sr-rich termination layer is not necessarily a true part of the LSC perovskite lattice. A SrO termination layer on top of the LSC film could also correspond to an AO layer of the so called Ruddlesden-popper structure ($ABO_4 = ABO_3 \cdot AO$). A rocksalt AO termination layer was also assumed for other single perovskites ($La_{0.6}Sr_{0.4}Co_{0.2}Fe_{0.8}O_{3-\delta}$ ¹⁰⁴) and double perovskites ($PrBaCo_2O_{5+\delta}$, $GdBaCo_2O_{5+\delta}$ ¹⁰⁵) with the transition metal of the double perovskites being buried below the surface layer. Further interaction of this layer with CO_2 and H_2O (i.e. $SrCO_3$, $Sr(OH)_2$) might be possible^{111, 112}.

Additionally, ICP-MS measurements were conducted on as-deposited thin films, see Fig. 4.4. Different eluents continuously dissolved parts of the LSC films and in Fig. 4.4a the cation concentration of the eluate, as detected by the mass spectrometer, is plotted against the measurement time. The eluent used for the extraction of the LSC cations was switched from ultrapure H_2O to diluted 0.012 mol/l hydrochloric acid after 360 seconds, which is also highlighted in the graph. In the beginning of the experiment, when H_2O is used as eluent, a sharp peak of the cation signals is observed. This indicates that only a limited amount of water-soluble cations exists on top of the thin films. The amount of water-soluble cations can be determined by standard calibration and integration over the H_2O peak (0.65 nmol Sr, 0.46 nmol Co and 0.16 nmol La). From the lattice parameter it can be calculated that 0.33 nmol Sr would be needed to form one atomic layer of SrO covering the entire $5 \times 5 \text{ mm}^2$ surface of the thin film. This means that the etching procedure does not only dissolve the very Sr-rich surface layer found in LEIS. In the given example, the additionally dissolved cations would correspond to about two elementary cells of LSC covering the projected area of $5 \times 5 \text{ mm}^2$. Effects of the enhanced surface area e.g. due to cracks are discussed in chapter 3.4. As soon as the eluent is switched to dilute HCl, without interrupting the

continuous eluent flux, a small La peak is observed and indicates that the ultrapure water possibly preferentially dissolved Sr and Co. During the course of the HCl etching the cation concentration again increases and reaches a rather constant level after 120 seconds.

The composition changes detected in the course of the etching procedure and thus over the thin film depth can be much better understood when plotting the molar ratio of the cations versus the sum of all cations detected by the mass spectrometer, Fig. 4.4b. Assuming that the thin film is etched homogenously, the total cation amount can be directly translated into a depth. In the case of LSC64, 1 nmol of cations corresponds to 0.78 nm LSC. In this plot it can again be seen that the ultrapure water primarily dissolves Sr and Co. After switching to diluted HCl a sharp peak of La is observed. The expected bulk stoichiometry is found after extraction of 7.5 nmol cations. This work, however, will mainly focus on the water soluble part detected by the ICP-MS as it gives most information on the surface and near-surface cation composition of our thin films.

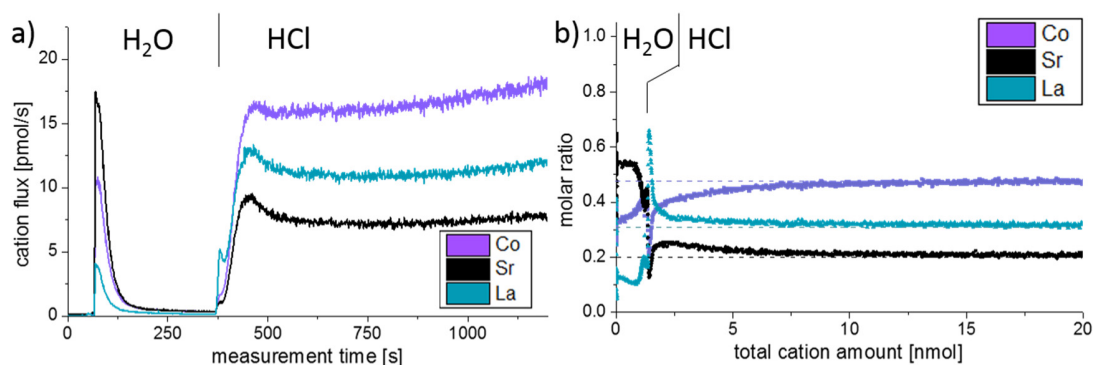


Fig. 4.4 ICP online analysis of as-deposited LSC thin film, displaying the measured cation flux (a) and the cation molar ratio vs. total amount of etched cations from the measured data (b). For a dense thin film 20 nmol of LSC correspond to 15.6 nm thick LSC layer.

4.3.3 Annealing of as-deposited thin films

A decrease of the electrochemical performance of LSC thin films and related materials with annealing time was often reported and mostly connected to stoichiometry changes at or close to the surface. It is known that Sr surface segregation can be chemically driven by atmospheric trace gases such as SO₂, CO₂ or H₂O³⁷⁻³⁹. Furthermore, the presence of a Si or Cr source in the vicinity of a perovskite sample together with a wet atmosphere were also shown to lead to strontium

precipitation on the surface^{40, 41}. Therefore, special care was attributed to avoidance of any contamination of the atmosphere during the annealing procedure, see chapter 4.2.2.

An as-deposited sample with two symmetrical LSC electrodes was annealed at 600 °C for 15 h in synthetic air and impedance spectra were continuously taken. Representative Nyquist plots normalized to the projected electrode surface area shown in Fig. 4.5. The high-frequency (>50 kHz) intercept can be attributed to the oxide ion conduction of the electrolyte. Small differences of the intercept between the spectra most probably originate from temperature fluctuations (± 1 °C) during the measurement. At medium frequencies (50 kHz – 1 kHz) a shoulder appears next to a low frequency semicircle (1 kHz to 0.1 Hz). The shoulder was already reported in earlier studies⁶⁵, where it could be attributed to electrochemical processes at the electrode/electrolyte interface. The low frequency semicircle is the only part of the spectra that changes its shape or size with annealing time. It could be fitted to a parallel R-CPE element (CPE = constant phase element with exponential fitting parameter $n \sim 0.9$). The capacitive element can be assigned to the chemical capacitance C_{chem} of the thin film according to the model of Jamnik-Maier⁶⁷. The values of C_{chem} are approx. $984 \pm 96 \text{ F/cm}^3$ and thus in the typical range found for LSC thin film electrodes. The resistance can be attributed to the oxygen surface exchange reaction, $R_{\text{surface exchange}}$ ⁶⁵. Despite all precautions taken to avoid any cathode poisoning, $R_{\text{surface exchange}}$ continuously increases from 0.6 to $4.6 \text{ } \Omega\text{cm}^2$ within 15 hours of annealing time. One may suppose that still strong Sr segregation was caused by an unknown poisoning process. Therefore the surface chemistry of the annealed thin films was investigated by LEIS and ICP-MS.

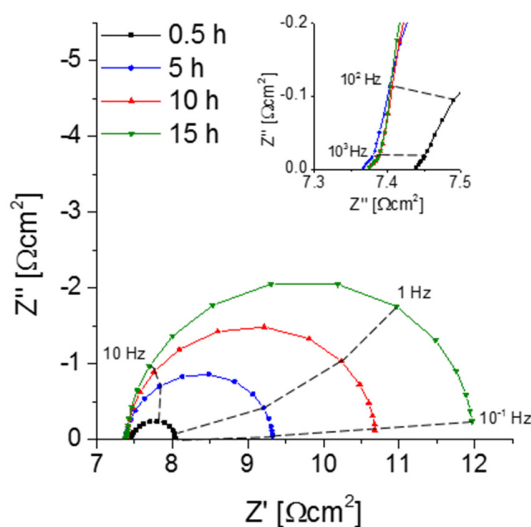


Fig. 4.5 Nyquist plot displaying the impedance change of a symmetrical deposited sample upon annealing at 600 °C, the inset shows the middle-frequency (50 kHz – 1 kHz) range in detail.

LEIS and ICP-MS measurements were performed on LSC thin films that were annealed for 1, 4 and 16 hours in the same experimental setup, results are given in Fig. 4.6 and 4.7. Interestingly, the LEIS depth profiles do not show any significant changes of the cation stoichiometry. The depth profiles of the annealed thin films are almost identical to those of the as-deposited thin film. Only an even smaller Co coverage is found on the surface for the 16 h annealed thin film. Fig. 4.7 summarizes the amount of water soluble cations for the differently annealed thin films measured by the ICP-MS. For each annealing time three samples were investigated and the error bars are obtained from the standard deviation. Again, no significant changes are found, except for a slight increase of the Sr amount during the first hour of annealing. Overall, none of the chemical analysis methods indicated substantial surface composition changes that reveal a simple correlation to the strong decrease of the oxygen surface exchange kinetics. From a compositional point of view, the thin film surface layer seems to be in a frozen-in state or already close to an equilibrium state without much driving force to change the surface structure.

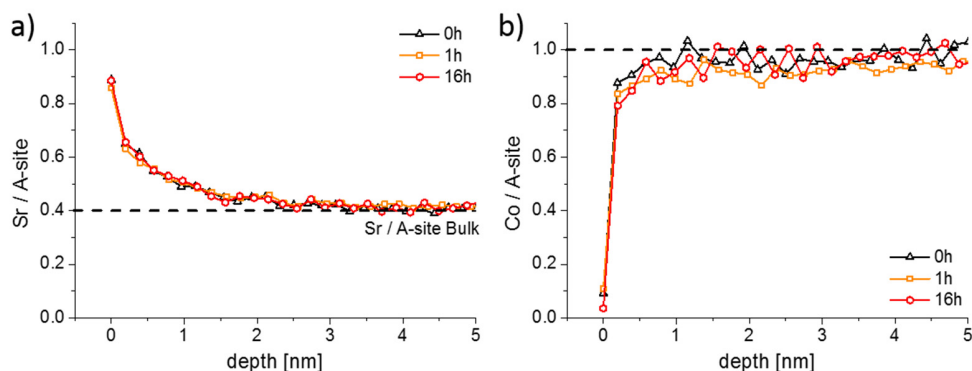


Fig. 4.6 LEIS depth profiles showing the Sr / A-site (a) and the Co / A-site (b) ratio of an as-deposited sample and of two samples that were annealed at 600 °C for 1 and 16 h.

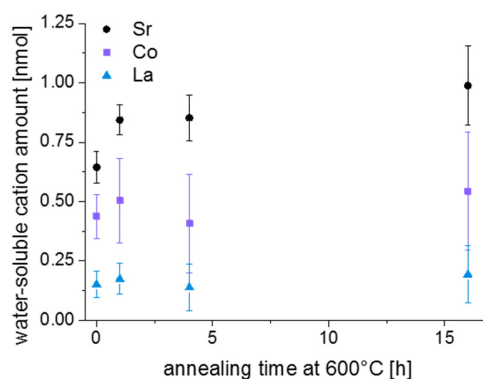


Fig. 4.7 H₂O soluble amount of cations detected by ICP-MS on a freshly deposited sample and on samples that were annealed for 1, 4 and 16 h at 600 °C.

4.3.4 Surface treatment of as-deposited thin films

In chapter 4.3.2 it was shown that Sr-rich layers of the LSC thin film could be removed by water during the ICP-MS measurements. This process of surface modification and its reversibility by short heat treatments was further investigated by LEIS and ICP-MS. First, several as-deposited samples were stirred ex-situ for 10 min in ultrapure H₂O in order to remove the water soluble layers. The samples were subsequently dried in a pure nitrogen gas stream. Two samples were then analyzed by LEIS and ICP-MS. The other samples were annealed for 1 h at 600 °C in syn. air and also chemically analyzed. These steps were repeated with chemical analysis by LEIS. All cation compositions measured by LEIS are shown in Fig. 4.8.

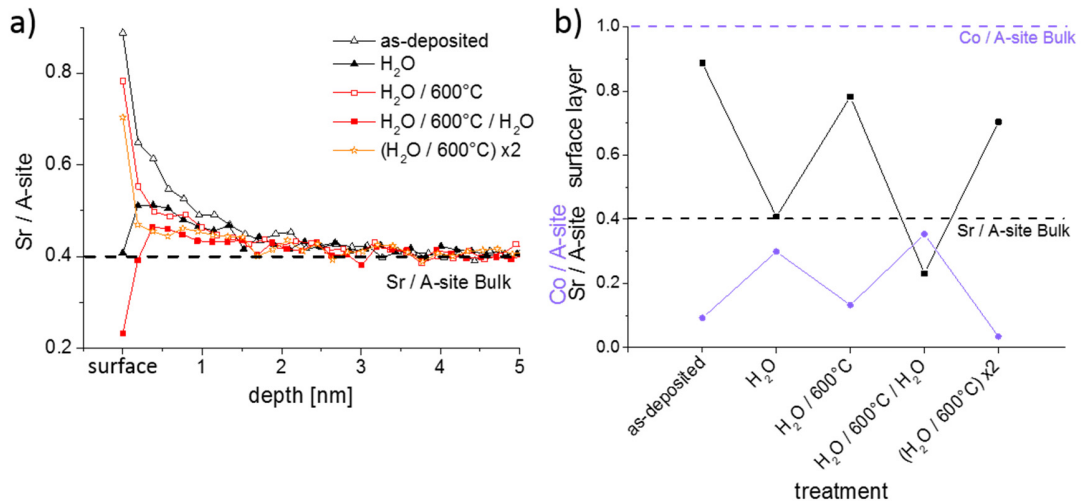


Fig. 4.8 (a) LEIS depth profiles showing the Sr / A-site ratio after different surface treatments; (b) Co / A-site and Sr / A-site ratio of the termination layer is displayed after different surface treatments.

Fig. 4.8a displays the LEIS depth profiles of the Sr cation composition, while Fig. 4.8b focusses on the Co / A-site and Sr / A-site ratio of the surface termination layer, i.e. the very first measurement points in Fig. 4.8a. After the first H₂O treatment the Sr level of the termination layer is strongly reduced. Simultaneously, a substantially higher amount of Co is measured in the termination layer. However, the Co amount is still far from bulk stoichiometry. The remaining part of the termination layer consists of La. The Sr enrichment in the near-surface layers is reduced but still present. This nominal decrease of Sr content in subsurface layers by the ex-situ H₂O etching can be partly attributed to the fact that H₂O removes more than the surface termination layer, similar to the results observed by time resolved ICP-MS using H₂O as eluent (cf. chapter 4.3.2). During the annealing of a H₂O treated sample for 1 h at 600 °C, Sr segregates back to the top of LSC leading

to about 70 % Sr ions with respect to the total cation amount in the termination layer. Except from the termination layer the Sr depth profiles of the H₂O treated and the H₂O treated + 600 °C annealed samples are almost identical. The absence of any Sr depletion in the first 5 nm of the annealed thin film raises the question from where the Sr segregates back to surface. This will be addressed in chapter 4.3.5. After a renewed exposition of an annealed thin film to ultrapure water for 10 min, the Sr depletion at the surface is again found. This time the Sr surface coverage even drops lower and the Co coverage is once more increased compared to the annealed sample. Another annealing step at 600 °C for 1 h brings the Sr-rich and Co-poor termination layer back. Again, no Sr depletion could be detected in the first few nm. These experiments confirm that formation of a Sr-rich surface layer is an equilibrium property of LSC. This layer is water soluble and cation diffusion kinetics is sufficiently fast to reestablish the termination at 600 °C in less than one hour.

The effect of H₂O treatment and annealing was also investigated by ICP-MS in order to obtain information on the layer composition and on the true cation amounts that were removed and reseggregated to the top of the thin films. The results are shown in Fig. 4.9a, together with the LEIS depth profiles plotted in a different manner. The LEIS depth profiles indicate the measured cation stoichiometry in the first 5 nm for three different surface treatments. Fig. 4.9b displays the amounts of each cation in the “water peak” of the ICP-MS measurements (cf. chapter 4.3.2). Three samples were investigated for each sample treatment to ensure reproducibility, as reflected by the error bars.

For the as-deposited sample, mainly Sr and Co are dissolved in ultrapure H₂O, cf. first data points in Fig 4.7. Qualitatively, the composition measured by ICP-MS (high Sr, low La) corresponds to that of the top layer analyzed by LEIS. Quantitatively, there are differences due to the fact that the “water peak” dissolves more than only the termination layer, see chapter 4.3.2. Also after the ex-situ H₂O treatment of the as-deposited sample cations are dissolved during the time resolved ICP-MS etching using H₂O (see Fig. 4.9 center). This is surprising since not only ex-situ H₂O treatment but also time resolved etching are performed using ultrapure water and should not dissolve further ions. Both, the dissolution of ions in addition to the Sr-rich termination layer of the as-deposited film and the dissolution of LSC after ex-situ H₂O treatment may be explained by the following: Trace gases, e.g. CO₂, adsorb at sample surface before ICP-MS analysis. Those can form acids in combination with the eluent (H₂O) used during the ICP-MS measurement. This can then lead to an additional dissolution of cations from the LSC lattice, which comes to an end as soon as

all adsorbates are consumed. These trace gases from ambient air are expected to desorb at higher temperatures and are therefore irrelevant for the electrochemical measurements performed in a constant flow of high purity gases. For the H₂O treated sample a decreased amount of soluble Sr is found within the ICP-MS eluate compared to the as-deposited sample while for the other cations no relevant changes were observed. This strongly suggests that the main difference between surface composition of an as-deposited and a H₂O treated layer is the absence of a very Sr-rich layer in the latter case.

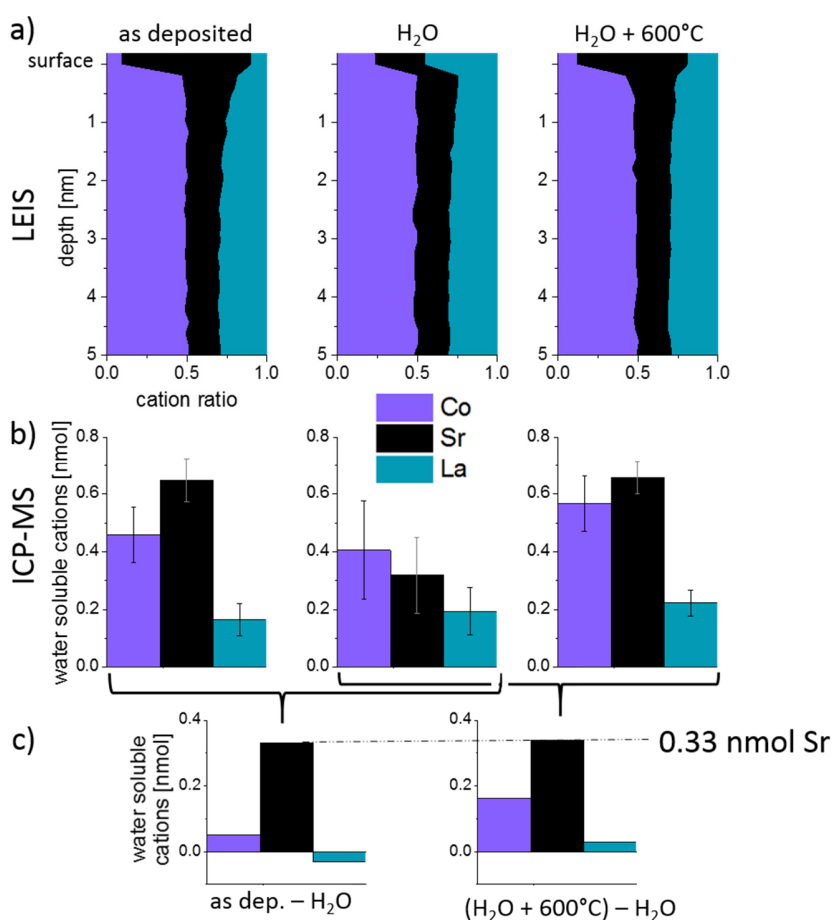


Fig. 4.9 (a) Cation composition of LEIS depth profiles, (b) amount of water-soluble cations measured by ICP-MS on samples after different surface treatments and (c) differences between the amounts of water-soluble cations found by ICP-MS. On top of the as-deposited and the annealed thin film an excess amount of 0.33 nmol Sr is found in comparison to the H₂O treated thin film.

After the H₂O treated sample is annealed at 600 °C for 1 h in synthetic air, again a Sr-rich eluate is measured by the ICP-MS in accordance with the high Sr surface coverage found by LEIS. The different amounts of water-soluble cations obtained for the H₂O treated + annealed sample

corresponds well to the amounts found for the as-deposited sample. Since the “water peaks” in ICP-MS also include cations of sub-surface layers, it is most interesting not to focus on the absolute cation amounts but on the differences between the surface treatments (Fig. 4.9c). Significant differences (confidence interval of ~90 %) are only found for Sr and, as highlighted in Fig. 4.9, this difference amounts to ca. 0.33 nmol Sr that is removed during H₂O treatment and segregated back to the surface after annealing. As already mentioned above, 0.33 nmol of Sr is exactly the amount needed to form one layer of (100) SrO on top of the 5x5 mm² thin film.

LEIS results, however, show that the surface layer is Sr-rich but does not entirely consist of Sr. The difference can be at least partially explained by the different surfaces investigated by the two techniques. While LEIS results reflect the cation composition of the projected surface, the eluent used in the water treatment and analysis during ICP-MS dissolves cations from the true surface. The true surface area is enlarged i.e. by the cracks shown in Fig. 4.1 and an area increase of about 30 % compared to the projected surface area would already explain the measured difference. This comparatively small enhancement of the surface area by cracks is also in accordance with the study on the thickness dependency of the surface exchange resistance and water soluble Sr amount found on the surface of similar thin films in chapter 2. Furthermore, H₂O does not necessarily dissolve the thin film homogeneously. A preferential cation dissolution at grain boundaries may further affect the data. Nonetheless, both analytical techniques present a very similar picture of the cation composition at and close to the surface.

The quick reappearance of a Sr-rich surface termination at 600 °C after its removal in H₂O raises the question of the kinetics of Sr diffusion and segregation. Annealing of H₂O treated samples was therefore performed at different temperatures for 1 h. The LEIS results of Fig. 4.10 show that thin films annealed up to 400 °C for 1 h do not show any significant differences in the composition of the surface. Neither the surface composition (Fig. 4.10b) nor the depth profile (Fig. 4.10a) is modified by annealing up to 400 °C. The depth profiles of these thin films also underpin the reproducibility of the H₂O treatment since all measurements were performed on different thin films. The thin film annealed at 550 °C, on the other hand, again exhibits a Sr-rich and Co-poor termination layer. This is even more pronounced after annealing at 600 °C: Then 69 % of surface cations are Sr, compared to 51 % after annealing at 550 °C. At 550 °C Sr re-segregation was most probably not completed yet after 1 hour.

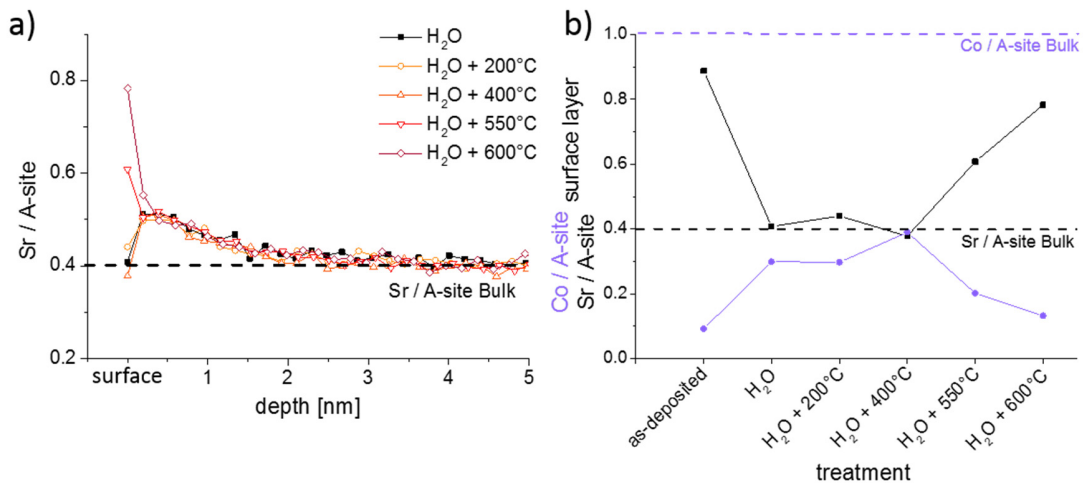


Fig. 4.10 (a) LEIS depth profiles showing the Sr / A-site ratio after annealing thin films for 1 h at different temperatures; (b) Co / A-site and Sr / A-site ratio of the termination layer of the same thin films.

The exact mechanism and the rate limiting step of Sr segregation is not clear yet. The substantial amount of Sr needed for the measured Sr-rich surface termination has to lead to some Sr depletion in the film. However, such a depletion was not observed within the first 5 nm of any annealed LSC thin films (Fig. 4.10a) and thus fast Sr diffusion with only slight depletion in larger parts of the film are concluded. Significant Sr tracer diffusion profiles were already reported at 650 °C in Ref. ⁵⁶ and quantitative data on fast diffusion along grain boundaries and bulk were deduced. Since ambipolar diffusion coefficients are expected to be much larger than the tracer diffusion coefficients⁵⁶, this is in accordance with our results.

4.3.5 Influence of the termination layer on the ORR

To investigate whether the Sr-rich termination layer promotes or inhibits the oxygen surface exchange reaction, impedance measurements were performed on as-deposited thin films and thin films after H₂O treatment at 400 °C, Fig. 4.11. Both Nyquist plots show the electrode impedance dependency on the oxygen partial pressure. For all partial pressures, two main features in the impedance spectra can be distinguished. At high frequencies (>1 kHz) the onset of a semicircle is observed, which represents the ionic conductivity of the YSZ electrolyte. This part of the spectra was not visible in Fig. 4.5, because of the higher measurement temperature and thus a higher bulk relaxation frequency which is proportional to the ionic conductivity. It can also be seen that the

ionic resistance of the electrolyte does not change upon oxygen partial pressure variations. The second feature at lower frequencies (<1 kHz) originates from the electrode.

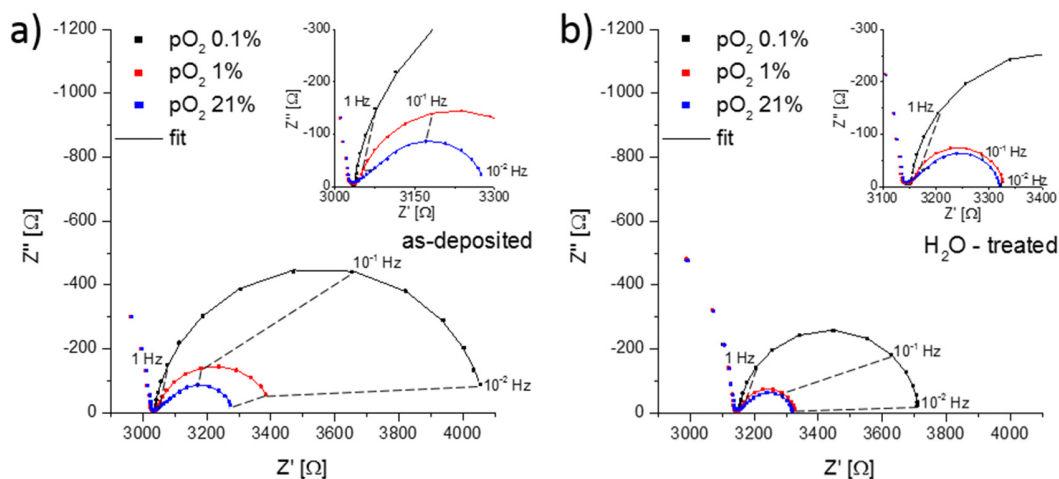


Fig. 4.11 Nyquist plots showing the dependence of the electrode impedance on the oxygen partial pressure for an (a) as-deposited and (b) H₂O-treated thin film. Measurements were performed at 400 °C in different N₂ / O₂ mixed atmospheres.

At oxygen partial pressures of 210 mbar (21 % O₂ = syn. air) the electrode impedance part has a semi-tear drop shape and for both samples it can be fitted to a finite Warburg element. For mixed conducting electrodes this is often an indication that transport of a charge carrier is rate-limiting. LSC is believed to show a metal-like electronic conductivity, therefore only the oxygen conductivity could be responsible for transport limitation. Additional effects including an ionic charge transfer resistance into YSZ or sample inhomogeneities may affect the spectrum shape and pure transport limitation cannot be necessarily concluded, see also the interpretation of the impedance spectra of LSC thin films measured at such low temperatures in Ref.¹¹³. However, most probably the surface exchange resistance does not dominate the entire electrode resistance under these conditions. In order to truly investigate the influence of the LSC termination layers on the oxygen surface exchange kinetics, other oxygen partial pressures are therefore more adequate. A reduction of the oxygen partial pressure accelerates the oxygen transport through the LSC thin film, due to an increase of the oxygen vacancy concentration, and it simultaneously slows down the oxygen exchange kinetics. This can be observed in Fig. 4.11a and 4.11b, as the electrode part of the impedance spectra changes its shape to a semicircle for lower oxygen partial pressures. At an oxygen content of 0.1 % it can be safely assumed that the surface exchange resistance dominates the overall electrode reaction and further investigation were done in this atmosphere.

The impedance spectra at a normalized oxygen partial pressure (pO_2) of 0.1 % were again fitted to a parallel RC-element with R being the oxygen surface exchange resistance. Multiple samples were investigated for statistics. The obtained surface exchange resistances for differently treated samples annealed at 400 °C and 600 °C for 16 h are plotted in Fig. 4.12.

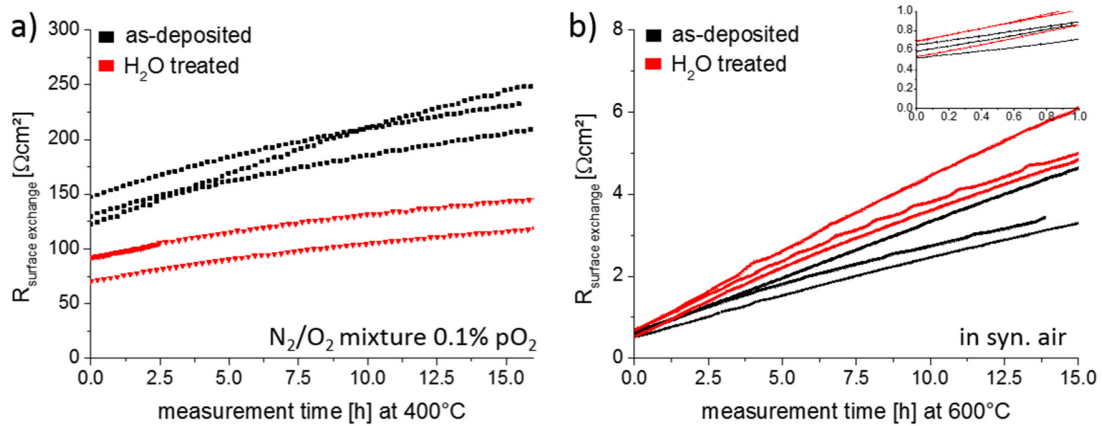


Fig. 4.12 Variation of the surface exchange resistance for as-deposited and H₂O treated thin films with annealing time. Measurements were performed (a) at 400 °C in 0.1 % pO_2 and (b) at 600 °C in 21 % pO_2 .

For the thin films annealed at 400 °C, Fig. 4.12a, a clear difference between the surface exchange resistance of as-deposited and H₂O treated thin films is visible. In the beginning the oxygen exchange kinetics, represented by $1/R_{\text{surface exchange}}$, is promoted by ~60 % when removing the Sr-rich and Co-poor termination layer. On the contrary, the initial values of the thin films annealed at 600 °C, inset of Fig. 4.12b, do not indicate any difference between the films. The latter can be easily understood since prior to the start of the impedance measurements each sample was thermally equilibrated for 1 h in the corresponding atmosphere. Hence, the removed Sr-rich termination layer already reappeared before the impedance measurement started, cf. chapter 4.3.4 and Fig. 4.13. These measurements are also an indication of the excellent reproducibility of our film surfaces with $R_{\text{surface exchange}} \approx 0.6 \Omega\text{cm}^2$ at 600 °C. At 400 °C, on the other hand, cations are considered to be immobile on the time scale of an hour as shown in chapter 4.3.4. The influence of a non-equilibrated termination layer on the surface exchange resistance can therefore be measured.

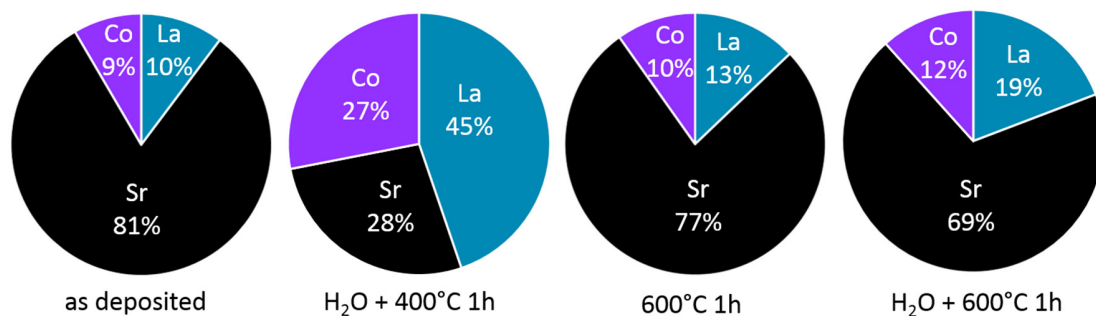


Fig. 4.13 Cation composition of the termination layer measured by LEIS for as-deposited LSC and after different thermal and chemical treatments.

The enhanced oxygen exchange kinetics observed for the non-equilibrated termination layer can have multiple reasons and is discussed based on the surface composition shown in Fig. 4.13. The SrO (or Sr(OH)₂) termination layer that forms on top of the LSC could simply block the oxygen from approaching active sites that are important for the oxygen reduction reaction. Assuming active sites being proportional to the surface parts without Sr termination suggest an increase from 19 % to 72 % and this is even more than the 1.6 factor found for the enhancement of the oxygen exchange kinetics. This argumentation does not consider details of the mechanism. Active sites may be either related to the accessibility to oxygen vacancies for adsorption, dissociation and diffusion of oxygen²⁸ or the possibility to approach B-site cations. Instead of the Sr decrease one may therefore consider the concentration increase of the other two cations, i.e. La and Co. Lanthanum is assumed to play only a role as a host atom that is substituted by Sr and does not take part in the oxygen reduction reaction. Cobalt, on the other hand, is known to facilitate the electronic conduction in LSC by constituting a conduction band via its 3d and oxygen 2p orbitals¹¹⁴⁻¹¹⁶. Thus the importance of surface Co atoms for charge transfer is therefore very realistic²³. If any charge transfer from the Co to an oxygen surface species is rate determining for the oxygen reduction reaction, the increased Co content after H₂O treatment could explain the improved surface exchange kinetics. Moreover, the kinetics change might also be not only stoichiometry related. Z. Cai and co-workers³² found a change of the Co oxidation state from Co²⁺ to Co³⁺ close to the Sr-rich surface of LSC using XPS and suggested a detrimental role of this valence change on the oxygen exchange kinetics.

Finally, the time dependence of the surface exchange resistance in Fig. 4.12 is discussed. At 600 °C, the degradation phenomenon was already shown for an as-deposited thin film in chapter 4.3.3. An average resistance increase by a factor of 6.7 after 15 hours of annealing is found. The

degradation of the H₂O treated thin film is very similar with a surface exchange resistances changed by a factor of 8.3 after 15 hours of annealing. These strong changes without much variation of the Sr coverage further question the existence of a simple relation between oxygen exchange kinetics and Sr surface coverage under very clean atmospheric conditions. The resistance increase at 400 °C is much less pronounced and amounts to a factor of 1.7 and 1.6 for as-deposited and H₂O treated films. The slower degradation may simply be an effect of temperature but could also be influenced by the atmosphere. In some earlier unpublished work it was observed that a lower oxygen partial pressure during annealing led to less degradation at the same annealing temperatures. For a clear mechanistic explanation of the degradation much further measurements are needed. However, one may speculate that the remaining Co concentration at the surface is most decisive. Degradation would then be caused by covering substantial parts of the still remaining small amounts of surface Co (cf. Fig. 4.6b). Hence, the most beneficial effect of the water treatment would be exposing more Co to the gas phase.

4.4 Conclusions

Surface sensitive measurements were performed by LEIS and time resolved ICP-MS to analyze the cation composition of La_{0.6}Sr_{0.4}CoO_{3-δ} thin film electrodes. Results obtained by both methods agree qualitatively and quantitatively and provide a consistent picture of the surface termination composition and cation diffusion kinetics. For as-deposited LSC thin films a water-soluble Sr-rich and Co-poor termination layer was found. While the Co depletion is only observed in the termination layer, the Sr is enriched in the first 3 nm of LSC. The surface layer is removed by treating the sample in ultrapure water, but ca. 1 monolayer of SrO repeatedly forms again whenever the sample is annealed at or above 550 °C for 1 h. A Sr depletion in subsurface regions was not found, thus very fast Sr diffusion with only slight depletion in larger parts of the film are concluded. These experiments confirm that formation of the Sr-rich surface layer is an equilibrium property of LSC and that Sr diffusion does not limit its formation under these conditions. Impedance measurements at 400 °C revealed the detrimental effect of this surface layer on the oxygen surface exchange and suggest that higher Co concentration in the termination layer facilitate the oxygen exchange reaction. Further annealing of thin films with Sr-rich termination layer in poison-free atmosphere at 600 °C did not lead to any significant cation composition changes although the oxygen surface exchange kinetics continuously decreased.

5 Impedance spectroscopy during PLD revealing large changes of the oxygen reduction activity by small amounts of cations

This chapter contains in large parts material submitted as a scientific paper to Nature Materials.

5.1 Introduction

Degradation of the electrochemical oxygen exchange kinetics was also found for other perovskite-type materials such as $(\text{La,Sr})\text{MnO}_{3-\delta}$ ^{29, 30, 117}, $(\text{La,Sr})(\text{Co,Fe})\text{O}_{3-\delta}$ ^{31-33, 49, 118}, $\text{Sr}(\text{Ti,Fe})\text{O}_{3-\delta}$ ^{34, 35} and $(\text{Ba,Sr})(\text{Co,Fe})\text{O}_{3-\delta}$ ³⁶ and it is often connected to a Sr enrichment in the surface region. Moreover, the ORR kinetics can be strongly deteriorated by precipitates caused by contaminants in the gas phase^{37, 38}. However, it is still unclear how surface segregates or precipitates affect the catalytic activity. Sr segregation, for example, may either passivate the entire electrode surface by forming a dense insulating SrO (or $\text{Sr}(\text{OH})_2/\text{SrCO}_3$) layer or may block specific reactive sites important for the ORR. Degradation was even observed without a measurable change of the cation surface stoichiometry, see chapter 4.3.3. So far, gaining a better understanding of the correlation between surface composition and surface ORR kinetics was hampered by the experimental decoupling of surface modification, surface analysis and investigation of surface properties. Furthermore, effects of well-defined surface modification by very small amounts of cations were hardly investigated yet¹¹⁹.

In the course of this thesis a novel approach was developed to investigate and change the performance of LSC thin film electrodes. Instead of chemical post-analysis of degraded electrode thin films, the LSC surface was deliberately modified by depositing defined amounts of its cation constituents. Several studies already modified the LSC surface by a wet-chemical route¹¹⁹ or deposition of larger amounts (several nm) of oxides via pulsed laser deposition (PLD)^{45, 101}. However, in contrast to those studies, a new technique was employed to carry out surface modification and electrochemical characterization simultaneously: In-situ impedance spectroscopy measurements inside a pulsed laser deposition chamber (IPLD) while depositing SrO, Co_3O_4 and La_2O_3 , see Fig. 5.1. This allows reliable monitoring also of very small changes of the electrochemical response by tiny amounts of cations, while guaranteeing that the surface does

not change between modification and electrochemical characterization. Quantification of the surface deposits was performed by means of calibration curves using inductively coupled plasma-mass spectrometry (ICP-MS). Applying a single laser pulse onto a SrO target effectively deposits only ~ 4 % of a SrO monolayer on the LSC electrode surface but already severely decreases the ORR kinetics. Moreover, it could be experimentally verified that the accessibility of surface Co strongly improves the oxygen exchange kinetics. These observations are summarized in a new model of active and inactive sites for ORR on LSC.

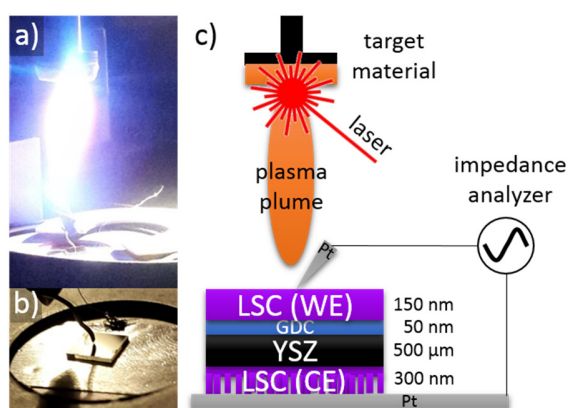


Fig. 5.1 The in-situ impedance setup for PLD (IPLD): (a) Setup during the ablation of target material with the sample positioned below the target and plasma plume. (b) Sample with the macroscopic 5 x 5 mm² dense LSC working electrode contacted by a Pt tip from above and the porous LSC counter electrode connected to a Pt sheet (c) Sketch of the entire setup.

5.2 Experimental

5.2.1 Target preparation and characterization

The La_{0.6}Sr_{0.4}CoO_{3-δ} (LSC) target for pulsed laser deposition (PLD) was synthesized according to the Pechini route⁶². La₂O₃, SrCO₃ and Co powders (all Sigma Aldrich, 99.995 %) were individually dissolved in nitric acid, mixed in appropriate ratios and citric acid (TraceSELECT®, 99.9998 %) was added for chelation. A calcination step was performed at 1000 °C in air, followed by isostatical pressing (150 MPa) of the powder to a pellet and a sintering procedure at 1200 °C for 12 hours in air. The exact target composition (La_{0.607±0.008}Sr_{0.396±0.004}Co_{0.996±0.005}O_{3-δ}) was determined from thin films grown by PLD on YSZ, which were dissolved in hydrochloric acid and analyzed by Inductively Coupled Plasma – Optical Emission Spectroscopy. The Ce_{0.8}Gd_{0.2}O_{2-δ} (GDC) powder (Treibacher Industrie AG, Austria) was isostatically pressed (240 MPa) and sintered for 10 hours at 1550 °C in air to yield a PLD target. The “La”, “Sr” target were prepared from La₂O₃, SrO powder which were

calcined in a Platinum crucible at 800 °C and 1200 °C, respectively, for 12 hours in a constant flow of high purity O₂ (ALPHAGAZ™ 1 >99.998 mol% oxygen) to decompose any hydroxyls or carbonates. After cooling down to room temperature in the same atmosphere, the powders were grinded and isostatically pressed within an hour and the pellets sintered again at 1200 °C (“La”) and 1300 °C (“Sr”) for 12 hours in a flux of high purity O₂. For the “Co” target, Co₃O₄ powder was grinded, isostatically pressed and the pellet sintered at 1200 °C for 12 hours in ambient air. A SrO single crystal purchased from SurfaceNet (Rheine, Germany) was used as “Sr (sc)” target. All targets were glued to target holders and the glue was cured at 180 °C for 4 hours in a flux of high purity O₂. All targets except from the LSC target were stored in a vacuum desiccator filled with silica gel (H₂O adsorbent) and freshly annealed SrO (H₂O & CO₂ getter) and transferred into the PLD immediately before evacuating the PLD recipient to avoid/reduce degradation of the materials.

The polycrystalline PLD targets were analyzed in Bragg Brentano geometry by a X'Pert Powder (PANalytical) diffractometer. Diffraction patterns are shown in Fig. 5.2 and allowed to determine the phase compositions. For sake of simplicity particles deposited from the non-phase pure “Sr” target (87 at% SrO, ~10 at% Sr(OH)₂, ~3 at% Sr₄PtO₆) were assumed to be pure SrO. The exact chemical composition of the deposited materials, however, was not accessible; it could only be determined reliably by a chemical in-situ analysis in the PLD chamber.

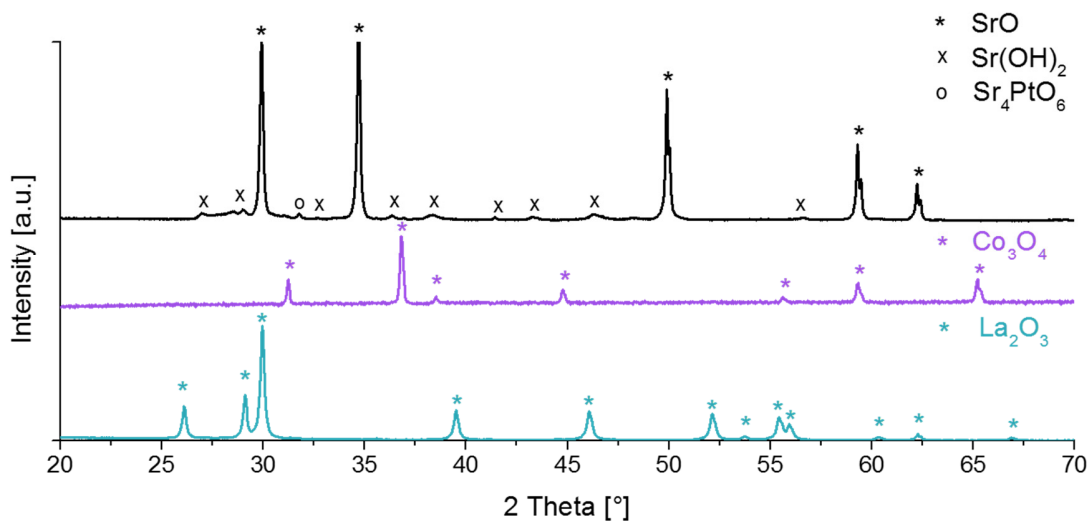


Fig. 5.2 X-ray diffraction patterns of polycrystalline “La”, “Co” and “Sr” target. “La” and “Co” target consists exclusively of La₂O₃ and Co₃O₄, respectively. For the “Sr” target different phases were found: 87 at% SrO, ~10 at% Sr(OH)₂ and 3 at% Sr₄PtO₆. The Sr₄PtO₆ was formed during calcination of the SrO powder or sintering of the target pellet in the Pt crucible.

While formation of hydroxides and carbonates is assumed to be unlikely inside the PLD because of the high purity oxygen used and the negligible nominal partial pressures of CO₂ and H₂O ($p_{\text{CO}_2} = 2.5 \cdot 10^{-10}$ bar and $p_{\text{H}_2\text{O}} = 1.5 \cdot 10^{-9}$ bar), ex-situ XPS analysis of as-prepared and decorated thin films indicated the presence of hydroxyls and carbonates on the surface. It is assumed that LSC and the deposited oxides, especially SrO, react with moisture and CO₂ of the ambient atmosphere as soon as the samples are removed from the PLD recipient. Apart from this result, XPS measurements (see chapter 5.5.4) qualitatively and semi-quantitatively confirmed the quantitative results found by ICP-MS.

5.2.2 Sample preparation

For the preparation of the samples, first dense ~55 nm thin Ce_{0.8}Gd_{0.2}O_{2-δ} buffer layers and dense ~140 nm thin LSC layers were deposited onto (100) oriented yttria stabilized zirconia (YSZ, 9.5 mol% Y₂O₃, Crystec GmbH, Germany) single crystals with a thickness of 0.5 mm and a size of 5x5 mm². These layers were used as working electrode of the electrochemical cells. Ablation of target materials was carried out by a KrF ($\lambda = 248$ nm) excimer laser (Lambda COMPexPro 201F) operated at a pulse repetition rate of 5 Hz, a pulse duration of 50 ns and a laser fluence of approximately 1.5 J·cm⁻² at the target. The atmosphere was set to 4·10⁻² mbar oxygen partial pressure (constant flux of high purity O₂) and the substrate was heated to a surface temperature of 600 °C. About 1,500 and 6,750 laser pulses were applied to the GDC and LSC target, respectively, with a constant substrate to target distance of 6 cm. After deposition, the sample was cooled in the deposition atmosphere at a cooling rate of 12 °C·min⁻¹. A cross-section of the WE of an as-prepared sample is shown in Fig. 5.3.

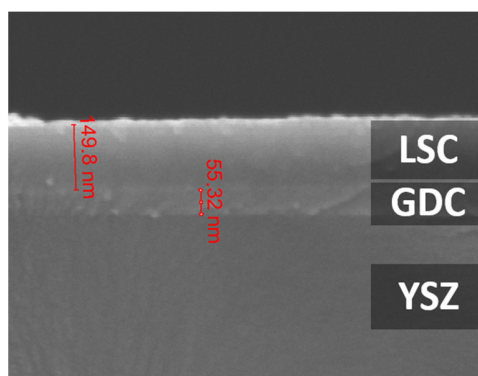


Fig. 5.3 SEM image of sample cross-section showing the 150 nm thin LSC film on top of the 55 nm thin GDC film grown on a YSZ single crystal.

The substrate was flipped and a porous LSC counter electrode was prepared by PLD in $4 \cdot 10^{-1}$ mbar oxygen partial pressure, at 450 °C substrate surface temperature, using 9,000 laser pulses and an adapted substrate to target distance of 5 cm. The morphological structure of such counter electrodes was analyzed by TEM cross-sections, and details on the electrochemical performance measured by impedance spectroscopy are given in chapter 2.3.3 and 2.3.4.

5.2.3 Electrochemical characterization - IPLD

The in-situ Impedance PLD (IPLD) setup is shown in Fig. 5.1. The surface of the resistive heater is arranged in the lab floor planes and a corundum plate is placed on top of the uncovered Pt heating wires for electronic isolation. Next, a Pt sheet placed on top of the corundum plate is pinned down by a corundum ring (Fig. 5.1b); it is used to contact the CE for the impedance measurement. A Pt wire wrapped around the entire length of a movable Cu arm was grinded to a sharp ($\sim 10 \mu\text{m}$) tip at one end. It is fixed in an in-plane distance of 18 cm directly at a chamber feedthrough. Before putting a sample into the IPLD setup, targets were freshly grinded, inserted into the PLD and ablated for 1 min in $5 \cdot 10^{-1}$ mbar $p\text{O}_2$ at room temperature. Then, the PLD chamber was again opened and the sample was positioned on the Pt-sheet directly below the target in a distance of 4.7 cm and the WE was contacted by manually placing the Pt tip of the Cu arm in the middle of the sample (see Fig. 5.1b). Subsequently, the chamber was evacuated and the atmosphere set to $5 \cdot 10^{-1}$ mbar $p\text{O}_2$ before heating the sample to 450 °C. The temperature was controlled by measuring the ionic conductivity of the YSZ single crystal, see SI. Fig. 5.1a and 5.1c shows a photograph and a sketch of the entire system while applying one laser pulse on to a target. The surface area of the WE shadowed by the needle tip during material deposition amounts to 3-5 %. This was estimated from microscope images (color contrast) after growing a complete LSC electrode ($\sim 150 \text{ nm}$) on top of YSZ. The laser repetition rate was set to 1 Hz for depositions using 1, 2, 5, 10, 20 and 50 laser pulses and increased to 2 Hz for ablations with 100, 200 or 500 laser pulses.

The impedance was measured by a Novocontrol Alpha A High Performance Frequency Analyzer in the frequency range from 10^6 to a minimum of 10^{-2} Hz with a resolution of five points per decade and an alternating voltage of 10 mV (rms) applied between the two thin film electrodes. The serial 2-point Pt wire resistance ($2 - 3 \Omega$ at 450 °C) was separately measured by placing the tip of the WE contact directly on the Pt-sheet. For each sample situation three spectra were measured

subsequently and those were generally in close agreement. This guarantees that resistance changes larger than 5 – 10 %, found after surface decoration, are true effects and not caused by a parallel degradation process. Furthermore, continuous impedance measurements inside the PLD chamber for 6 hours did not show any indication of electrode degradation and the scatter of the surface exchange resistance of 4 % was primarily because of temperature fluctuations (452 ± 3 °C), see chapter 5.5.3.

5.2.4 Chemical characterization – ICP and XPS

For the determination, of the target deposition rates, 100, 500 and 1000 laser pulses were used to ablate “La”, “Sr”, “Sr (sc)” and “Co” on to the surface of three YSZ single crystals, respectively, in a single run. The deposited materials were then dissolved in a 0.5 ml mixture of conc. HCl, HNO₃ and H₂O₂ for over 16 hours. Afterwards, ~14.5 ml of ultrapure H₂O and 15 µl of 10 ppb In (Indium Standard solution, Aristar®) as internal standard were added to the clear solutions of dissolved cations. For quantification, a standard dilution series was prepared using a mixture of La (ICP-Multi-Element Standard, Aristar®), Co and Sr (both Plasma Emission Standard, Prolabor®) in a similar acidic matrix. Cation amounts and calibration curves were determined by ICP-MS (iCAP™ Q, ThermoFisherScientific, Germany).

For X-ray photoelectron spectroscopy (XPS), samples were heated up to ~360 °C for 5 minutes in air to reduce the atmospheric carbon contamination prior to mounting. XPS measurements were carried out on a spectrometer with monochromatic Al K_α source (Microfocus 350, SPECS Surface Nano Analysis, Germany) and an angle-resolved photoelectron Analyser (Phoibos WAL, SPECS), collecting photoelectrons in the range of 20 to 80 degree from the surface normal. The microstructure of the as-deposited and decorated LSC thin films was investigated by a FEI Quanta200 field emission gun scanning electron microscope equipped with an Everhart–Thornley detector at 5 kV accelerating voltage.

5.3 Results

The $\text{La}_{0.6}\text{Sr}_{0.4}\text{CoO}_{3-6}$ thin film (140 nm) working electrode under investigation was deposited on an yttria stabilized zirconia (YSZ) single crystal with 50 nm Gd doped ceria (GDC) buffer layer. A porous LSC thin film acted as low resistance counter electrode and this sample was placed on a Pt sheet in the PLD chamber. Contact to an impedance analyzer was established by a Pt wire on top, see Fig. 5.1, thus leaving the LSC surface free for PLD deposition of additional oxides at 450°C in 0.5 mbar O_2 . The working electrode surface was modified (“decorated”) by applying a very limited number of laser pulses (between 1 and 888) to polycrystalline SrO (“Sr”), Co_3O_4 (“Co”), La_2O_3 (“La”) and single crystalline SrO (“Sr (sc)”) targets. Impedance spectra were recorded on as-prepared samples and after applying increasing numbers of PLD pulses for surface decoration. Representative Nyquist plots obtained at 450°C after decoration by different cation amounts are shown in Fig. 5.4 (“Sr” and “Co”) and in Fig. 5.10 (“La” and “Sr (sc)”).

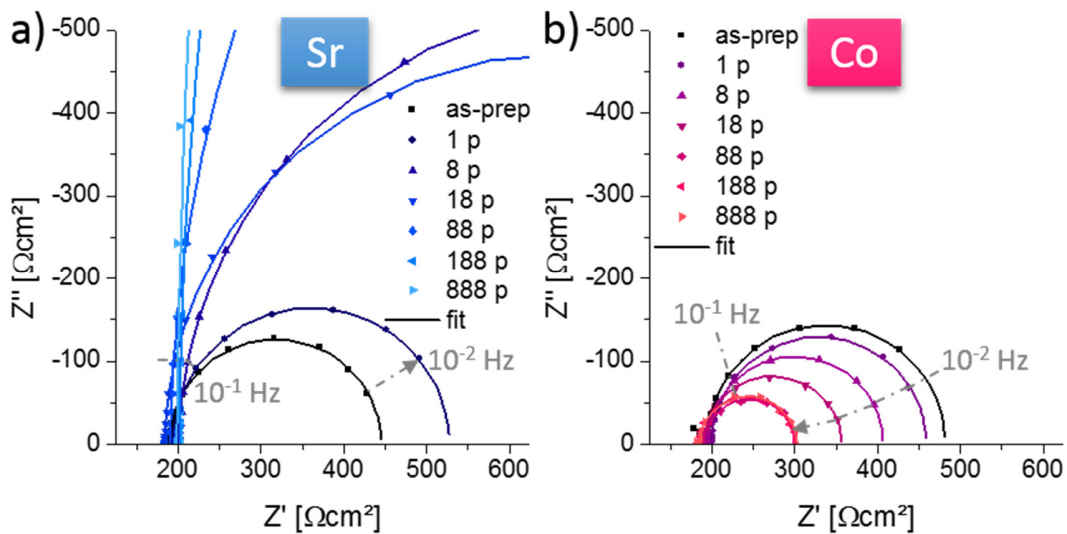


Fig. 5.4 Representative Nyquist plots normalized to the surface area of the LSC working electrode of as-prepared thin films decorated with particles from (a) “Sr” and (b) “Co” target measured in-situ at 450°C and $5 \cdot 10^{-1}$ mbar $p\text{O}_2$. The legends specify the total number of laser pulses after which the impedance spectra were recorded.

The interpretation of the spectra is based on many previous studies on LSC and similar mixed conducting electrodes^{65, 120} and is detailed in chapter 5.5.1. The main arc of the spectra, visible between ca. 100 – 0.01 Hz, is caused by the resistance of the oxygen exchange reaction at the working electrode surface. A significant effect of the counter electrode is not present, chapter 5.5.2. The parallel capacitor reflects the bulk chemical capacitance of the LSC film, which remained

constant at $1243 \pm 64 \text{ F/cm}^3$ throughout the study, irrespective of any surface modification. This is not surprising, since the surface of the 140 nm thick LSC film was only decorated by small amounts of oxides with a much lower non-stoichiometry.

Both as-prepared samples in Fig. 5.4 show a similar oxygen surface exchange resistance ($R_{\text{surf exch}}$) of ca. $250 \text{ } \Omega\text{cm}^2$ at 450°C in $0.5 \text{ mbar } p\text{O}_2$. Decoration of the LSC surface by depositing Sr or Co strongly affects the oxygen reduction reaction (ORR) already after a few laser pulses. Even a single pulse increases (Sr) or decreases (Co) $R_{\text{surf exch}}$. These partly small changes in the electrochemical response can only be monitored by an in-situ strategy, which ensures that the surface is not altered between preparation and measurement. $R_{\text{surf exch}}$ continuously increases for “Sr” decoration, while it significantly decreases for “Co”. In the latter case, however, changes level off after a few ten laser pulses at about 30% of its original resistance values.

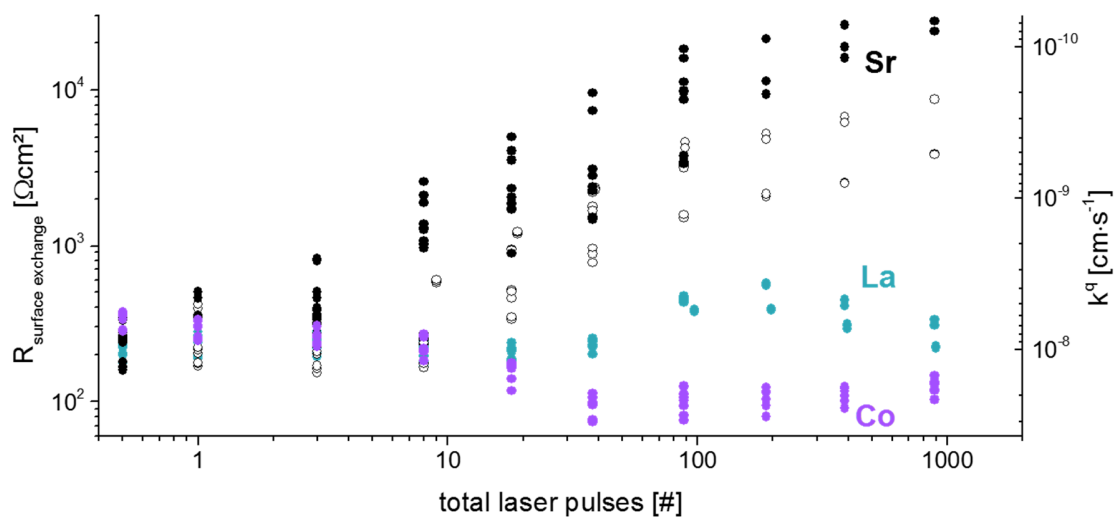


Fig. 5.5 Dependence of the surface exchange resistance and surface exchange coefficient k^a on the number of laser pulses used to decorate the LSC WE surface of 16 samples at 450°C in $5 \cdot 10^{-1} \text{ mbar } p\text{O}_2$; the surface exchange coefficient is given by¹²¹ $k^a = R_g T / (4F^2 R_{\text{surf exch}} c_O)$ with R_g being the gas constant, T the absolute temperature, F Faraday’s constant, $R_{\text{surf exch}}$ the ORR resistance normalized to the electrode area and c_O the oxygen lattice site concentration in LSC.

The same type of experiment was performed on 16 samples using four different targets for decoration. Fig. 5.5 displays the surface exchange resistance of all measurements on a logarithmic scale. The surface exchange resistance determined from the as-prepared samples ($254 \pm 77 \text{ } \Omega\text{cm}^2$) exhibits some scatter but relative changes of each sample and also the absolute values of the complete data set reveal very clear trends. The catalytic activity for the ORR of “Co” modified LSC surfaces were reproducibly increased by almost a factor of 3 after 38 pulses, corresponding to 96

$\pm 17 \Omega\text{cm}^2$, but then did not further change much. Decoration with “Sr”, on the other hand, leads to a strong and continuous decrease of the ORR activity with ongoing deposition: $R_{\text{surf,exch}}$ increased by almost a factor of 100 after 888 pulses on to the polycrystalline Sr target. Sr deposited by pulses on the single crystalline target (sc) seems to be less detrimental, but differences between “Sr” and “Sr (sc)” can be largely attributed to different deposition rates, see below. Deposition of “La” shows at first no influence on the ORR activity but after 88 pulses an increase of the surface exchange resistance is observed which, however, again decreases to nearly its initial values after 888 laser pulses.

The fact that very few pulses of Sr or Co may lead to severe changes of $R_{\text{surf,exch}}$ already suggests that rather small amounts of decorating ions strongly affect the oxygen exchange kinetics (cf. 6750 pulses required to deposit the entire LSC working electrode). However, for a more quantitative discussion, knowledge on the amounts of decorating ions is essential. This was determined by another independent measurement series. There, 100, 500 and 1000 laser pulses were used to ablate the respective target materials on top of inert YSZ single crystals under the same PLD conditions. The deposited oxides were then completely dissolved in a mixture of conc. HNO_3 , H_2O_2 , HCl , the amount of cations quantified by inductively coupled plasma mass-spectrometry (ICP-MS) and calibration curves were calculated (Fig. 5.6).

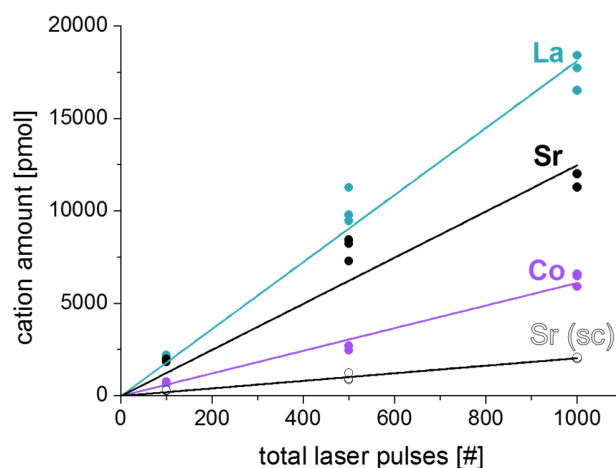


Fig. 5.6 Cation amount detected by ICP-MS plotted versus the total number of laser pulses used to fabricate the calibration samples. The slope of each curve represents the deposition rate of the respective targets: $6.3 \pm 0.2 \text{ pmol Co}$, $18.5 \pm 0.5 \text{ pmol La}$, $2.3 \pm 0.1 \text{ pmol Sr (sc)}$, $12.7 \pm 0.7 \text{ pmol Sr per laser pulse}$.

Hence, the deposition rates of target materials became available (6.3 pmol Co, 18.5 pmol La, 2.3 pmol Sr (sc), 12.7 pmol Sr per laser pulse). This allows us to plot the oxygen surface exchange resistance versus the amount of cations deposited on top of the LSC working electrode. From this quantitative analysis it is also possible to estimate the number of pulses required to deposit the cation amount for a (100) perovskite monolayer, $1.7 \cdot 10^{14}$ cations or 283 pmol. In this estimate, the same chemical composition of deposited particles and target materials and homogenous layer-by-layer growth is assumed (see chapter 5.2.1). One may argue that the material ablated from the target by one pulse can lead to somewhat different cation amounts on different substrates, i.e. on YSZ (used for amount quantification) and LSC (used for impedance analysis). However, since the numbers of our laser pulses cover three orders of magnitude, any moderate error does not affect the entire discussion. Moreover, studies on other oxides revealed that the substrate dependence of the deposition rate is more in the 5 – 15 % range¹²².

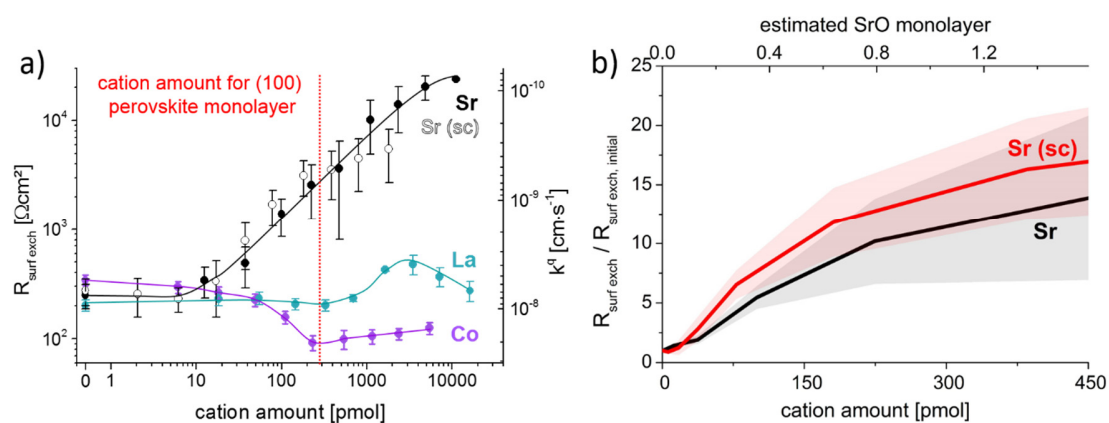


Fig. 5.7 (a) Surface exchange resistance plotted versus the amounts of cations deposited on the LSC WE surface (log – log plot, lines are guides to the eye). The nominal amount of cations needed to form a (100) perovskite monolayer is indicated as well. (b) Increase of the surface exchange resistance relative to its initial value with ongoing deposition of “Sr” and “Sr (sc)”. Effects of “Sr” and “Sr (sc)” decoration are the same within the error bars (colored area).

Fig. 5.7 displays the same resistance data as Fig. 5.5 but plotted versus the calculated amount of decorating cations. The amount nominally needed to establish a (100) perovskite monolayer is indicated by a vertical line. For all target materials, surface modifications by just a few laser pulses correspond to much less than a monolayer of the respective materials. A single laser pulse of “Sr” equals to $\sim 4\%$ of a SrO monolayer (~ 13 pmol Sr) but still this increases the initial $R_{\text{surf exch}}$ by about $42 \pm 6\%$. Three pulses ($\sim 13\%$ of a SrO monolayer) almost double $R_{\text{surf exch}}$. This severe detrimental effect of SrO cannot simply arise from a homogenous passivation of the electrode surface. Rather,

deposited SrO has to diffuse to highly active sites of an inhomogeneously active electrode surface. With ongoing deposition of SrO a further increase of $R_{\text{surf exch}}$ by a factor of about 6 and 11 for a nominal coverage of only 23% and 53% of the LSC working electrode area, respectively, is found. In Fig. 5.7 the relative resistance increase is plotted versus the Sr cation amount for Sr and Sr (sc) targets. The curves do not differ within the given error, which shows that the difference observed between the data obtained for the two Sr targets in Fig. 5.5 can be attributed to the different deposition rates.

Several studies on LSC thin films dense bulk pellets and porous electrodes^{31, 32, 37, 38, 55, 119, 120} reported an increase of the oxygen exchange resistance with annealing time and associated this with Sr surface segregation, measured ex-situ on degraded samples^{31, 32, 37, 38, 119}. These observations are in agreement with the deteriorating effect of SrO found in our decoration experiments. However, it was not known so far that already very small amounts of SrO can already significantly poison the electrode. Hence, our new method of in-situ IS during surface modification proves to be very powerful in revealing novel insights. With this information on large effects by little Sr in mind, it is also no longer surprising that the data reported on the ORR activity of LSC scatter by orders of magnitudes; already small variations of annealing temperature and atmosphere or solvents used during preparation steps can alter the surface and thus affect the oxygen exchange kinetics. Further, such small surface stoichiometry changes may explain degradation phenomena of the electrochemical kinetics found despite absence of measurable changes of the cation surface stoichiometry, see chapter 4.3.3 Interestingly, the negative impact of the “Sr” deposition can be observed even after 388 laser pulses, which already corresponds to 3.3 nm of a nominally dense SrO film. This suggests that the still existing oxygen exchange is facilitated through SrO particles/layers although at a much lower rate than by the active sites present in the beginning.

Decoration with 1 pulse of Co-oxide nominally corresponds to ~2 % of a monolayer and already enhances the oxygen exchange kinetics of the LSC base film by about 13 %. More pulses lead to further improvement but the decrease of the resistance $R_{\text{surf exch}}$ stops after reaching a factor of 3 for about one Co_3O_4 monolayer. However, it should be noted that “Co” and “La” decorations most probably form islands on top of the electrode and do not show a layer-by-layer growth, see chapter 5.5.5.

The positive effect of Co was further investigated on LSC films already decorated with Sr or La and thus exhibiting higher $R_{\text{surf exch}}$ compared to as-prepared thin films. 10, 20 and 50 laser pulses were

applied to the “Co” target and thus up to 550 pmol Co (~ 1.9 monolayers of Co_3O_4) was deposited on samples first degraded by 88 pulses of “Sr” (4.0 monolayer SrO), “Sr (sc)” (0.7 monolayer SrO), and “La” (5.8 monolayers La_2O_3).

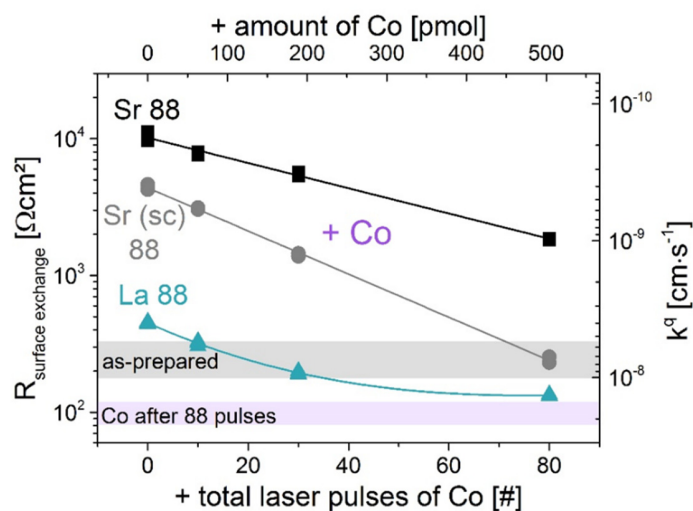


Fig. 5.8 Decrease of the surface exchange resistance while samples already decorated with 88 laser pulses of the “Sr”, “Sr (sc)” and “La” target were further decorated with 10, 20 and 50 laser pulses of the “Co” target at 450°C in $5 \cdot 10^{-1}$ mbar $p\text{O}_2$

For all samples a drastic enhancement of the oxygen exchange kinetics by Co was found, see Fig. 5.8. A total of 80 pulses of “Co” was sufficient to reduce the surface exchange resistance by a factor of 5.7, 18.3 and 3.4 for the samples decorated with 88 pulses of “Sr”, “Sr (sc)” and “La”, respectively. The much stronger relative and absolute effect of the “Co” decoration on the “Sr (sc)” sample compared to the “Sr” sample is most probably related to the lower deposition rate of the “Sr (sc)” target. For the “Sr” sample already 4.0 monolayer SrO were present and Co could not improve the electrode to the same degree as for “Sr (sc)” with only 0.7 monolayers SrO present. These and the results shown in Fig. 5.7a give clear experimental evidence that the accessibility of Co at the surface strongly improves the oxygen exchange kinetics. This conclusion is also in agreement with results presented in chapter 4.3.5, where an increase of the ORR activity by a factor of 2 was achieved after removing the Sr-termination layer of as-deposited LSC thin films and thus exposing more Co ions to the gas phase. Further, a higher Co surface concentration in $(\text{La}_{0.75}\text{Sr}_{0.25})_2\text{CoO}_{4\pm\delta}$ compared to $(\text{La}_{0.5}\text{Sr}_{0.5})_2\text{CoO}_{4\pm\delta}$ thin films was found and assumed responsible for the enhanced ORR kinetics¹²³. However, the environment of the Co-oxide particles still plays an important role for the catalytic activity.

The following mechanistic discussion starts with a conclusion already drawn above from our novel results particularly from the fact that small amounts of Sr cause severe resistance increases: Only relatively few sites of as-prepared films are highly active for oxygen exchange, and the decorating Sr cations do not randomly cover the surface but specifically deactivate these active sites. Our model of the relation between the ORR and the cation surface stoichiometry is sketched in Fig. 5.9.

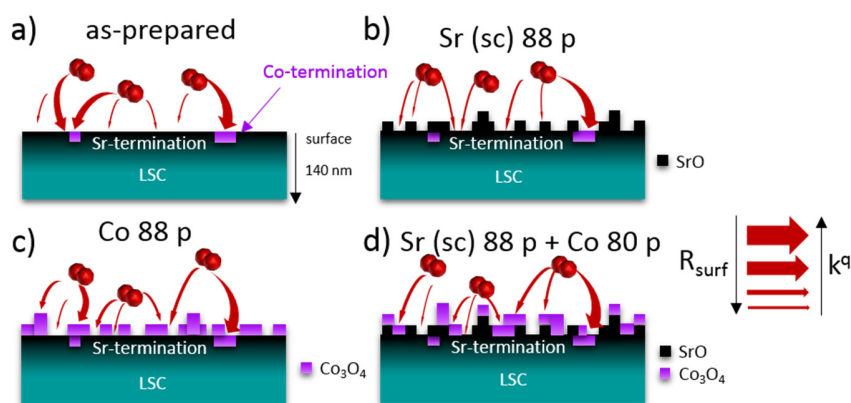


Fig. 5.9 Sketch of the model of inhomogeneously active LSC surfaces. (a) Sites of as-prepared thin films with Co-termination show a higher exchange rate than regions with Sr-termination. (b) Co-oxide decoration leads to an increase of the ORR activity. (c) SrO causes an activity decrease (resistance increase). (d) The surface of a SrO decorated LSC electrode can be reactivated to its initial value by adding Co-oxides, provided the SrO layer was not too thick yet.

A recent study showed that as-prepared LSC films as used here exhibit a kind of SrO termination (ca. one monolayer) even though in the surface layer still some La (10 %) and Co (9 %) cations are present, see chapter 4.3.2. This result suggests that those remaining Co sites (“Co termination” in Fig. 5.9a) are responsible for most of the oxygen exchange activity of as-prepared LSC films and that those enable the rather low surface polarization resistance of LSC. By chemically removing the terminating SrO layer the oxygen surface exchange resistance can be further lowered, in agreement with an enhanced Co concentration (27 %), see chapter 4.3.5. The SrO terminated part of the film, however, is also not completely inactive, it only exhibits a much reduced oxygen exchange rate, see Fig 5.9a. When depositing SrO, Sr surface diffusion to Co-terminating sites takes place and almost none of these sites remains available after some Sr decoration, see Fig. 5.9b. Possibly, the “Co termination” sites are primarily located at extended surface defects such as edges and Sr “aggregation” is not surprising.

After deactivating all Co sites, only the much slower oxygen exchange via SrO terminated regions remains possible. Deposition of additional SrO then “only” increases the thickness of the SrO layer and this further enhances the polarization resistance. The exact reason of this continuous further increase of the resistance remains speculative. Either the rate limiting step is still a surface related oxygen dissociation/ionization step and electron transfer becomes more difficult for larger distances to “buried” Co sites, or ion transport through the SrO layer plays a role. These suggested two ways of how Sr may affect the oxygen exchange kinetics are also in agreement with a change in the slope of the linear polarization resistance versus Sr amount plot (Fig. 5.8b): small Sr amounts deactivate highly active sites, larger amounts thicken the SrO layer. This would require electronic and ionic conductivity of thin SrO layers, which was also recently proposed by Mogensen et al.¹²⁴ based on similar considerations.

The effect of Co decoration on an as-prepared LSC layer is similar to the effect of a removal of SrO by chemical etching (chapter 4.3.4): In both cases more Co becomes available at the surface and thus the number of sites with fast oxygen exchange increases, see Fig. 5.9c. The positive effect of Co might be limited by island formation but also by the fact that oxygen vacancies are required for oxygen reduction and those may be associated with Sr. Additional Co on LSC with already existing Sr decoration can still strongly improve the oxygen exchange even though the underlying Sr hinders highest electrocatalytic activity, see Fig. 5.9d. The more Sr was deposited before Co, the higher the final resistance remains. Accordingly Co is most active close to the LSC bulk.

5.4 Conclusions

In summary, these experiments show that it is possible to manipulate electrode surfaces while in-situ measuring the ORR activity and thus one can avoid any alteration of the surface between preparation and investigation by undesired reactions with the ambient atmosphere or changes caused by cooling and heating. This technique also strongly improves the possibilities for monitoring effects of small amounts of cations and thus allowed us to achieve the main conclusions of this paper: small amounts (of cations) may matter a lot and the high electrochemical activity of LSC is most probably caused by only few highly active (Co-based) sites at the surface. Quantification of the surface modification was performed by means of calibration curves using inductively coupled plasma-mass spectrometry (ICP-MS). It was shown that a single laser pulse of "Sr" equals to ~4 % of a SrO monolayer (~13 pmol Sr) but still this increases the initial $R_{\text{surf exch}}$ by about 42 ± 6 %. Three pulses (~13% of a SrO monolayer) almost doubled $R_{\text{surf exch}}$. Therefore it is concluded that only a few sites of as-prepared LSC films are highly active for oxygen exchange and that decorating Sr cations do not randomly cover the surface but specifically deactivate those active sites. Moreover, Co-oxide decoration improved the ORR kinetics even of vastly degraded samples and gave clear evidence that the accessibility of Co at the surface for oxygen strongly improves the ORR kinetics. The novel combination of PLD and IS may not only be applicable to many other electrode surfaces but can also be highly valuable for directly monitoring the electrochemical properties of a growing MIEC thin film even at its earliest stages. Hence, insights into the film thickness dependence of defect chemistry and ORR activity can be gained at an accuracy level not accessible otherwise.

5.5 Appendix

5.5.1 Decoration with “La” and “Sr (sc)” and detailed impedance interpretation

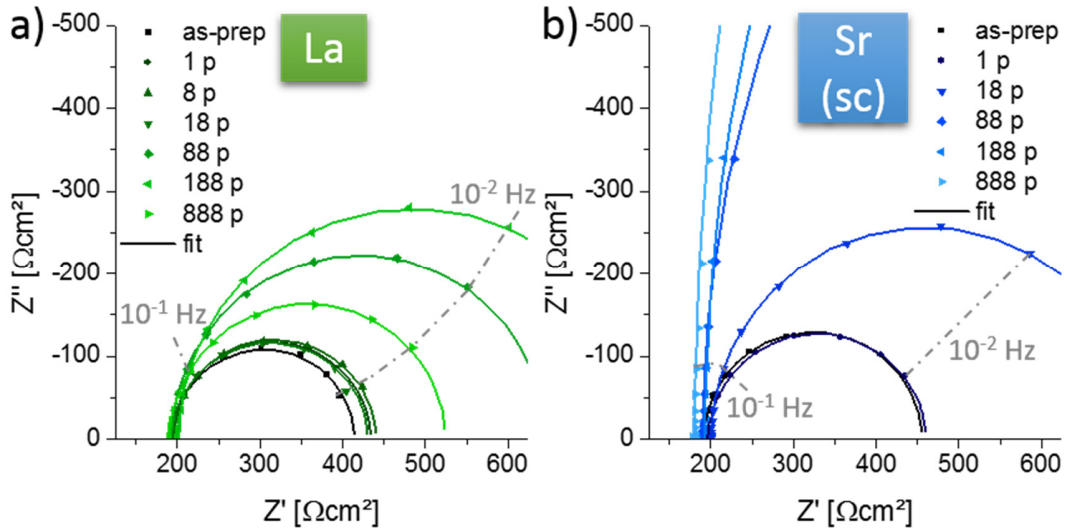


Fig. 5.10 Representative Nyquist plots normalized to the surface area of the working electrode for as-prepared thin films decorated with particles from (a) “La” and (b) “Sr (sc)” target measured in situ at 450 °C and $5 \cdot 10^{-1}$ mbar $p\text{O}_2$. The legends specify the total number of laser pulses after which the impedance spectra were recorded.

The high frequency intercept of impedance spectra (>100 Hz, $\sim 175 - 200 \Omega\text{cm}^2$), see Fig. 5.4 and 5.10, is predominantly attributed to the oxide ion conduction in the YSZ single crystal electrolyte. Resistive contributions from wiring ($\approx 3 \Omega$) could be neglected and the electronic sheet resistance was sufficiently small to guarantee a homogenous polarization of the entire working electrode (WE) despite very local contact by a needle tip (see below). The known temperature dependent ionic conductivity of YSZ⁶⁴ was used to determine the temperature from this high frequency intercept and to adjust the temperature to 450 °C throughout the entire study. Variations of the high frequency intercept between the different impedance spectra thus reflect small temperature fluctuations ($\pm 3 \text{ }^\circ\text{C}$). At lower frequencies (100 – 0.01 Hz) the impedance spectra become semicircle like and can be fitted to a resistor in parallel with a constant phase element (exponential fitting parameter $n > 0.98$). The resistance is associated with the oxygen surface exchange reaction of the LSC top electrode ($\sim 250 \Omega\text{cm}^2$); the ion transport resistance in the LSC electrode can be neglected under these and similar conditions, see chapter 6. The capacitive element in parallel to $R_{\text{surf, exch}}$ has a size of $> 20 \text{ mF/cm}^2$ and corresponds to the chemical capacitance of the LSC WE cf. interpretation in Ref. ¹²⁰. The chemical capacitance describes the ability of the material to store

chemical energy by undergoing stoichiometric changes and is therefore actually a volume property. It should be emphasized that the highly active porous counter electrode (CE) does not noticeably contribute to the impedance spectra. Even for the lowest electrode impedance ($96 \pm 17 \text{ } \Omega\text{cm}^2$, after Co decoration) no indication of a CE effect was found since the chemical capacitance of the low frequency semicircle remained unaffected by Co decorations. The maximal impedance of the CE was deduced by another IPLD measurement series (Chapter 5.5.2), where up to 188 laser pulses of porous LSC were deposited on top of the dense LSC WE and the surface exchange resistance thus decreased by more than an order of magnitude to $16 \text{ } \Omega\text{cm}^2$. This indicates that our much thicker porous CE has an even smaller polarization resistance.

The electronic sheet resistance $R_{\text{eon, sheet}}$ of the dense LSC thin film WE was estimated by

$$R_{\text{eon, sheet}} = \frac{1}{\sigma} \int_{\varnothing \text{ needle tip}}^{\varnothing \text{ sample}} \frac{dr}{2\pi r d} = \frac{1}{\sigma} \cdot \frac{1}{2\pi t} \cdot \ln r \Big|_5^5 \text{ mm} \quad (5.1)$$

with an LSC film thickness d of $\sim 140 \text{ nm}$, a needle tip diameter of $\sim 5 \text{ } \mu\text{m}$ (used to contact the WE), a sample size ($5 \times 5 \text{ mm}$) of $\sim 5 \text{ mm}$ diameter and an electronic conductivity σ of 1015 S/cm , which was measured on similar LSC thin films at $450 \text{ }^\circ\text{C}$ by the Van der Pauw Method, see chapter 6.3.6. An electronic sheet resistance of $77 \text{ } \Omega$ is thus obtained. Since, $R_{\text{eon, sheet}}$ is more than one magnitude lower than the sum of the ionic transport resistance of YSZ at $450 \text{ }^\circ\text{C}$ ($750 \text{ } \Omega$) and the oxygen exchange resistance ($\sim 1000 \text{ } \Omega$), it can be concluded that the entire electrode is electrochemically active, i.e. polarized.

5.5.2 Decoration with porous LSC to estimate CE influence

In order to estimate the influence of the porous LSC counter electrode on the low frequency semicircle, porous LSC was continuously deposited on an as-prepared dense LSC top electrode at $450 \text{ }^\circ\text{C}$ in $5 \cdot 10^{-1} \text{ mbar pO}_2$. Three impedance spectra, each taking 10 minutes, were measured after the deposition of LSC using 1, 2, 5, 10, 20, 50 and 100 laser pulses at a repetition rate of 1 Hz. Representative Nyquist plots normalized to the electrode surface area are shown in Fig. 5.11a and the legend shows the total amount of laser pulses after which the impedance spectra were recorded.

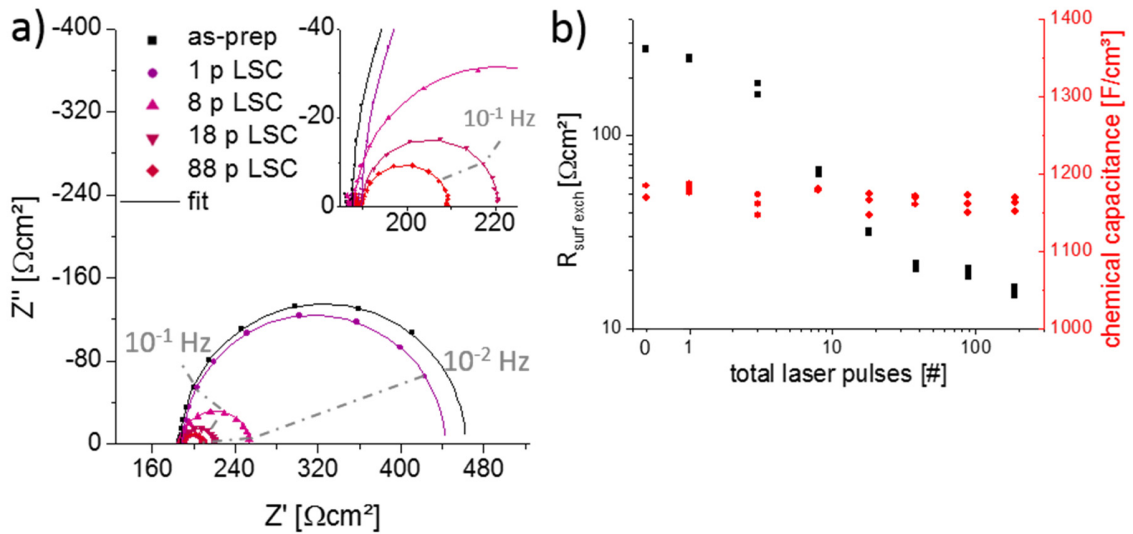


Fig. 5.11 (a) Representative Nyquist plots normalized to the surface area of the working electrode for as-prepared thin films decorated with particles from an LSC target and measured in situ at 450 °C and $5 \cdot 10^{-1}$ mbar $p\text{O}_2$. The legend specifies the total number of laser pulses after which the impedance spectra were recorded. (b) Decrease of the surface exchange resistance with increasing amount of laser pulses and independency of the chemical capacitance.

The high frequency intercept is not influenced by the LSC deposition and was again used to determine and adjust the temperature of the sample. Already after the deposition of 1 single laser pulse the diameter of the low frequency semicircle decreases measurably significantly. This means that the catalytic activity for oxygen surface exchange of the top electrode is enhanced by partly covering it with fresh LSC particles. This is in agreement with results presented in chapter 4, where it was shown that dense LSC electrodes deposited at higher temperature (600 °C) exhibit a Sr-rich termination layer after deposition, which decreases the catalytic activity, while low deposition temperatures lead to highly active surfaces⁶³. Deposition of additional LSC material on top of the dense electrode further decreases the surface exchange resistance, see also Fig. 5.11b. The impressive enhancement of the oxygen surface exchange activity, however, is not solely caused by a chemical improvement of the surface but also by enlarging the participating electrode surface area, since under these deposition conditions porous LSC is grown on top of dense LSC. The chemical capacitance remains constant during the entire experiment, despite an increase of the electrode volume by 2-3 % by the end of the experiment. However, such a small increase might easily be missed due to data scattering. Since neither the shape of the impedance spectra nor the chemical capacitance showed any significant change after deposition of 188 laser pulses it can be safely assumed that the counter electrode does not contribute to the low frequency semicircle

and shows superior oxygen exchange kinetics under the given conditions. This conclusion is further supported by the fact that 188 laser pulses were already enough to improve the surface exchange resistance of the top electrode from 276 to $16 \text{ } \Omega\text{cm}^2$, while for the fabrication of the counter electrode 9000 laser pulses were used leading to a porous electrode with much larger area.

5.5.3 Stability of the LSC electrochemical performance

The temperature of a sample calculated from the high frequency intercept (ionic transport resistance of YSZ) varied around $452 \pm 3 \text{ } ^\circ\text{C}$ during 6 hours of annealing inside the PLD chamber, see Fig. 5.12. The surface exchange resistance followed the temperature fluctuations and did not show any indication of degradation. It was concluded that the LSC WE is stable in the setup under these conditions and excellently suitable for the performed study.

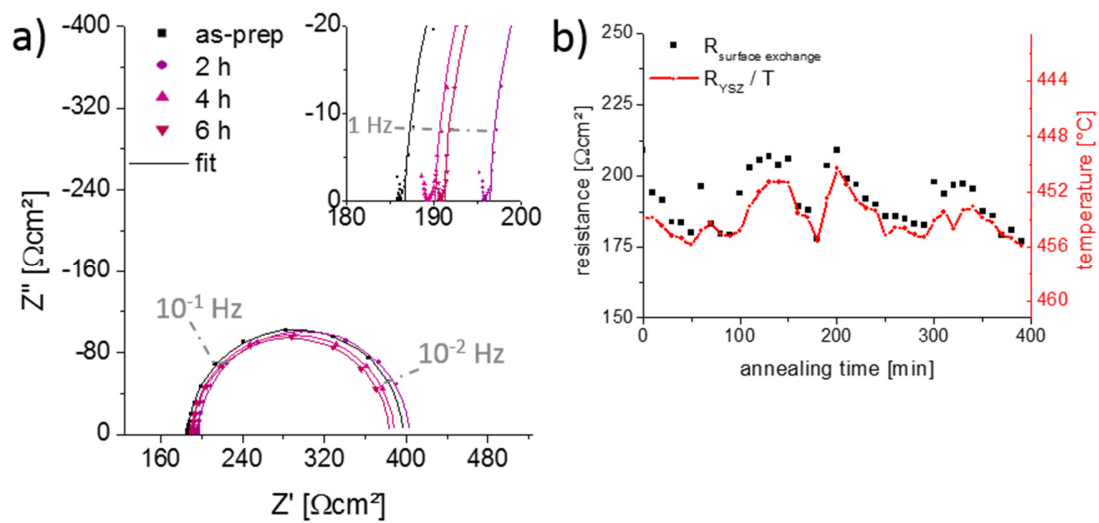


Fig. 5.12 (a) Representative Nyquist plots normalized to the surface area of the working electrode for as-prepared thin films annealed for 6 h at $450 \text{ } ^\circ\text{C}$ in $5 \cdot 10^{-1} \text{ mbar } p\text{O}_2$ and measured during annealing. The legend specifies the times after which the impedance spectra were recorded. (b) Progression of the relevant resistances with annealing time.

5.5.4 LSC compositions measured by XPS before and after decoration

XPS measurements were carried out after applying 88 or 888 laser pulses on different targets and decorating the surface of the LSC working electrode, Fig. 5.13. Approximately 68 % of the information is derived from the first 1.5 nm. The observed A-site and Sr enrichment for as prepared LSC thin films is in accordance with results obtained by XPS for similarly prepared LSC thin films in Ref. ³². Low Energy Ion Scattering (LEIS) measurements also confirmed a Sr termination (81 %) and a Sr enrichment for the first 3 nm of as-prepared LSC thin films, chapter 4.3.2. Deposition of “La” and “Sr” lead to the strongest change because of the much higher deposition rates. Clear trends between non, 88 and 888 applied laser pulses can be seen for all cation decorations.

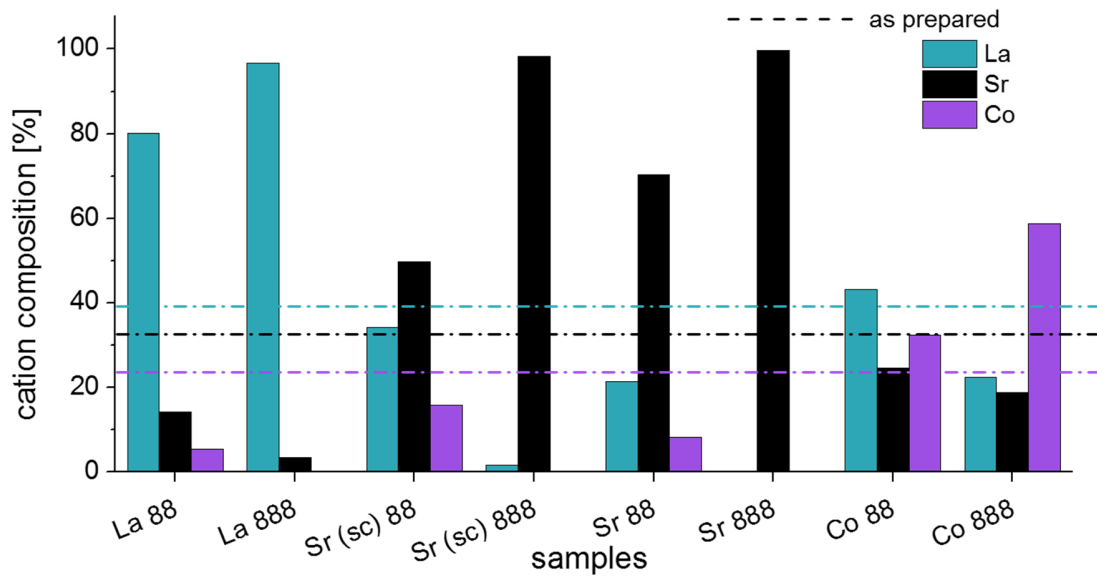


Fig. 5.13 XPS results of the cation composition, determined from Sr3d, La4d, and Co3p peak areas, for an as prepared sample (dotted line) and samples after deposition of 88 and 888 laser pulses of each target (“La”, “Sr (sc)”, “Sr”, “Co”).

5.5.5 LSC surface imaged by FESEM before and after decoration

SEM images obtained after 88 pulses (Fig. 5.14) and especially after 888 pulses (Fig. 5.15) suggest that “Sr” and “Sr (sc)” decorations form a rather dense layer on top of the 50 – 70 nm wide columnar grains of the as-deposited LSC thin film. On the other hand, for “Co” and “La” surface modifications small grains/islands seem to be distributed over the entire surface of the original LSC grain microstructure. It was shown in an earlier study that LSC films prepared by our procedure at >550 °C are already terminated by a monolayer of SrO, see chapter 4.3.2. It is very likely that the primarily Sr-terminated surface of LSC is very well wetted by material deposited from the “Sr” or “Sr (sc)” target, e.g. SrO on top of a SrO/SrOH/SrCO₃ termination. “La” island may thus form because of stronger adatom-adatom than adatom-LSC interactions and could leave SrO terminated “as prepared” LSC surface exposed to the gas. This remaining free surface becomes then improved by “Co” as seen in Fig. 5.9. Please note that Co-oxide island formation was only found in SEM after depositing an amount that corresponds to ~7 monolayers.

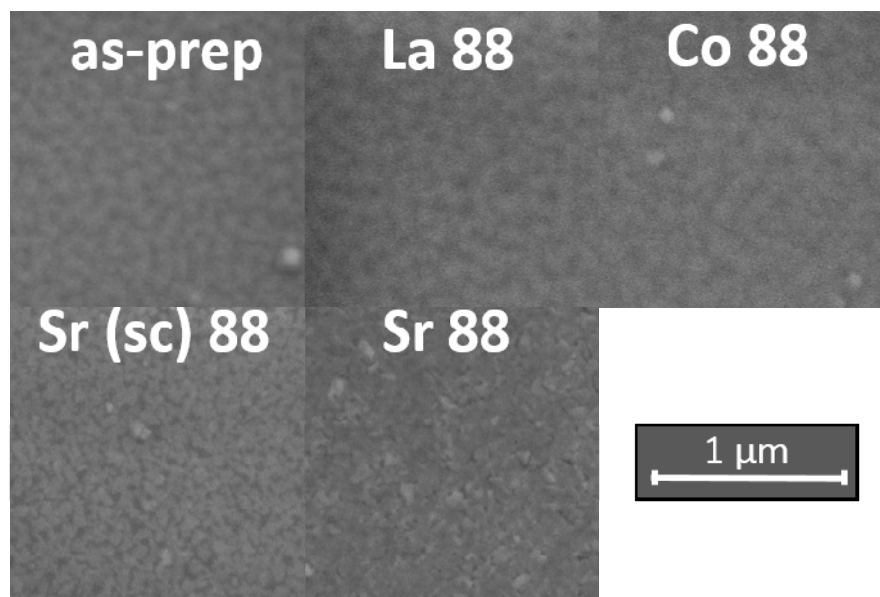


Fig. 5.14 SEM images showing the surface of as-prepared LSC WE before and after deposition of different target materials using 88 laser pulses. The microstructure of the as-prepared thin film (columnar LSC grains with a 50 – 70 nm ϕ) is still visible after the deposition of “La”, “Co” and even for “Sr (sc)”. For the “Sr” target the LSC surface is clearly covered by particles.

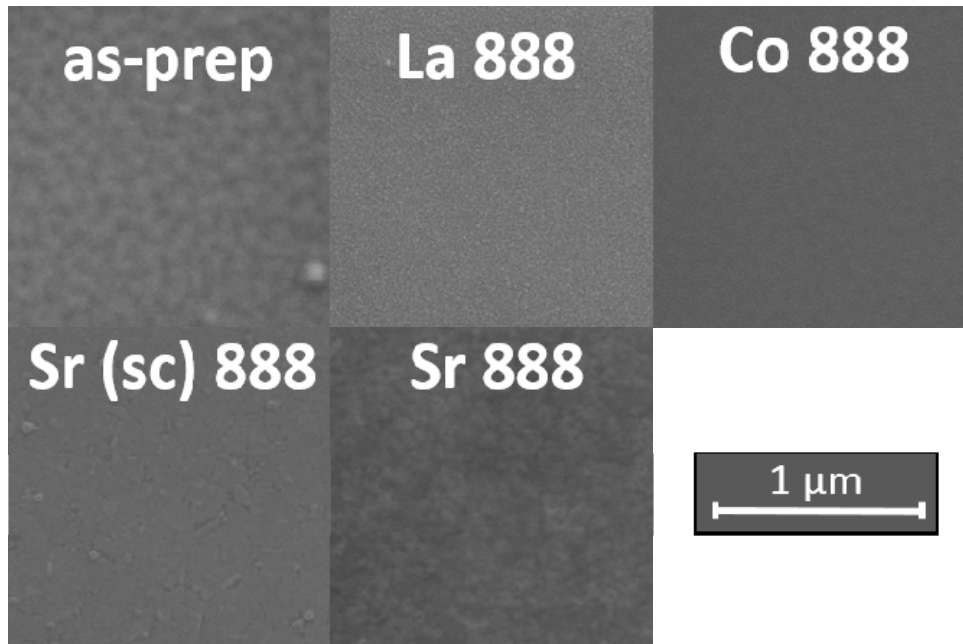


Fig. 5.15 SEM images showing the surface of as-prepared LSC WE before and after deposition of different target materials using 888 laser pulses. Shadows of the microstructure of the as-prepared thin film can still be found below the fine distributed islands of “Co” and “La” and particles. The surfaces of “Sr (sc)” and “Sr” decorated samples look almost molten and completely dense.

6 The superior properties of $\text{La}_{0.6}\text{Ba}_{0.4}\text{CoO}_{3-\delta}$ thin film electrodes for oxygen exchange in comparison to $\text{La}_{0.6}\text{Sr}_{0.4}\text{CoO}_{3-\delta}$

This chapter contains in large parts material published as a scientific paper in the Journal of The Electrochemical Society¹²⁰.

6.1 Introduction

It was already emphasized in chapter 1 that the ORR is considered to currently limit the performance of intermediate temperature (400 - 600 °C) SOFCs^{125, 126}. Special attention is therefore put on the search and improvement of cathode materials. $\text{La}_x\text{Sr}_{1-x}\text{MnO}_{3-\delta}$ (LSM) offers a high electronic conductivity, acceptable catalytic activity for the oxygen exchange and sufficient chemical stability, but due to its low ionic conductivity it is unattractive for SOFCs operating at intermediate temperatures. Mixed ionic and electronic conductors (MIECs) of the perovskite-type solid-solution $\text{La}_{1-x}\text{Sr}_x\text{Co}_{1-y}\text{Fe}_y\text{O}_{3-\delta}$ (LSCF), can extend the reaction zone from the triple phase boundary (electrode-electrolyte-gas) to the two phase boundary due to their excellent ionic conductivity. They also offer high catalytic activity for the oxygen exchange and thus have been in the focus of recent research^{65, 87}. For a given Sr concentration, e.g. $x = 0.4$, the catalytic activity, oxygen vacancy concentration and thus the ionic conductivity increase with the amount of Co on the B-site of the perovskite, though, at the expense of a reduced chemical stability¹²⁷. Furthermore, changes of the electronic structure are observed from semiconductor-like for $\text{La}_{0.6}\text{Sr}_{0.4}\text{FeO}_{3-\delta}$ (LSF) to metal-like behavior for $\text{La}_{0.6}\text{Sr}_{0.4}\text{CoO}_{3-\delta}$ (LSC) at SOFC operating conditions¹²⁸. The detailed influence of the B-site metal cation and of the Sr dopant concentration on the electrochemical properties were key aspects of numerous studies¹²⁹⁻¹³⁴, while much less investigations dealt with the effect of alternative A-site dopants¹³⁰.

In this chapter, the electrochemical properties of well-defined LSC64 and $\text{La}_{0.6}\text{Ba}_{0.4}\text{CoO}_{3-\delta}$ (LBC64) are directly compared with each other. The advantage of comparing these two identically charged dopants is that almost all the chemical and electrochemical differences originate from the different ionic radii of Sr^{2+} (144 pm) and Ba^{2+} (161 pm)¹³⁵, since both atomic Sr and Ba have a similar valence electron configuration ($5s^2$; $6s^2$). Nonetheless, the defect structure and thus the

MIEC properties differ significantly due to a higher reducibility of the perovskite-type lattice with Ba ions^{136, 137}. To the best of the authors' knowledge, electrochemical investigations of $\text{La}_{1-x}\text{Ba}_x\text{CoO}_{3-\delta}$ (LBC) electrodes have been only performed on porous systems¹³⁸⁻¹⁴² including mixtures of LBC with GDC¹⁴³. These studies already reported comparatively low polarization resistances, but were not able to deconvolute the surface exchange and transport resistances of LBC for geometrical reasons. Therefore, dense thin film model electrodes were used here and the catalytic activity for the oxygen exchange could be determined for LSC and LBC over an oxygen partial pressure range of 10^{-4} to 1 bar p_{O_2} and at temperatures between 450 and 600 °C. The results reveal the superior properties of LBC in terms of catalytic activity for oxygen exchange, in comparison to most state of the art MIECs for intermediate SOFCs.

6.2. Experimental

6.2.1 Thin film preparation

Targets for deposition of LSC thin films by pulsed laser deposition (PLD) were synthesized from powders prepared by Pechini synthesis⁶². La_2O_3 , SrCO_3 , BaCO_3 and Co powders (all Sigma Aldrich, 99.995 %) were individually dissolved in nitric acid, mixed in appropriate ratios and citric acid (TraceSELECT®, 99.9998 %) was added for chelation. A calcination step was performed at 1000 °C, followed by isostatical pressing (~150 MPa) of the powder to a pellet and a sintering procedure at 1200 °C for 12 hours in air, thus yielding a $\text{La}_{0.6}\text{Sr}_{0.4}\text{CoO}_{3-\delta}$ and a $\text{La}_{0.6}\text{Ba}_{0.4}\text{CoO}_{3-\delta}$ target for PLD.

The LSC and LBC thin films were deposited onto (100) oriented yttria stabilized zirconia (YSZ, 9.5 mol% Y_2O_3 , Crystec GmbH, Germany) single crystals with a thickness of 0.5 mm and a size of 5x5 mm² or 10x10 mm². Epipolished substrates were used to prepare symmetrical samples with nominally identical thin films on both sides of the YSZ for impedance measurements. Ablation of the target material was carried out by a KrF ($\lambda = 248$ nm) excimer laser (Lambda COMPexPro 201F) operated at a pulse repetition rate of 5 Hz, a pulse duration of 50 ns and a laser fluence of approximately 1.5 J·cm⁻² at the target. The atmosphere was set to $4 \cdot 10^{-2}$ mbar oxygen partial pressure and the substrate was heated to a surface temperature of 600 °C. By applying 9,150 laser pulses to the LSC and 8,175 laser pulses to the LBC target, thin films of approx. 300 nm thickness were grown on the substrate (substrate to target distance = 6 cm). After deposition, the sample was cooled in the deposition atmosphere at a cooling rate of 12 °C·min⁻¹. The substrate was flipped and the PLD procedure was again repeated for the backside. Prior to the impedance

measurements, the 5x5 mm² samples were broken into pieces of about 1.5x1.5 mm² to minimize the influence of electronic sheet resistance, see also chapter 6.3.2. It is noteworthy that the sample surface was never exposed to “cleaning” treatments after deposition in order to avoid any reactions and contamination from solvents including H₂O¹⁰⁰.

6.2.2 Structural characterization

The PLD target material was analyzed in Bragg Brentano geometry by a X'Pert Powder (PANalytical) diffractometer. A thin film diffraction pattern was obtained using a D8-Discover instrument (Bruker AXS) in parallel beam geometry equipped with a general area detector diffraction system (GADDS). Secondary electron microscopy was performed on a FEI Quanta 200 field emission gun scanning electron microscope equipped with an Everhart-Thornley detector.

6.2.3 Electrochemical measurements

All annealing and impedance experiments were performed in a cleaned quartz tube which was evacuated and refilled several times with the desired high purity N₂ (ALPHAGAZ™ 1 >99.999 mol% nitrogen)/O₂ (ALPHAGAZ™ 1 >99.998 mol% oxygen) mixture before the sample was uniformly heated in a tube furnace. The symmetrical samples (thin film – YSZ – thin film) were sandwiched between two platinum foils for impedance measurements. The electronic connection in the sample holder consisted of Pt wires and a non-encapsulated type S thermoelement was used for temperature measurement. No materials other than Pt, quartz and the sample itself were heated during impedance measurement and annealing. All these precautions were taken in order to obtain electrochemical measurements that do not suffer from any cathode poisoning. It took approximately 45 minutes to heat the sample to the desired temperature (thermal equilibration), then the different impedance measurement series were performed. The impedance was measured by a Novocontrol Alpha A High Performance Frequency Analyzer in the frequency range from 10⁶ to a minimum of 5·10⁻³ Hz with a resolution of five points per decade and an alternating voltage of 10 mV (rms) applied between the two thin film electrodes.

In-plane resistivity measurements of the thin films were also performed in a quartz tube. Four platinum needles were placed on top of the thin film in the corners of a 10 x 10 mm² sample as close as possible to the sample boundary to meet the prerequisites of the van der Pauw method¹⁴⁴.

The quartz apparatus was uniformly heated in a tube furnace and temperature was measured by means of an encapsulated type K thermoelement positioned adjacent to the sample. A mixture of high purity N_2/O_2 was used to realize an oxygen partial pressure of 0.21 bar. A precision voltage source (Keithley 2410) and a multimeter (Keithley 2000) were used during the course of the measurements.

6.3. Results

6.3.1 Structural characterization

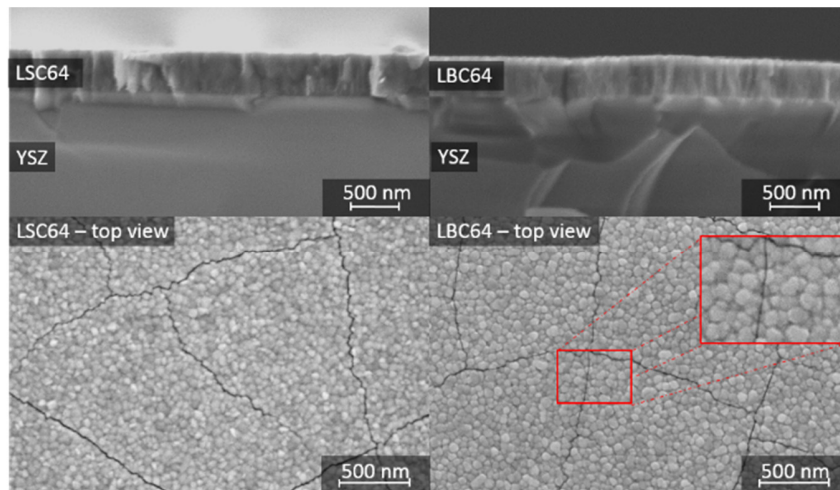


Fig. 6.1 SEM images of LSC (l.h.s.) and LBC (r.h.s.) thin films. Cross sections are shown on the top and the surface on the bottom.

The thin film morphology of both freshly deposited perovskite layers on top of the YSZ electrolyte was investigated by FESEM. Top views and cross-sections of the samples are shown in Fig. 6.1. Cross-sections of the thin films were achieved by fracturing of the samples. The electronically conducting thin films are clearly distinguishable from the blurry image of the non-conductive substrate. Therefore, the film thicknesses (LSC \approx 420 nm; LBC \approx 410 nm in Fig. 6.1) could be estimated from SEM-images and deposition parameters were then adjusted to obtain 300 ± 10 nm thin films for both materials. Both thin films show a very similar dense packing of columnar shaped grains, which is expected for the PLD growth conditions applied^{50, 60}. No voids or pinholes were observed in the cross-sections. For both materials crack formation could not be avoided, as seen in the top views in Fig. 6.1. Crack formation most probably takes place after completing thin film deposition during cooling and is driven by the difference of thermal expansion coefficients

between thin films ($\text{LSC64}^{107} = 20.5 \cdot 10^{-6} \text{ K}^{-1}$, $\text{LBC64}^{141} = 22.3 \cdot 10^{-6} \text{ K}^{-1}$) and substrate ($\text{YSZ}^{108} = 10.8 \cdot 10^{-6} \text{ K}^{-1}$). From previous measurements on similar LSC64 thin films an enhanced true surface area due to crack formation of up to 30 % was estimated see chapter 4.3.4. However, quantities extracted by EIS in this study were still normalized to the projected electrode surface area. Most cracks can be assumed to not penetrate the entire film, otherwise in-plane conductivities (see chapter 6.3.6) should be much smaller.

PLD target and thin film structure were examined in Bragg-Brentano 2θ - θ geometry with focusing and parallel-beam optics, respectively. LSC64 and LBC64 target as well as thin film diffraction patterns over the measured 2θ range are shown in Fig. 6.2. For both polycrystalline target diffraction patterns all visible peaks could be assigned to the perovskite phases and no sign of impurities was found. The peaks were indexed with respect to the pseudo-cubic structure of both materials since the rather small rhombohedral distortion of the crystal lattices could not be measured with the given resolution.

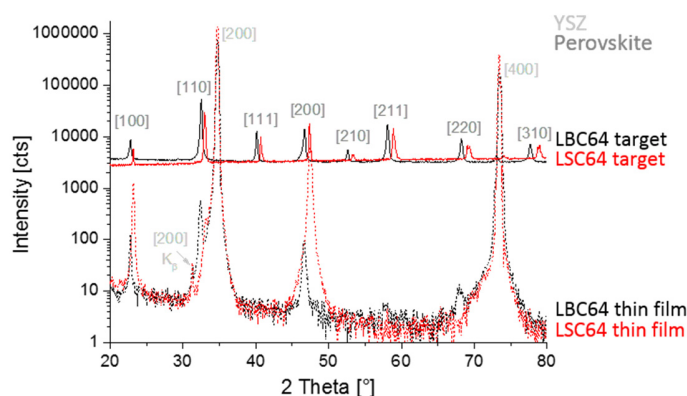


Fig. 6.2 XRD pattern of LSC64 and LBC64 PLD target and thin film deposited on YSZ.

For LSC64 and LBC64 rhombohedral angles α_r of 60.36° and 60.05° under standard conditions (298.15 K, 1 atm) can be calculated from literature^{141, 145}. Both values are close to 60° - the value for a cubic crystal structure. Generally, changes in the crystal structure symmetry of the ABO_3 perovskite family can be explained by Goldschmidt's tolerance factor t_f ¹⁴⁶. For LBC64 ($t_f \sim 1.00$) an almost ideal cubic structure is found in contrast to the more rhombohedrally distorted LSC64 ($t_f \sim 0.98$), calculated with ionic radii from¹³⁵. The pseudo cubic lattice parameter derived from the polycrystalline target diffraction patterns for LSC ($a_{pc} = 3.838 \pm 0.003 \text{ \AA}$) and LBC ($a_{pc} = 3.889 \pm 0.002 \text{ \AA}$) agree well with literature values^{141, 145}.

The thin film patterns show the actual thin film growth relative to the (100) YSZ-plane. Therefore, both patterns are dominated by the intense (00l) peaks of the substrate. Again, no other peaks besides the substrate or the thin film peaks are found, indicating a sufficiently phase-pure deposition. Furthermore, it can be seen that both films grow preferentially in (100) and (110) direction on the substrate. Due to the small amount of thin film peaks, the out-of-plane lattice parameters for LSC ($a_{pc} = 3.83 \pm 0.01 \text{ \AA}$) and LBC ($a_{pc} = 3.90 \pm 0.01 \text{ \AA}$) can be only given with limited accuracy.

6.3.2 Initial AC measurements and equivalent circuit model

First, electrochemical impedance spectroscopy was used to measure the response of freshly deposited LSC and LBC thin films at $604 \pm 2 \text{ }^\circ\text{C}$ in synthetic air and 0.21 bar oxygen partial pressure ($p\text{O}_2$). Nyquist plots normalized to the projected electrode surface area are shown in Fig. 6.3a for LSC and Fig. 6.3b for LBC, a comparison between the two materials is made in Fig. 6.3c after subtraction of the high frequency intercept. Qualitatively, both materials show a very similar Nyquist plot.

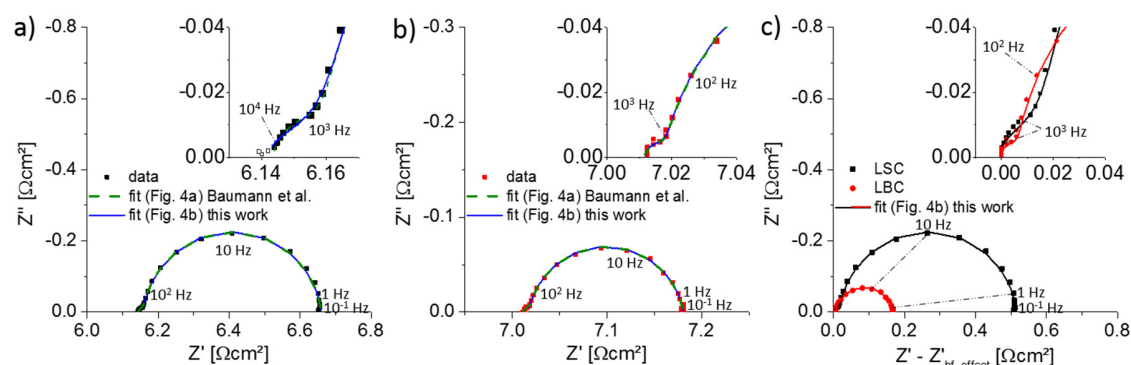


Fig. 6.3 Nyquist plots of freshly deposited (a) LSC64 and (b) LBC64 thin films at $604 \pm 2 \text{ }^\circ\text{C}$ and 0.21 bar $p\text{O}_2$. Data points represent measured values and the solid lines the corresponding fits according to the model proposed by Baumann et al.⁶⁵, Fig. 6.4a and the model used in this study, Fig. 6.4b. The insets display the medium-low frequency (25 kHz – 100 Hz) range for both materials. Fig. 6.3c shows a comparison of the two thin film materials after subtraction of the high frequency intercept.

The high-frequency intercept ($> 25 \text{ kHz}$) on the x-axis can be predominantly attributed to the oxide ion conduction in the electrolyte. In addition, the high frequency intercept is slightly higher for the LBC sample, probably because of its smaller electronic conductivity compared to LSC

(see chapter 6.3.6), which may cause an additional sheet resistance. This additional high frequency resistance amounts to 13 – 18 % of the total high frequency intercept and might indicate a slightly smaller active surface area for the LBC sample. However, compared to other effects found in this study, these differences are of minor importance and were thus not considered for the calculation of the resistive and capacitive values presented here. The electrode impedance is determined by a small shoulder at medium frequencies (25 kHz – 1 kHz) and a pronounced low frequency (1 kHz – 0.1 Hz) semicircle. It is generally agreed that the oxygen exchange resistance dominates the overall electrode impedance for thin films of the $\text{La}_{1-x}\text{Sr}_x\text{Co}_{1-y}\text{Fe}_y\text{O}_{3-\delta}$ perovskite family^{21, 113, 147, 148}. Therefore, the resistive contribution of the low frequency semicircle is associated with the oxygen exchange reaction at the surface, which is also supported by its time, temperature and pressure dependency shown in the following chapters. Accordingly, the surface exchange resistance can already be approximated from the impedance spectra without any detailed fit model.

A surface exchange resistance (R_{surf}) of $\sim 0.5 \Omega\text{cm}^2$ is found for the freshly deposited LSC thin film, which is in good agreement with literature values^{50, 100} reported for similarly prepared thin films. This indicates that, compared to other materials, already LSC thin films show excellent kinetics for the oxygen reduction reaction at 600 °C; other values are: $\text{Ba}_{0.6}\text{Sr}_{0.4}\text{Co}_{0.2}\text{Fe}_{0.8}\text{O}_{3-\delta}$ ¹⁹ $\sim 3 \Omega\text{cm}^2$, $\text{SrFeO}_{3-\delta}$ ²³ $\sim 9 \Omega\text{cm}^2$, $\text{Sm}_{0.5}\text{Sr}_{0.5}\text{CoO}_{3-\delta}$ ²¹ $\sim 14 \Omega\text{cm}^2$, $\text{La}_{0.6}\text{Sr}_{0.4}\text{Co}_{0.2}\text{Fe}_{0.8}\text{O}_{3-\delta}$ ²¹ $\sim 70 \Omega\text{cm}^2$, $\text{SrTi}_{0.95}\text{Fe}_{0.05}\text{O}_{3-\delta}$ ²³ $\sim 85 \Omega\text{cm}^2$, $\text{La}_{0.6}\text{Sr}_{0.4}\text{FeO}_{3-\delta}$ ²² $\sim 130 \Omega\text{cm}^2$. Freshly deposited LBC, however, shows an even lower surface exchange resistance than LSC; impressively small $\sim 0.17 \Omega\text{cm}^2$ can be estimated, see Fig. 6.5. This is certainly among the lowest oxygen surface exchange resistances reported so far for dense perovskite-type materials and to the best of our knowledge also the first value reported for the oxygen exchange kinetics of dense LBC thin films.

One of the major challenges in impedance spectroscopy is the quantitative evaluation of spectra in order to extract physically meaningful quantities. In general, impedance analysis is performed using equivalent circuits that consist of a network of resistors and capacitors. For a detailed analysis of the electrode impedance in Fig. 6.3 two different equivalent circuit models, see Fig. 6.4, were employed to fit the data; CPE denotes constant phase elements.

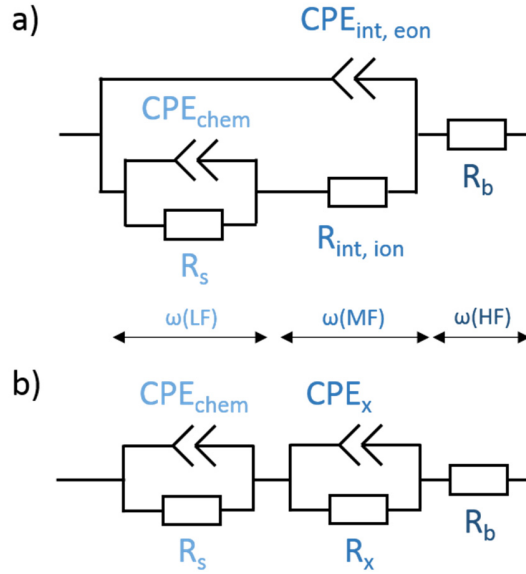


Fig. 6.4 Equivalent circuit used to fit impedance data a) by Baumann et al.⁶⁵ for $\text{La}_{0.6}\text{Sr}_{0.4}\text{Co}_{0.8}\text{Fe}_{0.2}\text{O}_{3-\delta}$ thin films and b) for LSC64 thin films in this study.

It can be seen in Fig. 6.3a and 6.3b that both models describe the measured data quite well but an excellent agreement between the equivalent circuit and the experimental data does not necessarily confirm the validity of any model. For a physical interpretation it is important to check whether the values of the fitting parameters are reasonable and show the expected dependencies on temperature, oxygen partial pressure and geometrical variations.

Baumann et al.⁶⁵ already approached this issue for $\text{La}_{0.6}\text{Sr}_{0.4}\text{Co}_{0.8}\text{Fe}_{0.2}\text{O}_{3-\delta}$ (LSCF) thin films and derived the equivalent circuit shown in Fig. 6.4a from a general description of mixed ionic-electronic conductors proposed in Ref.⁶⁷ under the assumptions of a very high ionic and electronic conductivity i.e. the oxygen incorporation into the electrolyte $\frac{1}{2} \text{O}_{2, \text{ gas}} + 2e^- \rightarrow \text{O}_{\text{electrolyte}}^{2-}$ is limited by the surface exchange and electrode-electrolyte interface transfer. In this model R_b represents the ionic bulk conductivity of the electrolyte, $R_{\text{int, ion}}$ the oxygen transfer between electrode and electrolyte and R_s the surface exchange resistance. The capacitors were replaced by constant phase elements, where

$$Z_{\text{CPE}} = \frac{1}{Q(i\omega)^n} \quad (6.1)$$

is the impedance of the constant phase element and the capacitance is calculated by

$$C = (R^{1-n} \cdot Q)^{\frac{1}{n}} \quad (6.2)$$

For $n = 1$ the impedance of the constant phase element corresponds to the impedance of an ideal capacitor. $CPE_{int, eon}$ represents the double layer capacitance expected at the interface between electrode and electrolyte due to the blockage of electronic charge carriers and C_{chem} the chemical capacitance of the thin film.

One may suggest the same equivalent circuit for our $La_{0.6}Sr_{0.4}CoO_{3-\delta}$ (LSC64) and $La_{0.6}Ba_{0.4}CoO_{3-\delta}$ (LBC64) thin films, since they also show an excellent mixed conductivity and are limited by the surface exchange reaction. However, inconsistencies with this model are found in the medium frequency regime (small shoulder), since the extracted values for an interfacial double layer capacitance are too large. Baumann⁶⁵ calculated a $C_{int, eon}$ of $\sim 100 \mu F/cm^2$ for LSCF thin films at 500 °C, while in our case much larger values are deduced from the model in Fig. 6.4a (LSC $\sim 2500 \mu F/cm^2$, LBC $\sim 10000 \mu F/cm^2$ for the two thin films at 510 °C). Yang et al.¹⁴⁹ also measured similarly high capacitances in the medium frequency range on $La_{0.5}Sr_{0.5}CoO_{3-\delta}$ thin films. Assuming a capacitor thickness as small as the interatomic distance of the two cation layers in an elementary cell ($d = 1.9 \text{ \AA}$), a relative permittivity ϵ_r can be calculated by

$$\epsilon_r = \frac{C_{int, eon}}{A} \cdot \frac{d}{\epsilon_0} \quad (6.3)$$

with $\epsilon_0 (= 8.85 \cdot 10^{-12} \text{ F/m})$ being the vacuum permittivity, and A the interfacial area. This model would deliver relative permittivity values of ≈ 430 (LSC) and ≈ 2100 (LBC). Such large ϵ_r values are hardly conceivable while the value of ≈ 21 for LSCF, calculated using $C_{int, eon}$ from Ref.⁶⁵, is still in a realistic range. Therefore, it is assumed that the high capacitance obtained at medium frequencies represents stoichiometric changes and thus also reflects a chemical capacitance. Hence, it is not appropriate to use the Baumann model (Fig. 6.4a), since a second chemical capacitance would rather be in series and not in parallel to the $R_s | CPE_{chem}$ element. Quantities discussed here are thus extracted by the modified equivalent circuit shown in Fig. 6.4b. The exact mechanisms behind CPE_x and R_x are unknown and the circuit is considered as approximation of a more complex one; values could only be determined with limited accuracy, since the overall electrode impedance is strongly dominated by the large arc, i.e. by CPE_{chem} and R_s . Exponential fitting parameters of $n \sim 0.7$ for the $R_x | CPE_x$ and $n > 0.92$ for the $R_s | CPE_{chem}$ element were determined throughout this chapter.

6.3.3 Time dependent AC measurements

Electrochemical impedance spectroscopy was used to investigate changes of the electrochemical performance for as-deposited LSC and LBC thin film electrodes at 604 ± 2 °C in synthetic air (0.21 bar pO_2) over annealing time. Impedance spectra were measured continuously in an interval of ~ 5 minutes for 15 hours. Nyquist plots normalized to the projected electrode surface area are shown in Fig. 6.5a for LSC and Fig. 6.5b for LBC thin films after the given annealing times. The points represent measured data and the straight line the fit according to the model shown in Fig. 6.4b.

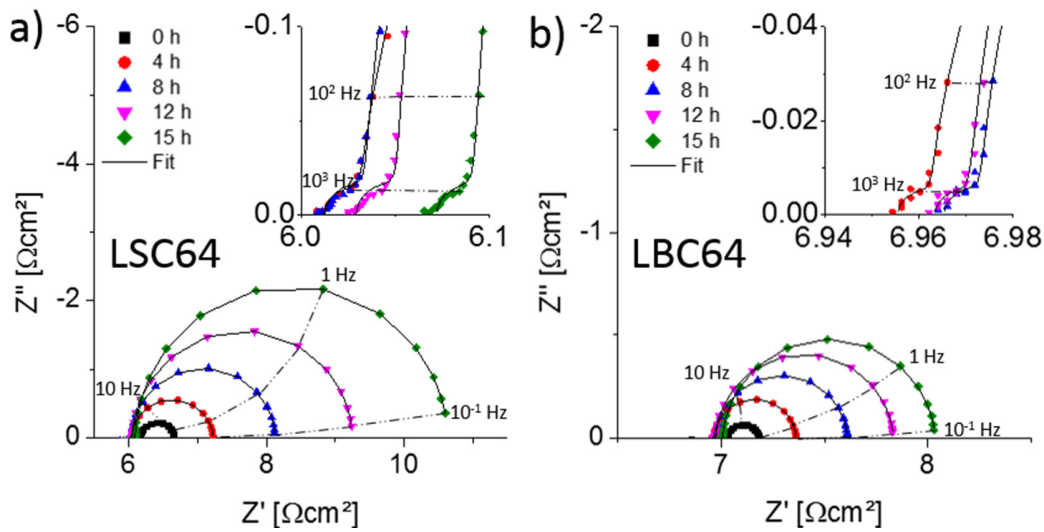


Fig. 6.5 Nyquist plots displaying the impedance change of a LSC64 (a) and LBC64 (b) thin film upon annealing at 604 °C and 0.21 bar pO_2 . Data points represent measured values and the solid line is the corresponding fit according to the model presented in Fig 4b. The insets show the medium-low frequency (25 kHz - 100 Hz) range.

Fig. 6.6a and 6.6b summarize the resistive and capacitive changes during 15 hours of annealing. The oxygen surface exchange resistance R_s increases continuously from $0.5 \Omega\text{cm}^2$ to $4.2 \Omega\text{cm}^2$ for LSC and $0.15 \Omega\text{cm}^2$ to $1 \Omega\text{cm}^2$ for LBC within 15 hours of annealing time at 600 °C. The degradation of the electrochemical exchange kinetics of LSC thin films and related materials with annealing time was often reported and mostly connected to cation stoichiometry changes at or close to the surface^{32, 53, 101}. Especially, the presence of certain atmospheric trace gases such as SO_2 , CO_2 or H_2O ^{38, 39, 111} as well as Si or Cr sources in the vicinity of perovskite samples in wet atmosphere are known to decrease the electrode performance by formation of Sr rich phases on the surface^{37, 41}. However, special care was attributed to avoiding any contaminations of the atmosphere during the annealing procedure, see chapter 6.2.3. For similarly prepared LSC thin films it was already

shown in chapter 4.3.3 by low-energy ion sputtering and on-line inductively coupled plasma mass spectrometry that degradation during annealing (in the same setup) is not necessarily connected to severe cation stoichiometry changes at the surface. It is beyond the scope of this paper to clarify reasons of the changes measured here but they have to be kept in mind when analyzing activation energies (chapter 6.3.4).

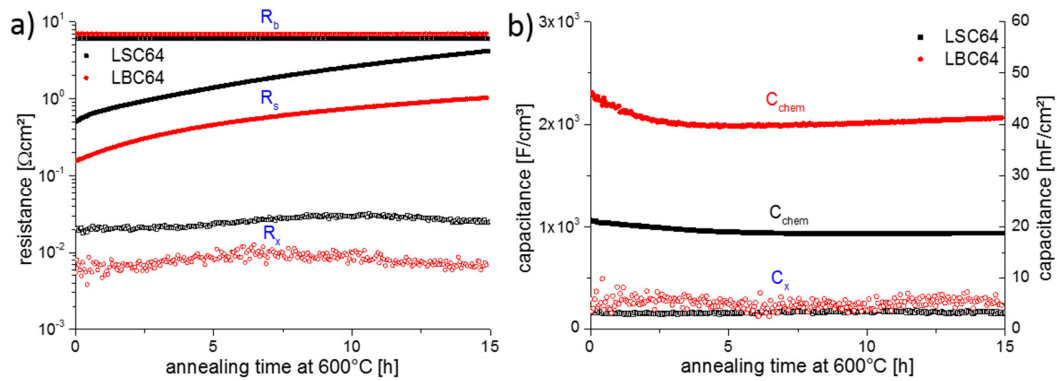


Fig. 6.6 Variation of the (a) resistive and (b) capacitive quantities of LSC64 and LBC64 thin films with annealing time at 600 °C and 0.21 bar pO_2 . All values are normalized to the projected surface area (R_s , R_x , R_b , C_x) or the film volume (C_{chem}).

C_{chem} decreases within the first 5 hours from 1050 Fcm^{-3} to 950 Fcm^{-3} for LSC and from 2300 Fcm^{-3} to 2000 Fcm^{-3} for LBC. This minor variation may be due to morphological changes of the thin film since the samples were only shortly at such temperatures during deposition (20 minutes). The higher C_{chem} values for LBC reflects its ability to undergo larger stoichiometric changes upon polarization in comparison to LSC. For C_x , measured at medium frequencies, very high values in the order of 4 to 7 mF/cm^2 were obtained. Neither C_x nor R_x show substantial changes with annealing time for both materials; R_x is 1-2 orders of magnitude smaller than R_s at the start of the measurement. For both materials R_b remains the same and is close to the expected value assuming a YSZ ionic conductivity of $4.75 \cdot 10^{-3} \text{ S/cm}$ at 600 °C.

6.3.4 Temperature dependent AC measurements

Freshly deposited LSC and LBC thin films were thermally equilibrated in synthetic air at 604 °C for 1 h and then measured between 604 °C and 463 °C with intervals of 22-24 °C. A total of 8 temperature cycles (each consisting of 1 heating and 1 cooling subcycle) was measured for both materials with each temperature cycle taking approx. 8 hours. Representative Nyquist plots at different temperatures during the first temperature cycle are shown in Fig. 6.7. A very good agreement between equivalent circuit fit (solid line) and measured data (points) is found over the whole temperature range.

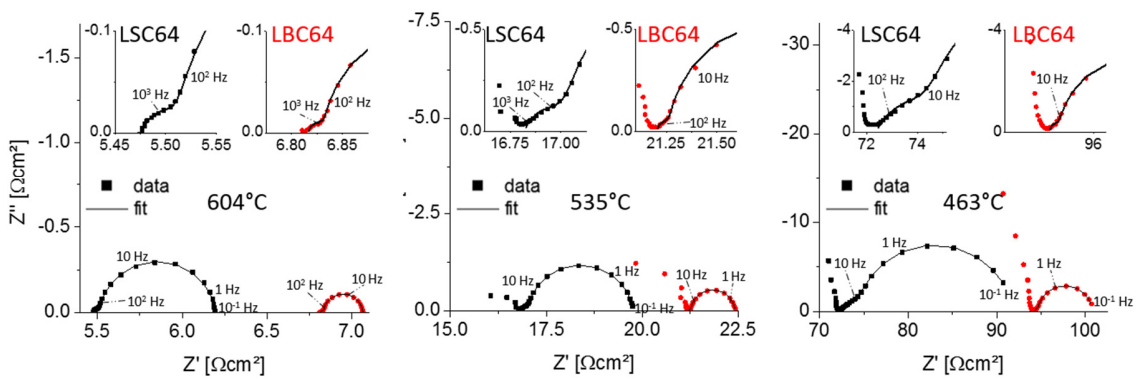


Fig. 6.7 Nyquist plots displaying the dependence of the (a) LSC64 and (b) LBC64 thin films on temperature at 0.21 bar pO_2 . Data points represent measured values and the solid line the corresponding fit according to the model presented in Fig 4b. The insets show the medium-low frequency (25 kHz – 100 Hz) range for both materials.

The general shape of the impedance spectra at medium and low frequencies does not change at lower temperatures. However, at higher frequencies (>10 kHz) the onset of a semicircle is observed, which represents the ionic resistance of the YSZ electrolyte in parallel to its geometrical capacitance. This part of the spectra was not visible at 604 °C, because of the higher bulk relaxation frequency which is proportional to the ionic conductivity. The higher R_b value found for the LBC sample may be again attributed to a sheet resistance and thus slightly decreased active area of the electrode. Arrhenius plots of the resistances and capacitances extracted from the first temperature cycle together with their activation energies are shown in Fig. 6.8. For all quantities, except C_x of LBC, an Arrhenius-type behavior could be determined. The activation energies obtained for $1/R_b$, for example, are 1.02 ± 0.01 eV for LSC and 1.04 ± 0.01 eV for LBC, and agree well with literature values reported for the ionic bulk conductivity of 9.5 mol % YSZ single crystals, 1.07 ± 0.06 eV^{65, 149-151}.

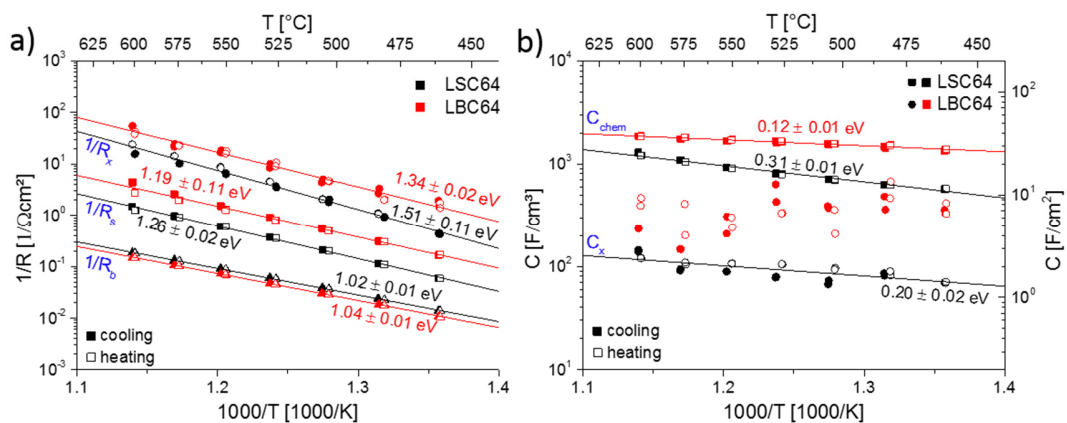


Fig. 6.8 Arrhenius plots of the (a) resistive and (b) capacitive quantities of LSC64 and LBC64 thin films at 0.21 bar pO_2 measured during the first cooling (■) and heating (□) subcycle. The activation energies determined from these data are also given.

The activation energy of the oxygen surface exchange is 1.26 ± 0.02 eV for LSC and 1.19 ± 0.11 eV for LBC, calculated from all data of the first temperature cycle. However, as already mentioned in chapter 6.3.3 degradation occurs, leading to an increase of the surface exchange resistance with annealing time also during the temperature cycles, see Fig. 6.9a. The increase of the absolute values is accompanied by a continuous increase of the activation energy with number of temperature cycles, as can be seen in Fig 9b. The activation energy calculated from the last (8th) temperature cycle amounts to 1.33 ± 0.04 eV for LSC and 1.33 ± 0.02 eV for LBC. The surface exchange resistance continuously increases during the temperature cycles. Therefore, the activation energy is shifted to lower values when calculated from a heating subcycle only and to higher values when calculated from a cooling subcycle. The averaged activation energies are shown in Fig. 6.9b by a polynomial approximation.

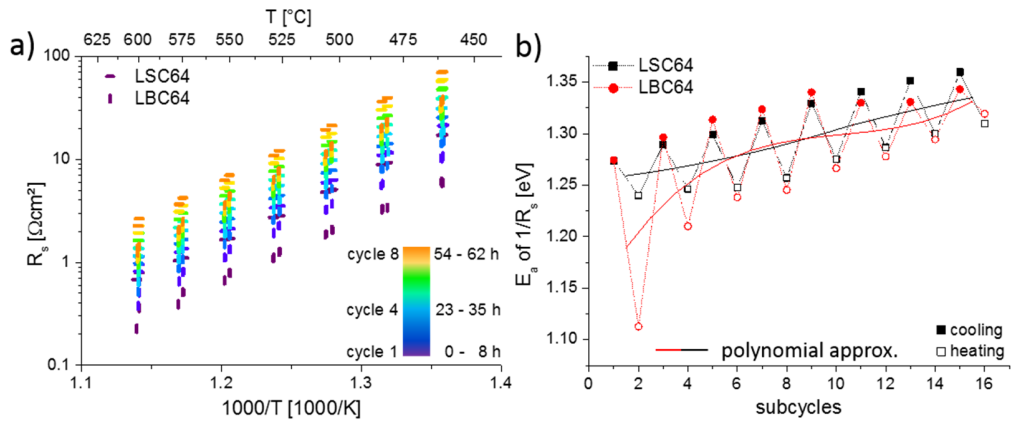


Fig. 6.9 (a) Arrhenius plot of the surface exchange resistance of LSC64 and LBC64 thin films at 0.21 bar pO₂. For each thin film 8 temperature cycles (cooling and heating) were performed within 62 hours. (b) The activation energies of 1/R_s, calculated from each subcycle of (a) and a polynomial approximation is shown (solid line).

For both materials a similar pre-exponential factor of the Arrhenius equation, $5 \cdot 10^{-8} \pm 2 \cdot 10^{-8} \text{ } \Omega\text{cm}^2$ for LSC and $4 \cdot 10^{-8} \pm 3 \cdot 10^{-8} \text{ } \Omega\text{cm}^2$ for LBC, is found. Hence, the different oxygen exchange kinetics of the two materials can be mainly attributed to the different activation energies. Moreover, the pre-exponential factor changes by less than 10 % during the course of the 8 temperature cycles. Since, it includes the number of sites participating in the oxygen exchange reaction, it is reasonable to conclude from this constancy that only a small fraction of those sites becomes deactivated during the course of the measurements. Thus, mainly the change of the activation energy causes degradation. This change may reflect a homogenous and continuous variation of the chemical environment of active surface sites. However, for LSC and most other MIECs it is still under debate, which elementary step is rate limiting during the oxygen incorporation i.e. adsorption, dissociation, charge transfer. Hence, it is also difficult to find a more detailed explanation for the degradation. Regardless of the drifting activation energy, it has to be emphasized that both, LSC and LBC, show very low activation energies for the oxygen incorporation compared to other MIEC perovskite-type materials. This makes both of them and especially LBC due to its low absolute polarization resistance highly attractive for the use in intermediate-temperature SOFCs.

For the unknown interfacial process, represented by R_x, an activation energy of $1.51 \pm 0.11 \text{ eV}$ for LSC and $1.34 \pm 0.02 \text{ eV}$ for LBC was calculated. As already discussed in chapter 6.2.3, Baumann et al. assigned this resistive contribution to the transfer of O²⁻ ions across the electrode/electrolyte boundary and determined an activation energy of $1.55 \pm 0.05 \text{ eV}$ for La_{0.6}Sr_{0.4}Co_{0.8}Fe_{0.2}O_{3-δ} thin

films⁶⁵. Yang et al. assumed a similar reaction mechanism for the medium frequency range and obtained an activation energy of 1.6 eV for $\text{La}_{0.5}\text{Sr}_{0.5}\text{CoO}_{3-\delta}$ thin films¹⁴⁹. A more detailed discussion of this minor part to the overall polarization resistance is beyond the scope of this paper.

Fig. 6.8b shows the activation energies of C_{chem} for LSC (0.31 ± 0.01 eV) and LBC (0.12 ± 0.01 eV). C_{chem} is proportional to $\partial\delta/\partial\mu_{\text{O}}$, with μ_{O} being the chemical potential of oxygen in the electrode. Thus, a positive activation energy is in accordance with data obtained by coulometric titration¹⁵² and thermogravimetry¹⁵³ for polycrystalline $\text{La}_{0.6}\text{Sr}_{0.4}\text{CoO}_{3-\delta}$ and $\text{La}_{0.7}\text{Sr}_{0.3}\text{CoO}_{3-\delta}$ bulk samples respectively. A detailed discussion of C_{chem} and a comparison to literature values is given in chapter 6.3.5. For LBC a clear trend of the temperature dependence of C_x could not be observed. However, for the LSC thin films an activation energy of 0.20 ± 0.02 eV was determined. The positive activation energy again highlights the difference to the interfacial capacitance reported in Ref. ⁶⁵ for $\text{La}_{0.6}\text{Sr}_{0.4}\text{Co}_{0.8}\text{Fe}_{0.2}\text{O}_{3-\delta}$ thin films, the latter is negatively thermally activated by -0.15 ± 0.05 eV.

6.3.5 $p\text{O}_2$ dependent AC measurements

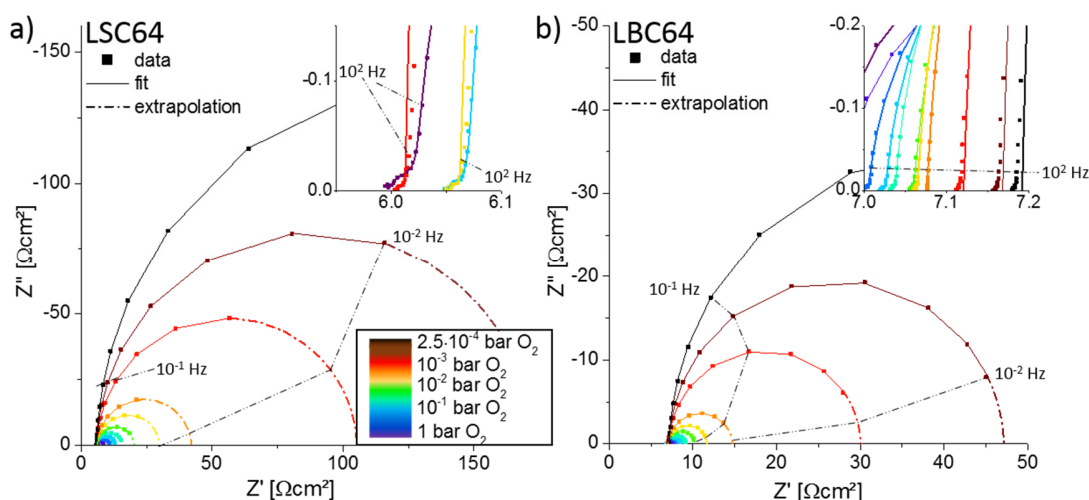


Fig. 6.10 Nyquist plots displaying the dependence of the LSC64 and LBC64 thin film impedance on $p\text{O}_2$ at 600 °C. Data points represent measured values and the solid line the corresponding fit according to the model presented in Fig 4b. The insets show the medium-low frequency (25 kHz – 100 Hz) range for both materials. For a better overview, only a limited selection of graphs is displayed in the inset of (a)

Subsequent to the time dependent measurements, see chapter 6.3.3, EIS analysis was performed on both materials at constant temperature (604 °C) but different atmospheres. The ratio of the O_2/N_2 gas mixture was changed using mass flow controllers to vary the oxygen partial pressure

(pO_2) between 1 and $2.1 \cdot 10^{-4}$ bar pO_2 . A pO_2 cycle from 0.21 to $2.1 \cdot 10^{-4}$ and back to 1 bar pO_2 was recorded for both materials within 10 hours. Qualitatively, degradation slowed down at lower oxygen partial pressures and therefore values obtained during the decreasing and increasing pO_2 subcycle are in good accordance. In Fig. 6.10 Nyquist plots are shown for the whole oxygen partial pressure range and both materials. It can be seen that the fit becomes less accurate in the medium frequency range for measurements performed at lower oxygen partial pressures ($\leq 10^{-2}$ bar pO_2), see insets in Fig. 6.10a and 6.10b. Therefore, it was not possible to extract the quantities R_x and C_x for LBC at oxygen partial pressures below $5 \cdot 10^{-2}$ bar pO_2 . These deviations, however, do not affect the much larger quantities R_s and C_{chem} .

Moreover, some minor dependence of the high frequency intercept on pO_2 was observed for both samples. While for the LSC sample the changes can be most probably attributed to small temperature fluctuations due to different gas fluxes, the high frequency intercept of the LBC samples systematically increases with decreasing pO_2 . Under equilibrium conditions oxygen is removed from the electrode bulk at lower oxygen partial pressures. According to the reaction $O_x \rightleftharpoons 1/2 O_2 + 2e^- + V_O^{\bullet\bullet}$ electrons are left behind in the electrode. Those recombine with holes $h^+ + e^- \rightleftharpoons nil$ and this usually decreases the conductivity of a p-type material. Hence, for the slightly less conductive LBC (see below) an increase of the already existing sheet resistance may cause the shift of the high frequency intercept, R_b , with decreasing pO_2 .

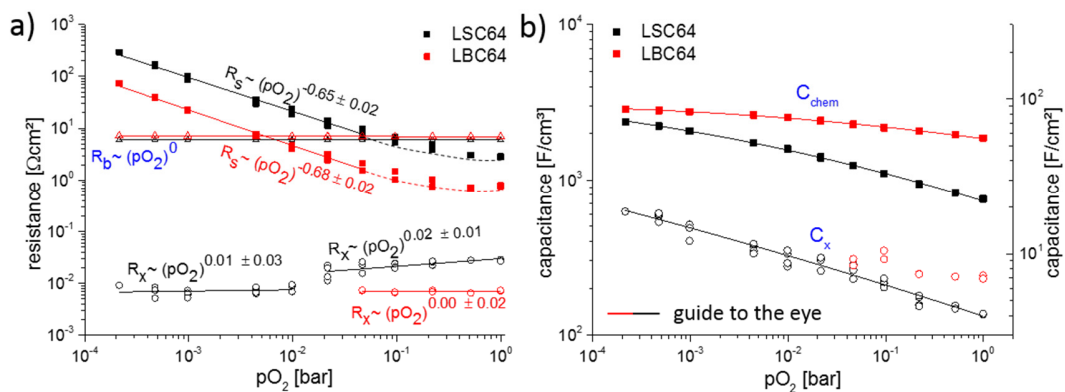


Fig. 6.11 Dependence of the (a) resistive and (b) capacitive quantities of LSC64 and LBC64 thin films on pO_2 at 600 °C. Power laws according to $R_s \sim (pO_2)^m$ are highlighted together with their linear fit (solid lines) in (a). The solid lines in (b) represent a guide to the eye.

The oxygen surface exchange resistance exhibits a power law behavior $R_s \sim (pO_2)^m$ for $pO_2 < 5 \cdot 10^{-2}$ bar. For both materials, exponents m between -0.65 to -0.68 are found, see Fig. 6.11. At higher pressures the pO_2 dependence becomes very weak. This is most probably not caused by a change of the rate limiting step to ionic transport; a change of the impedance shape from a semicircle to a Warburg element is not observed and the exponential fitting parameter n of the CPE elements was > 0.98 at 1 bar pO_2 . The very similar pO_2 dependence of R_s for LSC and LBC again support the assumption that the oxygen reduction mechanism and rate limiting step are the same and only differ in their activation energy. However, a detailed mechanistic interpretation of the pO_2 dependence is far from trivial since pO_2 not only affects the concentration of adsorbed species but also all defect concentrations in the MIEC. Such a defect chemical analysis is beyond the scope of this work. R_x exhibits large fitting errors of approx. 30-80 % for both materials and does not show a clear dependence on the oxygen partial pressure. Also the step change of R_x in Fig. 6.11a between $1 \cdot 10^{-2}$ and $2 \cdot 10^{-2}$ bar pO_2 for LSC most probably originates from fit inaccuracies.

Fig. 6.11b shows that C_{chem} and C_x of both materials decrease with increasing oxygen partial pressure, which supports the assumption of C_x also being a chemical capacitance (of the interface). C_{chem} of LBC is larger than for LSC over the measured partial pressure range but the difference decreases towards lower pO_2 . The larger C_{chem} of LBC indicates that the material is more ready for stoichiometry changes, i.e. is easier to reduce compared to LSC. This may be due to the fact that the larger ionic radius of Ba leads to an increased lattice parameter, as shown in Sec 3.1, and thereby offers more space to form oxygen vacancies and reduced (larger) B cations¹⁵⁴. A similar observation was made on $Ba_xSr_{1-x}Ti_{1-y}Fe_yO_{3-\delta}$ bulk samples using thermogravimetry to analyze the oxygen vacancy concentration^{136, 137}. It was found that the non-stoichiometry curve is shifted to higher pO_2 with higher amounts of Ba. In analogy, one may assume that the LBC- C_{chem} curve in Fig. 6.11b is shifted compared to LSC by about 3-4 orders of magnitude in pO_2 and thus that LBC has a higher vacancy concentration due a lower vacancy formation enthalpy. Unfortunately, C_{chem} cannot be used to directly determine the concentration of oxygen vacancies, which are the minority charge carriers in the measured pO_2 range, since the prerequisite of a dilute system is not fulfilled to apply the corresponding simplified equations⁶⁷.

Nonetheless, the measured chemical capacitances of LSC may be compared with those expected from non-stoichiometry data of bulk samples. The chemical capacitance is given by

$$C_{chem} = \frac{4 \cdot F^2}{V_M} \frac{d(3-\delta)}{d\mu_O} \quad (6.4)$$

with F being the Faraday constant ($96485 \text{ C}\cdot\text{mol}^{-1}$) and V_M denoting the molar volume of LSC64 ($39.12 \text{ cm}^3\cdot\text{mol}^{-1}$). The non-stoichiometry data from Lankhorst et al.¹⁵⁵, Kawada et al./Mizusaki et al.^{153, 156} and Kuhn et al.¹⁵⁷ for bulk samples were numerically evaluated in terms of eq. 6.4. The resulting C_{chem} values are plotted in Fig. 6.12 together with C_{chem} values directly obtained from the impedance measurements in our study but also from measurements on thin films by Kawada²³ and Yang ($\text{La}_{0.5}\text{Sr}_{0.5}\text{CoO}_{3-6}$)¹⁴⁹ at $600 \text{ }^\circ\text{C}$ and different oxygen partial pressures. It can be seen that our data fit rather well to the bulk based models from Lankhorst, Kawada/Mizusaki and Kuhn, C_{chem} values of the three latter deviate from each other by less than 50 %. In contrast to this, the C_{chem} values extracted from thin films on $\text{Ce}_{0.9}\text{Gd}_{0.1}\text{O}_{1.95}$ (GDC) by Kawada¹⁵⁶ are a factor of 2-3 lower. Possibly epitaxial growth of LSC64 on top of GDC restricts chemical expansion of the LSC layer i.e. formation of oxygen vacancies while expansion restriction from the substrate is less pronounced in our thin films. Our measured data are therefore only slightly shifted to lower oxygen partial pressures compared to bulk data.

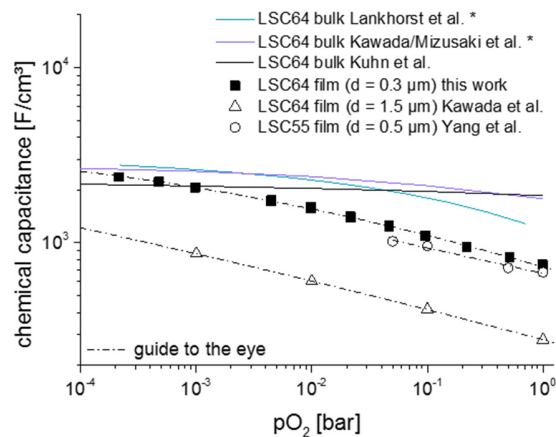


Fig. 6.12 Dependence of the chemical capacitance on $p\text{O}_2$ at $600 \text{ }^\circ\text{C}$ for LSC64 and LSC55, respectively. Data determined from $\delta(\mu_{\text{O}})$ slopes of thermogravimetry and coulometric titration measurements by Lankhorst¹⁵⁵, Kawada/Mizusaki^{153, 156} and Kuhn¹⁵⁷ on bulk samples (solid line) are shown together with data extracted from impedance measurements on thin films by Kawada²³ and Yang¹⁴⁹ (open symbols). The asterisk (*) denotes that data had to be extrapolated, d is the thickness of the thin films. A dashed line is drawn as guide to the eye.

6.3.6 Van der Pauw – electronic conductivity

Resistivity measurements using the van der Pauw method¹⁴⁴ were performed on LSC and LBC thin films at $0.21 \text{ bar } p\text{O}_2$ and different temperatures ($80 - 600 \text{ }^\circ\text{C}$). This technique is able to determine the thin film resistivity irrespective of the contact placement and the shape of the sample (as long

as point contacts are at the periphery of the specimen). To ensure that the YSZ substrate does not influence the thin film conductivity measurement, the conductivity of YSZ obtained during the impedance measurement at 600 °C, $4.75 \cdot 10^{-3}$ S/cm, is used to compare sheet resistances of substrate and film. From $R_{sheet} = \frac{1}{\sigma \cdot d}$, with d being the film thickness, the measured sheet resistance of the thin film is in the 1 % range of the substrate sheet resistance and thus a substrate effect can be safely neglected.

The temperature dependent electronic conductivity resulting after one hour thermal equilibration at 600 °C is shown in Fig. 6.13 for both materials. LSC is known to be primarily electron conducting under these condition and also LBC thin films revealed conductivity values far above any conceivable ionic conductivity. The samples were equilibrated for 1 hour at 600 °C before several temperature cycles were started. In Fig. 6.13a it can be seen that for both materials a conductivity maximum is found (LSC $\sigma_{eon} = 1028$ S/cm at 382 ± 8 °C, LBC 839 S/cm at 442 ± 5 °C. At higher temperatures, σ_{eon} decreases as one would expect for metallic conductivity. The maximum of σ_{eon} for LSC is observed close to the phase transition temperature of ~ 390 °C for bulk samples, where the crystal lattice changes from the low temperature rhombohedral into a cubic structure. However, for bulk LSC64 samples the maximum of σ_{eon} was found to be close to 0 °C¹²⁹. A hysteresis like behavior is measured for the LBC sample for yet unknown reasons.

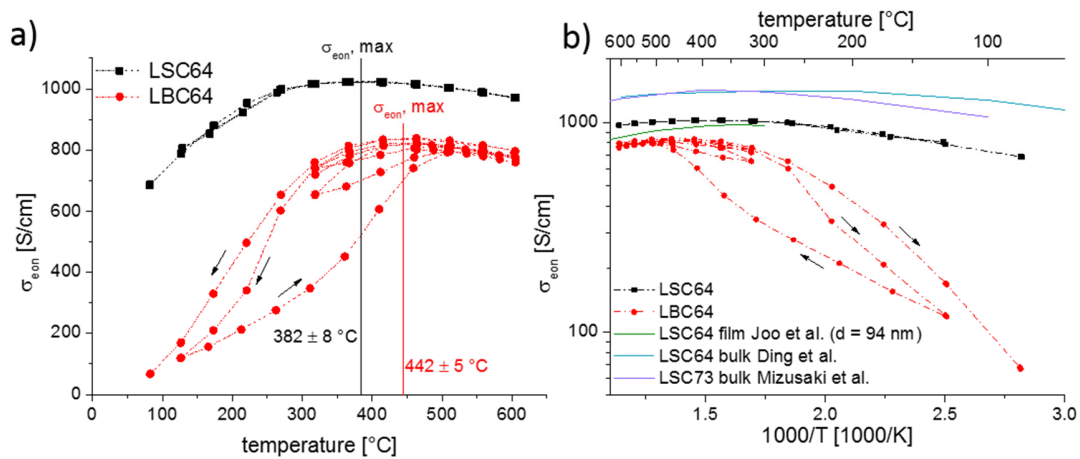


Fig. 6.13 Electronic conductivity measured by van der Pauw method for LSC64 and LBC64 thin films at different temperatures and 0.21 bar p_{O_2} in linear (a) and logarithmic (b) plots; dashed lines serve as guide to the eye. Literature data measured on bulk samples by Ding¹⁵⁸ and Mizusaki¹²⁹ and on thin films by Joo¹⁵⁹ are also plotted as reference in (b).

In Fig. 6.13b additional measurements from Ding et al.¹⁵⁸ and Mizusaki et al.¹²⁹ on LSC64 and LSC73 bulk samples, respectively, are plotted together with LSC64 thin film measurements conducted by Joo et al.¹⁵⁹. While the thin film data of Joo and our results correspond well, a difference of about 40 % is found between thin film and bulk samples. This could again be caused by defect chemical differences between bulk and thin film but might also be due to the columnar microstructure of our thin films, since the grain boundaries may have a higher resistivity. The somewhat smaller electronic conductivity of LBC was already mentioned in chapter 6.3.2 as the possible cause of an increased high frequency intercept. However, above 400 °C the conductivity is still far beyond that of most SOFC cathode materials such as $\text{La}_{1-x}\text{Sr}_x\text{MnO}_{3-\delta}$ and $\text{La}_{1-x}\text{Sr}_x\text{FeO}_{3-\delta}$ and sufficient for excellent cathodes. Hence, it can be concluded that based on its superior oxygen exchange activity LBC is a highly promising material for intermediate temperature SOFCs.

6.4. Conclusions

An extraordinarily high catalytic activity of dense $\text{La}_{0.6}\text{Ba}_{0.4}\text{CoO}_{3-\delta}$ (LBC) thin film model electrodes for the oxygen surface exchange was revealed. A comparative study with $\text{La}_{0.6}\text{Sr}_{0.4}\text{CoO}_{3-\delta}$ (LSC) thin films showed that the oxygen incorporation of both perovskite-type material is limited by the oxygen surface exchange reaction in the temperature range of 450 – 600 °C. The surface exchange resistance R_s in synthetic air, already known to be very low for LSC (0.5 - 0.7 Ωcm^2 at 604 °C, 17 – 18 Ωcm^2 at 463 °C) is even lower for LBC (0.15 - 0.22 Ωcm^2 at 604 °C, 5.8 – 6 Ωcm^2 at 463 °C). Furthermore, a very low activation energy of R_s was found for both materials (LSC 1.26 ± 0.11 eV, LBC 1.19 ± 0.11 eV) in the temperature range relevant for intermediate temperature SOFC applications.

A very similar oxygen partial pressure dependency of the surface exchange resistance was found for both materials and together with other similarities this suggests the same oxygen incorporation mechanism. Differences and variations of R_s are mainly caused by changes of the activation energy. The larger chemical capacitance of LBC is attributed to an increased reducibility of the perovskite lattice caused by the introduction of the larger Ba ion in comparison to Sr. Chemical capacitances of LSC films are close to those expected from bulk defect chemical data. The temperature dependence of the electronic conductivity revealed a maximum for LSC $\sigma_{\text{eon}} = 1028$ S/cm at 382 ± 8 °C and LBC 839 S/cm at 442 ± 5 °C. At all relevant temperatures, conductivity values are by far sufficient for application in SOFCs.

7 Electronic and ionic conductivity of $\text{La}_{0.95}\text{Sr}_{0.05}\text{Ga}_{0.95}\text{Mg}_{0.05}\text{O}_{3-\delta}$ (LSGM) single crystals

This chapter contains in large parts material submitted as a scientific paper to the Journal of The Electrochemical Society.

7.1 Introduction

Strontium and magnesium doped lanthanum gallate (LSGM) has been widely investigated as potential electrolyte material in solid oxide fuel cells (SOFC) and thus as promising alternative to the fluorite type electrolytes yttria stabilized zirconia (YSZ) and gadolinium doped ceria (GDC). At lower temperatures ($< 700\text{ }^{\circ}\text{C}$) the ionic conductivity of LSGM can exceed the conductivity of YSZ by more than a factor of 5¹⁶⁰⁻¹⁶². Although the ionic conductivity below ca. $600\text{ }^{\circ}\text{C}$ is smaller compared to GDC, LSGM has the advantage of a broad electrolytic domain with negligible electronic conductivity under typical reducing and oxidizing conditions of SOFCs^{163, 164}. However, electrochemical properties of LSGM have been investigated almost exclusively on polycrystalline samples^{160, 165-170}, in contrast to YSZ where many studies are also available on single crystals. This is largely because of the difficulty to synthesize larger single crystals of the preferred composition $\text{La}_{0.8}\text{Sr}_{0.2}\text{Ga}_{0.8}\text{Mg}_{0.2}\text{O}_{3-\delta}$ with sufficient quality. The very few existing studies on LSGM, mostly with lower dopant concentration, dealt with crystal structure, thermal conductivity and ionic conductivity^{166, 171}. Detailed information on the electronic conductivity of LSGM single crystals is not available so far.

Measurements on polycrystalline materials often suffer from difficulties to discriminate between effects induced by grains and grain boundaries. In principle, impedance spectroscopy allows separation of resistive grain and grain boundary contributions and often a brick layer model is used for data analysis^{150, 172, 173}. However, this approach only works at lower temperatures (due to the limited frequency range of impedance spectroscopy) and for the total conductivity, which is largely ionic in LSGM. A separation of resistive bulk and grain boundary contributions of electrons in LSGM is highly non-trivial and electronic conductivities determined on polycrystals may not reflect true bulk properties. Also identification of fast conduction paths along grain boundaries

fails in conventional impedance studies¹⁷⁴. Hence, additional experiments on single crystals are very helpful for understanding the defect chemistry and charge transport properties of LSGM.

For the results presented in this chapter, a $\text{La}_{0.95}\text{Sr}_{0.05}\text{Ga}_{0.95}\text{Mg}_{0.05}\text{O}_{3-\delta}$ single crystal was grown by the Czochralsky technique in the group of oxide crystal growth of the polish academy of science by M. Glowacki. This crystal was used in an impedance study over a wide temperature (180 – 800 °C) and oxygen partial pressure range (0.21 – 1013 mbar p_{O_2}). Usage of ion blocking electrodes revealed information on electronic and ionic conductivities. Data analysis is based on the general equivalent circuit model introduced in Ref. ⁶⁷ by J. Jamnik and J. Maier for mixed ionic and electronic conductors (MIEC). This very general model was successfully applied for the analysis of Pt|GDC|Pt¹⁷⁵ and Ag|AgI|Ag₂S|AgI|Ag¹⁷⁶ electrochemical cells and allows a detailed evaluation of the charge carrier properties and defect chemistry of MIECs. Complementary Hebb-Wagner type DC polarization experiments with one reversible $\text{La}_{0.6}\text{Sr}_{0.4}\text{CoO}_{3-\delta}$ electrode were carried out to determine both n- and p-type conductivities and to verify the results obtained by the AC impedance measurements.

7.2 Experimental

7.2.1 LSGM single crystal synthesis and substrate preparation

The $\text{La}_{0.95}\text{Sr}_{0.05}\text{Ga}_{0.95}\text{Mg}_{0.05}\text{O}_{3-\delta}$ single crystal was grown by the Czochralski method using the following starting materials: La_2O_3 (4N purity), Ga_2O_3 (4N5 purity), SrCO_3 (4N5 purity) and MgO (4N purity). Reagents were dried for 6 hours – oxides at 1000 °C and SrCO_3 at 300 °C – before they were mixed in stoichiometric ratio and melted in an iridium crucible. A single crystal (20 mm \varnothing , ~35 mm length) with convex crystal-melt interface was grown on (001) LaGaO_3 oriented seed with a pulling rate of 2.5 mm/h and a rotation speed of 20 rpm under ambient pressure in a nitrogen atmosphere. Then, the LSGM single crystal was cut into smaller specimen (5 x 5 x 0.5 mm³) by CrysTec GmbH (Germany) and the front and back side (001 oriented) of the single crystals were polished (epitaxy ready).

7.2.2 Sample preparation for AC impedance measurements

A 400 nm Pt thin film was deposited on top of the as-prepared LSGM single crystals by a sputter coater (MED 020 Coating System, BAL-TEC, Germany) using a Pt (99.95 % Pt, ÖGUSSA, Austria) target. Deposition was performed at room temperature in $2 \cdot 10^{-2}$ mbar Ar atmosphere and the film thickness was controlled during sputtering by a quartz micro-balance. After deposition the sample was turned and the sputter process was repeated to obtain a similar Pt thin film electrode on the back side. Finally, the side faces of the samples were grinded to remove any residual Pt. The microstructure of similarly prepared ~ 350 nm thin Pt films on top of yttria stabilized zirconia single crystals before and after annealing at 750 °C for 2 h is shown in Ref. ¹⁷⁷. These Pt electrodes turned out to be almost entirely blocking for oxygen exchange (see chapter 7.3) and thus allowed to gain information on both ionic and electronic charge carriers.

7.2.3 Sample preparation for Hebb-Wagner type polarization

After sputtering a 400 nm Pt thin film on one side of the LSGM single crystal, as described above, a $\text{La}_{0.6}\text{Sr}_{0.4}\text{CoO}_{3-\delta}$ (LSC) layer was deposited on the back side of the sample by pulsed laser deposition (PLD). The LSC target preparation for PLD is described elsewhere¹²⁰. For the pulsed laser deposition, the substrate was heated to ~ 600 °C in $4 \cdot 10^{-2}$ mbar pO_2 and the substrate to target distance was set to 6 cm. Ablation of the target material was carried out by a KrF ($\lambda = 248$ nm) excimer laser (Lambda COMPexPro 201F, Coherent, Germany) operated at a pulse repetition rate of 5 Hz, a pulse duration of 50 ns and a laser fluence of approximately $1.5 \text{ J} \cdot \text{cm}^{-2}$ at the target. By applying 1,025 laser pulses to the LSC target a thin film of approx. 50 nm thickness was grown on the substrate. After deposition, the sample was cooled in the same atmosphere at a cooling rate of $12 \text{ °C} \cdot \text{min}^{-1}$.

Afterwards, a lift-off photolithographic process step was used to fabricate a current collector grid (35 μm mesh size, 15 μm stripe width) from a 5 nm Ti (ÖGUSSA, Austria) and 100 nm Pt thin film, sputtered on top of the LSC layer at room temperature in $7 \cdot 10^{-3}$ and $2 \cdot 10^{-2}$ mbar Ar atmosphere. The Ti between the LSC and Pt film acted as an adhesive layer. Finally, the side faces of the LSGM single crystals were grinded to remove any residual Pt or LSC. The LSC layer with current collectors acted as a reversible electrode with low oxygen exchange resistance¹²⁰.

7.2.4 Structural characterization

Diffraction patterns of the LSGM single crystal with and without LSC thin film as well as reciprocal space maps were obtained using a diffractometer (D8-Discover, Bruker AXS, Germany) in parallel beam geometry equipped with a general area detector diffraction system (GADDS). One LSGM single crystal was powderized in a tungsten carbide mortar and analyzed in Bragg Brentano geometry by a powder diffractometer (X'Pert Powder, PANalytical, Netherlands).

7.2.5 Sample setup and electrochemical measurements

All annealing and impedance experiments were performed in a cleaned quartz tube which was evacuated and refilled several times with a 79 % N₂ (ALPHAGAZ™ 1 >99.999 mol% nitrogen, Air Liquide, Austria)/ 21 % O₂ (ALPHAGAZ™ 1 >99.998 mol% oxygen, Air Liquide) mixture before the sample was uniformly heated in a tube furnace. Samples were sandwiched between two platinum foils for the impedance and DC polarization experiments. Temperature series from 180 °C → 800 °C → 180 °C → 800 °C with 50 °C step size were used in the AC experiment. When the temperature or atmosphere was changed the sample was given at least ½ h to equilibrate before any measurements were started. Absence of any significant time dependence suggest equilibration with the gas atmosphere in all measurements. Oxygen partial pressure variations were performed from 550 – 800 °C and were archived by different high purity N₂/O₂ or N₂/0.99 %O₂ (pre-mixture of 0.99 ± 0.02 %O₂ in N₂, Air Liquide) mixtures using mass flow controllers. The pO₂ was measured by a lambda probe (Micropoas™, Setnag, France) placed in the vicinity of the specimen.

Impedance measurements were performed using an impedance analyzer (Alpha A High Performance Frequency Analyzer with a POT/GAL 30 V 2 A Test Interface, Novocontrol, Germany) in the frequency range from 10⁶ Hz to a minimum of 5·10⁻³ Hz with a resolution of five points per decade and an alternating voltage of 10 mV (rms) applied between the two electrodes. The impedance spectra were quantitatively evaluated by a complex nonlinear least square fit program (Z-View2, Scribner, USA). The equivalent circuits used to fit the experimental data are shown in the respective chapters. The serial 2-point Pt wire resistance was separately measured and taken into account in the equivalent circuit fits (not explicitly shown). It was determined by a temperature cycle without any sample, i.e. with the two Pt foils being in contact. The same

measurement setup, including the potentiostat as DC voltage source, was also used in the Hebb-Wagner type polarization experiments.

7.3 Results

7.3.1 Structural characterization

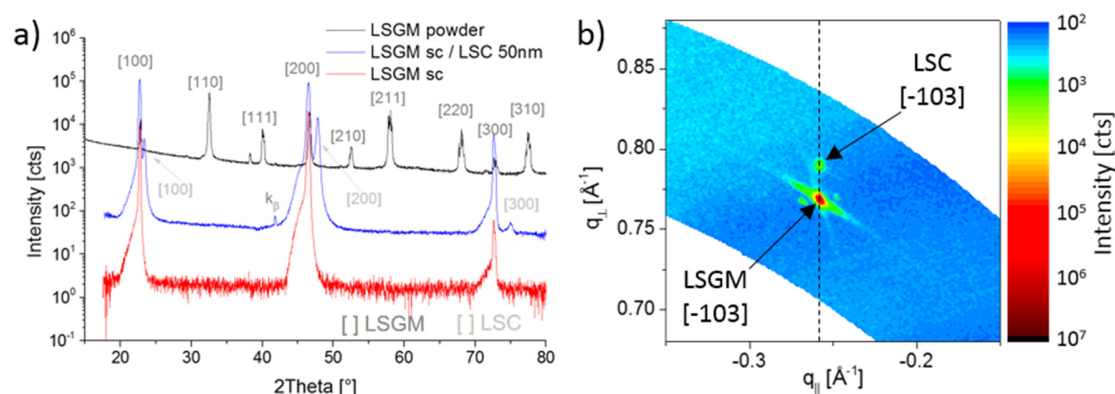


Fig. 7.1 (a) XRD patterns of LSGM powder (black), an LSGM single crystal (blue) and an LSGM single crystal with an additional 50 nm thin LSC film on top (red). (b) XRD reciprocal space map showing the reflection of the [-103] plane of both the LSGM substrate and 50 nm thin LSC film.

LSGM single crystals were examined in Bragg-Brentano Θ - 2Θ geometry using parallel-beam optics without and with additional 50 nm LSC thin film layer on top (sample for Hebb-Wagner polarization experiment). The diffraction patterns over the measured 2Θ range are shown in Fig. 7.1a. Furthermore, a diffraction pattern of a powderized LSGM single crystal (black) measured with focusing optics is shown in the figure. All peaks were indexed with respect to the pseudo-cubic structure of both materials and no sign of impurities was found. However, LSGM shows an orthogonal and LSC a rhombohedral distortion at room temperature. The orthorhombic structure of LSGM is clearly observed in the powder diffraction pattern by a peak at $38.2^\circ 2\Theta$ and splitting of other indexed peaks. The refined values of the calculated unit cell are $a = 7.782 \text{ \AA}$, $b = 5.493 \text{ \AA}$, $c = 5.533 \text{ \AA}$ and close to the values reported in Ref. ¹⁷¹ measured on $\text{La}_{0.95}\text{Sr}_{0.05}\text{Ga}_{0.9}\text{Mg}_{0.1}\text{O}_{3-6}$.

The LSC thin film deposited on the LSGM single crystal showed only [00l] peaks in the measured 2Θ range and the epitaxial growth was further analyzed by a reciprocal space map, see Fig. 7.1b. The reciprocal space map shows a high intensity spot representing the [-103] lattice plane of LSGM and two horizontally shifted satellite spots indicating different domains in the single crystal. This

was also found in $\text{La}_{0.95}\text{Sr}_{0.05}\text{Ga}_{0.9}\text{Mg}_{0.1}\text{O}_{3-\delta}$ single crystals^{166, 178}. The [-103] lattice plane of LSC is observed directly above the high intensity LSGM spot. Thus, it can be concluded that the in-plane lattice components match well. A pseudo-cubic in-plane lattice parameter of $a_{\text{pc}, \parallel} = 3.87 \pm 0.01 \text{ \AA}$ for both materials and an out-of-plane lattice parameter of $a_{\text{pc LSGM}, \perp} = 3.90 \pm 0.01 \text{ \AA}$ and $a_{\text{pc LSC}, \perp} = 3.80 \pm 0.01 \text{ \AA}$ results for LSGM and LSC, respectively. Hence, a tensile in-plane lattice strain of 1.1 % can be determined based on the lattice mismatch between the strained LSC thin film and a relaxed LSC thin film ($a_{\text{pc}} = 3.838 \text{ \AA}^{120}$) grown on YSZ. Although the strain induced in the electrode thin film is of minor importance here, deposition of perovskite-type materials on top of LSGM single crystals might be a very attractive strategy to investigate the influence of strain in thin film electrodes on the oxygen exchange and transport kinetics by means of electrical measurements (e.g. impedance spectroscopy).

7.3.2 Equivalent circuit model

The general equivalent circuit model of a MIEC introduced by J. Jamnik and J. Maier⁶⁷, see Fig. 7.2, consist of an ionic and an electronic rail with a capacitive displacement rail in parallel to the entire circuit ($C_{\text{MIEC, dielec}} = \text{geometrical capacitance of the MIEC}$). This circuit represents a homogenous MIEC under the assumption of local electroneutrality. The charge carrier flux in the bulk of the MIEC is determined by differential resistive elements along the ionic and electronic resistive rails, which are coupled by the chemical capacitance. The chemical capacitance describes the ability of a material to store chemical energy by undergoing stoichiometric changes. The ionic and electronic resistive rails are terminated on both sides by an RC-element to account for electrochemical reactions and charge transfer taking place at interfaces. Certainly, electrode reactions are very complex and may not necessarily be represented by this simplified terminal. However, for Pt electrodes on ceria, this approach has already been shown to fit experimental data well and also in our study any further elements would lead to overparameterization¹⁷⁵.

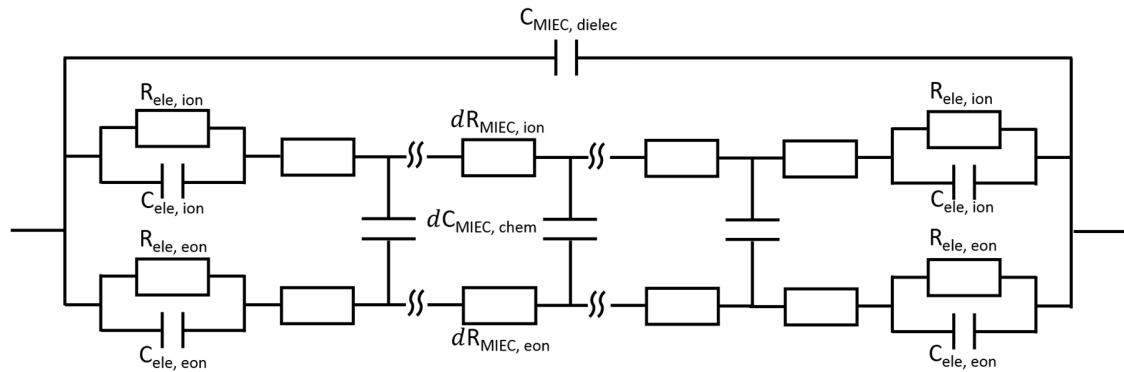


Fig. 7.2 General equivalent circuit of a mixed ionic electronic conductor between two electrodes. In the data analysis software this circuit (except $C_{MIEC, dielec}$) is termed DX Type 19 - Jamnik-Maier-Lai-Lee.

Since, Pt electrodes were deposited on both sides of the LSGM single crystal, a symmetrical electrochemical cell was obtained and in chapter 7.3.3 (AC experiments) only one half of the equivalent circuit from Fig. 7.2 is shown to highlight the relevant fit elements. Subscripts $_{ele}$ and $_{MIEC}$ are then specified by the given materials Pt and LSGM.

7.3.3 Temperature dependence of the impedance spectra shape

The temperature dependency of the impedance response was measured between 180 °C and 800 °C in synthetic air (mixture of 21 % O₂ in N₂). Representative Nyquist plots starting from high temperatures and going to low temperatures in steps of ~50 °C are shown in Fig. 7.3 and 7.4. The experimental data were fitted to the equivalent circuits shown below each plot. Fit elements and current paths of the entire circuit that were excluded in the particular temperature regime are indicated by dashed lines. An excellent agreement between the presented equivalent circuit fitting model (solid line) and measured data (points) is found over the whole temperature range.

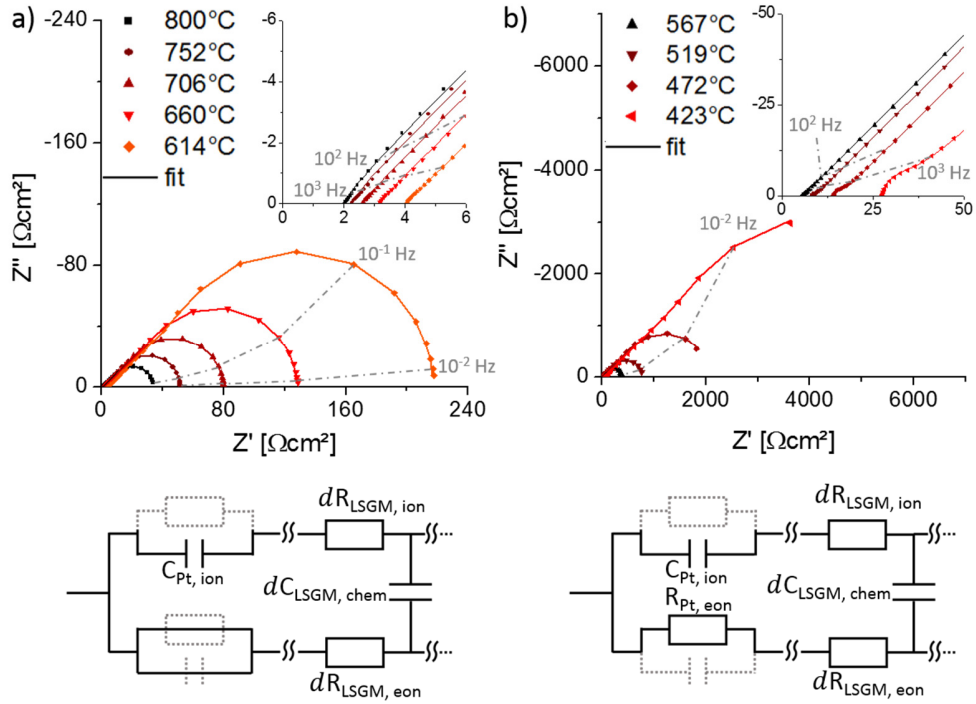


Fig. 7.3 Nyquist plots of a Pt|LSGM|Pt sample measured at (a) 800 – 614 °C and (b) 567 – 423 °C in synthetic air. The respective equivalent circuits used to fit the experimental data are shown below the Nyquist plots. Grey dotted current paths and/or elements were omitted for the fit.

At high temperatures (800 °C – 614 °C) the impedance spectra are characterized by a high frequency intercept and a semi-tear drop shaped feature, a Warburg-type impedance. After subtracting the serial wire resistance, the high frequency intercept (R_{hf}) corresponds to the total conductivity of the LSGM bulk, i.e. the electronic conductivity in parallel to the ionic conductivity, since the low impedance of the electrode capacitance ($C_{Pt, ion}$) allows ion movement at these frequencies. At lower frequencies, ion motion in LSGM becomes more and more hindered since the Pt electrodes essentially block the oxygen exchange and thus the ions. Consequently, a Warburg-type impedance is obtained. This can be reflected in the equivalent circuit, by an infinitely large $R_{Pt, ion}$. It is shown in Ref. ^{67, 175} that in such a case with $C_{ele, ion} \ll C_{MIEC, chem}$ the impedance of the entire circuit (except $C_{MIEC, dielec}$) is given by

$$Z = R_{hf} + R_W \frac{\tanh((i\omega T)^p)}{(i\omega T)^p}. \quad (7.1)$$

The second term corresponds to the analytical expression of a finite Warburg impedance with resistance R_W and fit parameters T and p . An ideal Warburg element is obtained for $p = 0.5$, which

then also allows to directly relate the fit parameter T with the sample thickness L to the one-dimensional chemical diffusion coefficient D_{chem}

$$T = \frac{\left(\frac{L}{2}\right)^2}{D_{chem}} = \frac{C_{MIEC, chem} (R_{MIEC, eon} + R_{MIEC, ion})}{4}. \quad (7.2)$$

Chemical diffusion coefficients at different temperatures and oxygen partial pressures are calculated by this relationship at the end of this chapter. Indeed, the serial connection of a finite Warburg element and a resistor also fits our data, instead of the generalized impedance circuit used in the entire study (here without $R_{Pt, ion}$, $C_{Pt, eon}$ and $R_{Pt, eon}$).

In the temperature regime 567 °C – 423 °C a new semicircular shaped feature ($10^3 - 10^5$ Hz) arises between the high frequency intercept and the Warburg-type impedance, see inset Fig. 7.3b. The impedance of this semicircle increases continuously with decreasing temperature. This feature cannot be explained by the equivalent circuit elements of the MIEC bulk. Thus, it has to be associated with a change of the terminals, i.e. the electrode impedance. Analysis of the impedance spectra by the entire equivalent circuit model of Fig. 7.2 revealed that only an additional electrode resistance in the electronic rail can describe the observed phenomena (cf. Fig. 7.3b bottom). This resistance may either refer to the LSGM||Pt or to the Pt||Pt-contact sheet interface. One reasonable explanation would be the formation of PtO_x at the Pt||LSGM interface; PtO_x was reported to decompose at higher temperatures^{179, 180}. In any case, the equivalent circuit fits the measured data very well over the entire frequency regime and allows to extract also $R_{Pt, eon}$.

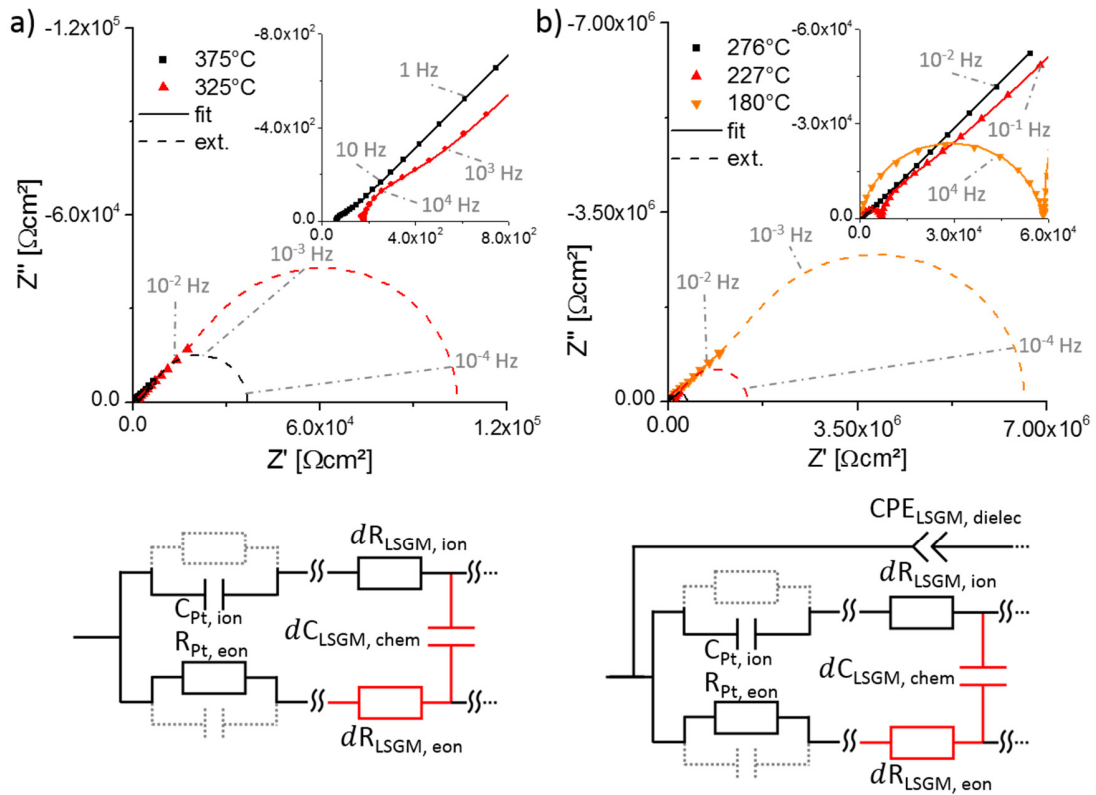


Fig. 7.4 Nyquist plots of a Pt|LSGM|Pt sample measured at (a) 375 – 325 °C and (b) 276 – 180 °C in synthetic air. The respective equivalent circuits used to fit the experimental data are shown below the Nyquist plots. Grey dotted current paths and elements were omitted for the fit. Red highlighted equivalent circuit elements indicate that these quantities could only be determined with limited accuracy.

Below 400 °C, Fig. 7.4, the semi-tear drop shaped low-frequency feature could no longer be fully resolved within a reasonable time (> 1/2 hour for a single impedance spectra). Therefore only the first part, the Warburg-type diffusion slope, could be used to fit the experimental data and the quantities $R_{\text{LSGM}, \text{eon}}$ and $C_{\text{LSGM}, \text{eon}}$ were determined with less accuracy (highlighted in red in the equivalent circuit). The relative fitting error of these two parameters strongly increased from ~4 % at 375 °C to ~120 % at 180 °C. The latter error is still surprisingly “low” since at 180 °C only about 1/7th of the real part of the Warburg-type element is measured. Extrapolations of the fitted impedance according to the equivalent circuit models (dashed lines) are shown in Fig. 7.4. At low temperatures (<276 °C) the high frequency intercept changes into a high frequency semicircle, see inset. Its peak frequency $\omega = (RC)^{-1}$ is determined by the parallel elements $R_{\text{LSGM}, \text{eon}} || R_{\text{LSGM}, \text{ion}} || C_{\text{LSGM}, \text{dielec}} \approx R_{\text{LSGM}, \text{ion}} || C_{\text{LSGM}, \text{dielec}}$ and shifts into the measured frequency range because of the strong temperature dependence of $R_{\text{LSGM}, \text{ion}}$. A constant phase element instead of the capacitance $C_{\text{LSGM}, \text{dielec}}$ is used to fit the data properly. Its impedance is given by

$$Z_{CPE} = \frac{1}{T(i\omega)^p} \quad (7.3)$$

with the fitting parameters T and p . The capacitance was calculated by the relationship¹⁸¹

$$C = (R^{1-p} \cdot T)^{1/p}. \quad (7.4)$$

For all measurements p -values of ~ 0.88 were obtained for the $CPE_{LSGM, dielec}$ element. In this manner, all spectra could be quantified by one and the same generalized equivalent circuit model and four important materials parameters could be obtained: ionic conductivity (σ_{ion}), electronic conductivity (σ_{eon}), chemical capacitance (C_{chem}) and electronic interfacial resistance ($R_{Pt, eon}$). The other fit parameters ($C_{LSGM, dielec}$, $C_{Pt, ion}$) were also determined but are not discussed in detail.

7.3.4 Temperature dependence of the materials parameters

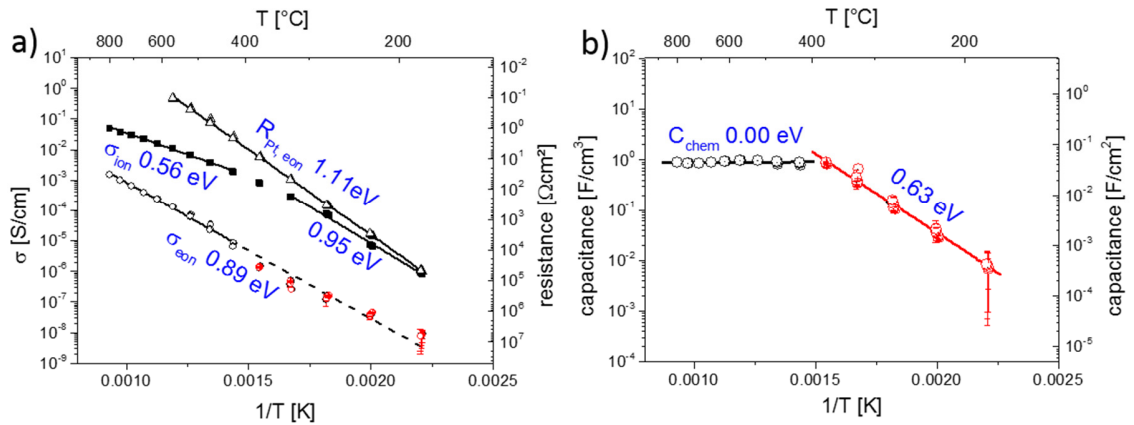


Fig. 7.5 Arrhenius plots of the (a) resistive and (b) capacitive quantities of a Pt|LSGM|Pt sample measured in synthetic air. Red data points highlight measurements of limited accuracy (cf. Fig. 7.4 and error bars). Activation energies determined from the give data are also shown.

Arrhenius plots of the resistances and the LSGM chemical capacitance extracted from three temperature series (180 °C → 800 °C → 180 °C → 800 °C) are shown in Fig. 7.5 together with their activation energies. Values of all three series are in excellent agreement. Also two spectra measured for each temperature in each series with 30 minutes time difference did not show any time dependencies or hysteresis effects. Hence, it is supposed that all values in Fig. 7.5 are equilibrated values. The ionic conductivity σ_{ion} of LSGM does not exhibit a simple linear Arrhenius-type behavior. A remarkable curvature is found with lower activation energies (0.56 eV) at higher temperatures. A changing activation energy was already observed for polycrystalline LSGM pellets

of the same and other compositions as well as for other highly doped ionic conductors such as YSZ and GDC. It is generally explained by defect-dopant interactions such as trapping of isolated oxygen vacancies or formation of ordered-vacancy clusters at low temperatures. K. Huang et al.¹⁸² experimentally found a strong correlation between the low temperature activation energy and the Mg concentration in $\text{La}_{1-x}\text{Sr}_x\text{Ga}_{1-y}\text{Mg}_y\text{O}_{3-\delta}$ (and only minor influence of the Sr concentration). This is consistent with theoretical calculations of M.S. Islam¹⁸³ who determined a high binding energy for the $\text{Mg}_{\text{Ga}}^{\text{I}} - \text{V}_{\text{O}}^{\cdot\cdot}$ cluster compared to $\text{Sr}_{\text{La}}^{\text{I}} - \text{V}_{\text{O}}^{\cdot\cdot}$. The absolute values obtained for the ionic conductivity of our LSGM single crystal are in excellent agreement with measurements of the total conductivity on polycrystalline pellets at temperatures of 595 – 800 °C¹⁸². Hence, the grain to grain boundary conductivity ratio in the latter case has to be smaller than the thickness ratio of grain to grain boundary¹⁸⁴.

For the electronic conductivity an activation energy of 0.89 eV was determined between 423 – 800 °C. In chapter 7.3.5 it is shown that holes are responsible for this electronic conductivity. The activation energy is comparable to measurements of the temperature dependent p-type conductivity by ion-blocking DC techniques (cf. chapter 7.3.6) on $\text{La}_{0.9}\text{Sr}_{0.1}\text{GaO}_{3-\delta}$ ¹⁸⁵ (0.86 eV) and $\text{La}_{0.9}\text{Sr}_{0.1}\text{Ga}_{0.8}\text{Mg}_{0.2}\text{O}_{3-\delta}$ ¹⁶⁴ (1.12 eV). However, please note that the electronic conductivity measured here is indeed a pure bulk property, while from measurements in literature, performed on polycrystals, only effective electronic conductivities are available. This makes a quantitative comparison difficult. Interestingly, literature data on the p-type conductivity show very pronounced differences (several orders of magnitude^{164, 185-187}) for different Sr and Mg doping levels. This is not expected from a simple defect chemical model (see below) and might be, at least partly, caused by grain boundary effects.

The electronic conductivities determined for lower temperatures (< 400 °C) are less accurate (see above) and analyzing only those values suggest a lower activation energy. However, extrapolating the accurate temperature values to low temperatures showed very reasonable agreement with measured data. Hence, it is supposed that the entire temperature range shows the same activation energy ca. 0.9 eV. The electronic transference number $t_{\text{eon}} (= \sigma_{\text{eon}}/(\sigma_{\text{eon}} + \sigma_{\text{ion}}))$ has a minimum (0.001) at 320 °C and increases at higher temperatures to 0.03 at 800 °C in synthetic air. $R_{\text{pt, eon}}$, finally, shows an ideal linear Arrhenius-type behavior with an activation energy of 1.11 eV.

The temperature dependency of the chemical capacitance exhibits two well separated regimes. At low temperatures (below 400 °C) it increases with an activation energy of 0.63 eV. Above this temperature it is essentially constant. The chemical capacitance of LSGM given is given by¹⁸⁸

$$C_{chem} = 4e^2V \left(\frac{\partial \mu_o}{\partial c_o} \right)^{-1} = 4e^2V \left(\frac{\partial}{\partial c_o} (-\mu_V + 2z_{e_{on}}\mu_{e_{on}}) \right)^{-1} \quad (7.5)$$

with e being the elementary charge, V the sample volume, c_o the oxygen concentration and the chemical potentials μ_o , μ_V , $\mu_{e_{on}}$ of oxygen, vacancies and main electronic charge carriers (with the electronic charge number z), respectively. Usually, the chemical capacitance is dominated by the minority charge carrier. Since for LSGM, $R_{ion} < R_{e_{on}}$ and the ionic mobility is generally much lower than the electronic mobility, it can be concluded that the electronic charge carriers (here holes) are the minority species. In the dilute limit ($C_{chem} = 4e^2Vc_h/kT$) with hole concentration c_h results from eq. 7.5. Accordingly, C_{chem} and $\sigma_{e_{on}}$ should exhibit similar temperature dependences, with the conductivity additionally including a temperature dependence of the mobility. However, while for the electronic conductivity high and low temperature activation energy are in reasonable agreement, C_{chem} exhibits a drastic change around 400 °C. Agreement of high and low temperature values of $\sigma_{e_{on}}$ excludes an artifact of an inaccurate fit that causes the surprising C_{chem} - T behavior. It can therefore be proposed that additional defect chemical effects come into play. A large number of trapped holes might be present, which increases C_{chem} but does not contribute to $\sigma_{e_{on}}$. But also by including traps into the analysis of eq. 7.5 it was not possible to explain the activation energy change of C_{chem} and thus further unknown factors seem to affect the chemical capacitance. Accordingly, the absolute hole concentrations could not be determined from C_{chem} . The quantities $C_{Pt, ion}$ ($6.02 \pm 0.32 \cdot 10^{-5} \text{F/cm}^2$) and $C_{LSGM, dielec}$ ($1.13 \pm 0.01 \cdot 10^{-10} \text{F/cm}^2$) are not plotted but remained constant over the measureable temperature regime.

7.3.5 Oxygen partial pressure dependence

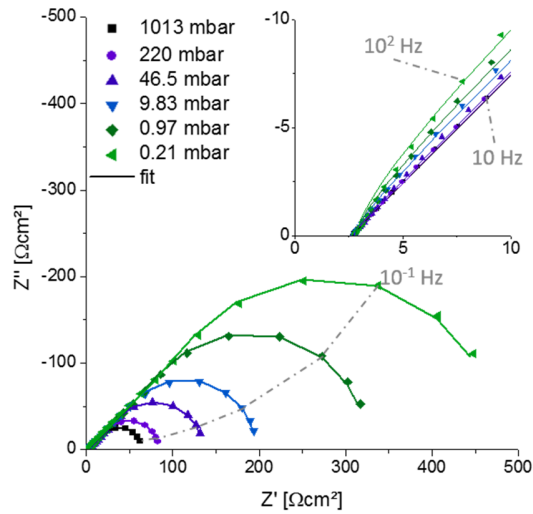


Fig. 7.6 Nyquist plots of a Pt/LSGM/Pt sample measured at 700 °C and different oxygen partial pressures. Experimental data were fitted to the equivalent circuit shown in Fig. 7.3a.

The oxygen partial pressure (p_{O_2}) was varied between 0.21 and 1013 mbar and impedance spectra were measured at different temperatures (550 °C – 800 °C). Representative Nyquist plots at 700 °C are shown in Fig. 7.6. A clear dependence of the spectra on p_{O_2} without any time drift is found and indicates equilibration of LSGM to each novel p_{O_2} prior to the impedance measurement. The experimental data were fitted to the equivalent circuit in Fig 3a. $R_{Pt, eon}$ was not required for these measurements and an excellent agreement between data and fit is found for all oxygen partial pressures. In accordance with the interpretation given above the sum of the high frequency intercept and the Warburg resistance corresponds to the electronic transport resistance of LSGM. The total conductivity of LSGM is represented by the high frequency intercept and dominated by the ionic transport. The high frequency intercept ($\sim 2.7 \Omega\text{cm}^2$ for all p_{O_2}) and thus σ_{ion} is essentially p_{O_2} independent. On the other hand, the size of the Warburg-type impedance increases significantly with decreasing p_{O_2} . Accordingly, the electronic conductivity of LSGM shows a significant dependence on the oxygen partial pressure. This is quantitatively shown in Fig 7a.

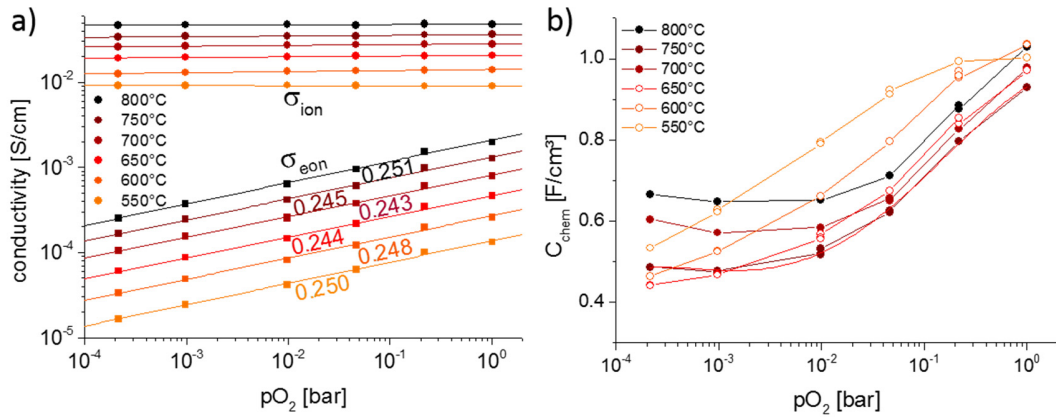


Fig. 7.7 Oxygen partial pressure dependence of the (a) conductivities and (b) the chemical capacitance of a Pt|LSGM|Pt sample between 550 – 800 °C. Power laws according to $\sigma_{\text{eon}} \sim (p\text{O}_2)^m$ are indicated in (a) together with their linear fit (solid lines). The solid lines in (b) only represent a guide to the eye.

The slopes found for the electronic conductivity in such $\log \sigma - \log p\text{O}_2$ diagrams are very close to 0.25 for all temperatures. Hence, the LSGM single crystals follow almost ideally the defect chemical model given by the following defect equilibrium:



$$[h^{\cdot}] = p_{\text{O}_2}^{1/4} \cdot \sqrt{\frac{K_{\text{O}} \cdot [V_{\text{O}}^{\bullet\bullet}]}{[\text{O}_{\text{O}}^{\times}]}} \quad (7.7)$$

The oxygen vacancy concentration $[V_{\text{O}}^{\bullet\bullet}]$ is essentially fixed by the dopant concentration in accordance with the $p\text{O}_2$ independent ionic conductivity and a slope of 0.25 should thus result. As a consequence, the ionic transference number $t_{\text{ion}} (= \sigma_{\text{ion}} / (\sigma_{\text{eon}} + \sigma_{\text{ion}}))$ increases for lower oxygen partial pressures and for lower temperatures. Electronic conductivities are often determined by the Hebb-Wagner method (see chapter 7.3.6) and this also reveals information on the $p\text{O}_2$ dependence of σ_{eon} (or, more precisely, its dependence on the oxygen chemical potential). The beauty of the impedance approach used here, however, is the fact that very accurate absolute conductivity values can be determined for each $p\text{O}_2$. This allows very precise analysis of slopes in $\log \sigma - \log p\text{O}_2$ plots. In Hebb-Wagner measurements absolute electronic conductivities are generally obtained from a fit of an idealized model to a complete I - V curve (see below) and small deviations from ideality are easily missed. Alternatively, absolute values can be obtained from slopes of I - V curves, which is usually again a less accurate approach.

Fig. 7.7b displays the C_{chem} dependency on the oxygen partial pressure in a linear plot. A very clear general trend is not found. However, it can be excluded that only free electron holes determine the chemical capacitance, since the slope of C_{chem} does not match the slope of σ_{eon} . This again supports the assumption of a complex interplay of defect chemical effects in C_{chem} already discussed above. The oxygen chemical diffusion coefficient of LSGM D_{chem} was determined according to equation 7.2, see Fig. 7.8. This reveals a $p\text{O}_2$ dependence and in particular a surprising temperature dependence. But a simple interpretation of the latter, especially of its temperature independent part, is not possible due to the complex nature of C_{chem} . Still D_{chem} values are in accordance with our assumption of equilibrated LSGM samples at all temperatures.

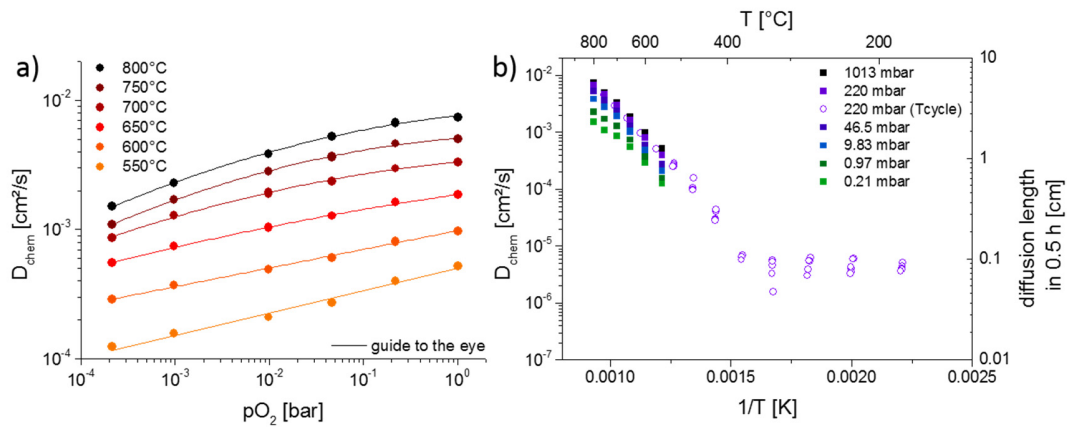


Fig. 7.8 (a) Oxygen partial pressure and (b) temperature dependence of the oxygen chemical diffusion coefficient of a LSGM single crystal. Diffusing lengths calculated from $(D_{\text{chem}} \cdot t)^{1/2}$, $t = 0.5$ h, are also indicated.

7.3.6 Hebb-Wagner type polarization

For reasons of comparison the p-type and n-type conductivities were also determined in a Hebb-Wagner type polarization experiment. This method is more frequently used than the AC approach shown above and also all literature data of σ_{eon} in LSGM available so far were obtained in that manner. For these measurements the electrode arrangement has to be changed. A 50 nm thin LSC film was deposited on one side of the LSGM single crystal and a Pt mesh (35 μm mesh size) was sputtered on top of the film to avoid in-plane sheet resistances in the LSC film. LSC is expected to act as an almost reversible electrode for oxygen exchange¹²⁰. A 400 nm thin Pt electrode (as used in AC experiments) on the other side of the specimen served as ion blocking electrode. The experiment was performed at 600 °C and 0.21 bar $p\text{O}_2$. A bias voltage between -0.1 and 1.7 V (100 mV step size) was applied to the reversible LSC electrode relative to the blocking electrode. The current-voltage characteristics of the cell is shown in Fig. 7.9a (currents measured 10 minutes after each voltage change).

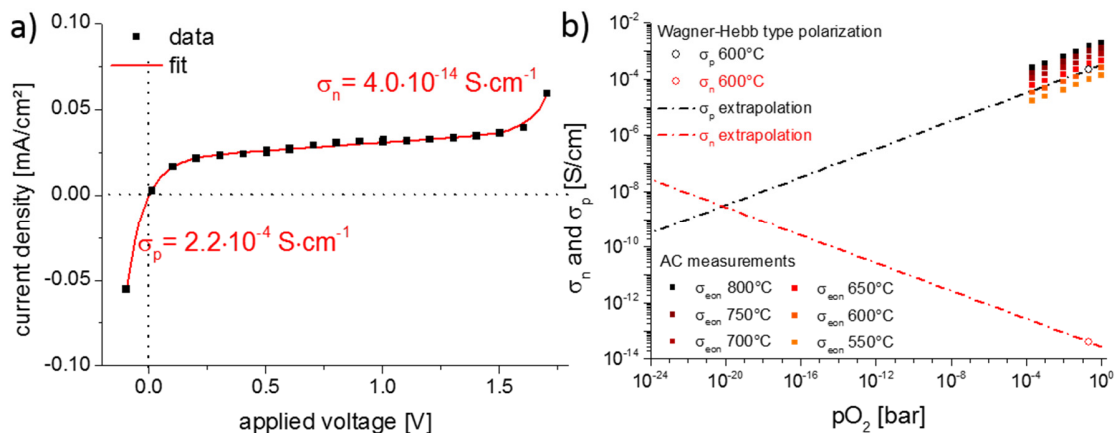


Fig. 7.9 (a) Current – voltage characteristic of a Pt/LSGM/LSC sample at 600 °C. The oxygen partial pressure at the reversible electrode (LSC) was set to 0.21 bar $p\text{O}_2$. The p- and n-type conductivities for zero voltage, determined by fitting the experimental data to eq. 7.9, are highlighted red. (b) Brouwer type diagram of the p-type and n-type conductivity, including extrapolated values, measured by Hebb-Wagner type polarization and the total electronic conductivity measured in the AC experiment.

Small negative voltages lead to a strong current increase. For positive voltages the current increase becomes rather small except for $U > 1.5$ V. The relation between current and voltage in ion-blocking polarization experiment was first described by Hebb and Wagner in Ref.^{189, 190}.

Supposing exact validity of eq. 7.7 and band-band equilibrium $[e^{\cdot}]\cdot[h^{\cdot}] = K_e$ as well as $[e^{\cdot}]\cdot[h^{\cdot}] \ll [V_O^{\cdot}]$ for all chemical potentials, it is given by

$$I = \frac{RT}{F} \cdot \frac{A}{L} \left(\sigma_p \left[1 - e^{-\frac{UF}{R_g T}} \right] + \sigma_n \left[e^{\frac{UF}{R_g T}} - 1 \right] \right) \quad (7.8)$$

with R_g being the gas constant, T the temperature, F the Faraday constant, A and L the sample area and thickness, respectively. The hole conductivity σ_p and the electron conductivity σ_n at the reference partial pressure (0.21 bar p_{O_2} , in this case) can be determined by fitting the measured data to equation 7.8. However, for very different σ_p and σ_n Eq. 7.8 should lead to an almost constant current in a large voltage range. This is in contrast to our data with a continuous slight increase between 0.3 and 1.3 V. Supposedly, an ionic leakage current is the reason for this non-ideality, since the side faces of the LSGM single crystal were not sealed and therefore allowed oxygen exchange. Similar non-idealities can also be found in literature^{164, 185, 186, 191}.

To take account of this leakage current an additional linear term with slope α is introduced into eq. 7.8 leading to

$$I = \frac{RT}{F} \cdot \frac{A}{L} \left(\sigma_p \left[1 - e^{-\frac{UF}{R_g T}} \right] + \sigma_n \left[e^{\frac{UF}{R_g T}} - 1 \right] \right) + \alpha U \quad (7.9)$$

and the fit to the measured data set is shown in Fig. 7.9a. The additional ohmic resistance α^{-1} determined from the fit is $2.7 \pm 0.1 \cdot 10^4 \Omega$. The excellent fit suggests indeed an ohmic resistor determining this leakage current despite supposed serial oxygen incorporation at Pt. Based on the results obtained in chapter 3.3, AC experiments although using the same ion blocking Pt electrodes seem to be unaffected. This might be because of the strong polarization in DC (1.7 V) compared to the AC (0.01 V) experiments. This will lead to a high μ_O gradient between gas phase and the LSGM close to the blocking Pt electrode and a higher electron concentration at the blocking electrode. Hence, there is a much larger driving force and defect concentration, which eases the oxygen incorporation during the DC experiment. Then, the incorporated oxygen is transported to the reversible electrode and a leakage current is generated. An extension of the oxygen incorporation area from the triple phase boundary of microstructured Pt electrodes to parts of the free YSZ surface was also found under strong cathodic bias in Ref. ³⁶.

A p-type conductivity of $2.2 \pm 0.1 \cdot 10^{-4} \text{ S}\cdot\text{cm}^{-1}$ at 0.21 bar $p\text{O}_2$ is determined and this is in very good agreement with the total electronic conductivity (σ_{eon}) measured during $p\text{O}_2$ variation ($1.9 \pm 0.1 \cdot 10^{-4} \text{ S}\cdot\text{cm}^{-1}$) and temperature cycling ($2.0 \pm 0.1 \cdot 10^{-4} \text{ S}\cdot\text{cm}^{-1}$) by the impedance approach shown above. The n-type conductivity of $4.0 \pm 0.2 \cdot 10^{-14} \text{ S}\cdot\text{cm}^{-1}$ obtained in this experiment is not accessible in the AC experiment. It may best be compared to extrapolated values from Ref. ¹⁸⁶, $3.1 \cdot 10^{-13} \text{ S}\cdot\text{cm}^{-1}$ at 600 °C in 1.013 bar $p\text{O}_2$. There, the n-type conductivity was also measured by an ion-blocking polarization technique but between 967 – 767 °C on polycrystalline $\text{La}_{0.95}\text{Sr}_{0.05}\text{GaO}_{3-\delta}$ samples. The results of the electronic conductivity of LSGM are again summarized in a kind of Brouwer diagram in Fig. 7.9b. It includes precisely measured σ_{eon} data from AC experiments, the two fit values of hole (σ_p) and electron (σ_n) conductivity at 600 °C in syn. air and lines representing conductivities according to the Hebb-Wagner measurements for ideal slopes of 0.25. At 600 °C the hole conductivity equals the electron conductivity at an oxygen partial pressure of approx. 10^{-20} bar $p\text{O}_2$ with $\sigma_n = \sigma_p \approx 3 \cdot 10^{-9} \text{ S}\cdot\text{cm}^{-1}$.

7.4 Conclusions

An AC impedance study on $\text{La}_{0.95}\text{Sr}_{0.05}\text{Ga}_{0.95}\text{Mg}_{0.05}\text{O}_{3-\delta}$ (LSGM) single crystals with ion blocking electrodes was carried out and the impedance spectra were quantitatively evaluated over the entire measured temperature and $p\text{O}_2$ range by the general equivalent circuit model for mixed conductors. The excellent agreement between fit and experimental data allowed determination of the ionic and electronic conductivity, the chemical capacitance and the oxygen chemical diffusion coefficient from a single impedance spectrum. Activation energies for the electronic (0.89 eV) and ionic transport (0.95 eV at low and 0.56 eV at high temperatures) were calculated. Partial pressure as well as temperature dependence of the chemical capacitance suggests existence of trapped electronic defects and further defect chemical complexities. The p-type conductivity on the other hand was almost exactly proportional to $p_{\text{O}_2}^{1/4}$ in the range of 10^{-4} to 1 bar oxygen partial pressure and thus shows impressive agreement with ideal dilute defect chemical models. Hebb-Wagner type DC polarization experiments yielded a p- and n-type conductivity of $2.2 \pm 0.1 \cdot 10^{-4} \text{ S}\cdot\text{cm}^{-1}$ and $4.0 \pm 0.2 \cdot 10^{-14} \text{ S}\cdot\text{cm}^{-1}$ respectively at 600 °C and 0.21 bar $p\text{O}_2$. DC results are in excellent agreement with those determined by the AC experiments under the same conditions. This supports the supposed reliability of the AC method to precisely determine electronic conductivities.

8. Summary

$\text{La}_{0.6}\text{Sr}_{0.4}\text{CoO}_{3-\delta}$ (LSC) model thin films (20 – 200 nm) were deposited by pulsed laser deposition (PLD) on (100) oriented yttria stabilized zirconia (YSZ) single crystals. Depending of the substrate temperature, chemistry of the substrate and ambient oxygen partial pressure different LSC microstructures could be tailored. Columnar grain growth was determined independent of the preparation conditions. Lower substrate temperatures (450 °C) yielded polycrystalline LSC thin films while at higher temperatures (600 °C) the grain size increased and lead to thin films with preferred crystal orientation in (100) and (110) direction. Higher oxygen partial pressures ($4 \cdot 10^{-1}$ mbar) lead to an increased porosity, while dense thin films were obtained at lower oxygen partial pressures ($4 \cdot 10^{-2}$ mbar). Nonetheless, as-prepared thin films suffered from crack formation during cooling, caused by the difference of the thermal expansion coefficients between LSC and YSZ. Implementation of a ~ 50 nm thin $\text{Ce}_{0.8}\text{Gd}_{0.2}\text{O}_{2-\delta}$ buffer layer between electrolyte and electrode prevented crack formation and allowed deposition of well-defined completely dense LSC thin film model electrodes. All three types of films (porous, dense with some cracks, completely dense) were investigated in this thesis.

First studies on the oxygen reduction reaction (ORR) kinetics of LSC thin films were carried out on microelectrodes (200 μm diameter) fabricated by photolithography. Impedance spectroscopy was used to deconvolute different impedance contribution of the investigated LSC/YSZ system, thus allowing to extract quantities such as the electrolyte resistance, oxygen surface exchange resistance and chemical capacitance. Special attention was given to the oxygen reduction reaction (ORR) kinetics, since it determines the polarization resistance of LSC thin films and is crucial for a successful integration of LSC in solid oxide fuel cells (SOFCs). Degradation of the electrochemical performance was correlated to Sr surface segregation, first monitored by secondary ion mass spectrometry (SIMS). For further investigations an innovative approach for a quantitative determination of the LSC surface stoichiometry was developed. LSC thin films were treated with different etching solutions (H_2O , HCl), followed by on-line analysis of the derived eluates using inductively coupled plasma – optical emission spectrometry (ICP-OES). This approach has the advantage of a simple quantification by standard calibration in opposite to conventionally applied methods for the analysis of solids (SIMS, X-ray photoelectron spectroscopy (XPS)). Further, a differentiation between water soluble and acid soluble parts of near surface regions in thin films was enabled.

A water-soluble Sr rich surface layer was found for dense thin films freshly deposited at 450 °C. It corresponds to ~1.2 atomic layers of SrO covering the electrode surface. Quantification by ICP-OES allowed to correlate the Sr amount and the oxygen surface exchange resistance ($R_{\text{surface exchange}}$) for dense and porous thin films. Thus, the influence of microporosity on the $R_{\text{surface exchange}}$ could be quantified by combining impedance spectroscopy measurements and ICP-OES. In another study⁴⁹ the same technique was successfully applied on thicker (~15 μm) screen-printed porous LSCF electrodes. There, the true surface area was calculated by a three-dimensional tomography analysis using focused ion beam–scanning electron microscopy and the Sr surface amount, 1.04 ± 0.22 atomic layers of SrO, was very similar to that found on thin films. Since the Sr-rich surface of LSC was proven to be water-soluble, all further investigations were carried out on macroscopic ($5 \times 5 \text{ mm}^2$) as-deposited thin films to avoid any contact of the surface with solvents needed for photolithographic preparation of microelectrodes.

Further improvements in sensitivity and reproducibility were achieved by ICP-MS, a PTFE etching compartment and correction of spectral interference by internal standards. Thus the surface and near-surface composition of dense LSC thin films that could previously be analyzed only with limited accuracy, especially for La and Co, became fully accessible. Equality of true and projected surface area facilitated normalization of the results and allowed a comparison to conventionally applied surface sensitive analysis techniques for solids such as SIMS, XPS and low energy ion scattering (LEIS).

Surface sensitive measurements on LSC thin films performed by LEIS and in-situ ICP-MS thin film electrodes agreed qualitatively and quantitatively and provided a consistent picture of the surface termination composition and cation diffusion kinetics. For as-deposited dense LSC thin films a water-soluble Sr-rich and Co-poor termination layer was confirmed. While the Co depletion was only observed in the termination layer, Sr was enriched in the first 3 nm of LSC. The surface layer was removed by treating the sample in ultrapure water, but ca. 1 monolayer of SrO repeatedly formed again whenever the sample was annealed at or above 550 °C for 1 h. A Sr depletion in subsurface regions was not found, thus very fast Sr diffusion with only slight depletion in larger parts of the film were concluded. These experiments indicate that formation of the Sr-rich surface layer is in fact an equilibrium property of LSC and that Sr diffusion does not limit its formation kinetics under these conditions. Impedance measurements at 400 °C revealed the detrimental effect of this surface layer on the oxygen surface exchange and suggest that higher Co concentration in the termination layer facilitate the oxygen exchange reaction.

For an even more detailed insight into the impact of surface composition on the ORR, a novel approach was developed. Instead of the most common chemical post-analysis of degraded electrode thin films, the LSC surface was deliberately modified by depositing defined amounts of its cation constituents (Sr-, Co and La-oxides). Electrochemical characterization was performed during the deposition process by in-situ impedance spectroscopy measurements inside the pulsed laser deposition chamber (IPLD). This approach has the advantage that any alteration of the electrode surface between preparation and investigation can be avoided. Quantification of the surface modification was performed by means of calibration curves using inductively coupled plasma-mass spectrometry (ICP-MS). It was shown that a single laser pulse on a SrO target leads to deposition of only 4 % of a SrO monolayer (13 pmol Sr) but still this increases the initial $R_{\text{surf exch}}$ by about 42 %. Three pulses (13% of a SrO monolayer) almost doubled $R_{\text{surf exch}}$. It is therefore concluded that only a few sites of as-prepared LSC films are highly active for oxygen exchange and that decorating Sr cations do not randomly cover the surface but specifically deactivate those active sites. Moreover, Co-oxide decoration improved the ORR kinetics even of vastly degraded samples and gave clear evidence that the accessibility of Co at the surface strongly improves the ORR kinetics. The novel combination of PLD and IS may not only be applicable to many other electrode surfaces but can also be highly valuable for directly monitoring the electrochemical properties of a growing MIEC thin film even at its earliest stages. Hence, insights into the film thickness dependence of defect chemistry and ORR activity can be gained at an accuracy level not accessible otherwise.

An additional cathode material, $\text{La}_{0.6}\text{Ba}_{0.4}\text{CoO}_{3-\delta}$ (LBC), was investigated as an alternative to LSC and an extraordinary high catalytic activity for the ORR was found in the temperature range relevant for intermediate temperature SOFC applications. In a comparative study with $\text{La}_{0.6}\text{Sr}_{0.4}\text{CoO}_{3-\delta}$ (LSC) thin films it could be shown that the very low surface exchange resistance for LSC ($\sim 0.6 \Omega\text{cm}^2$ at 604 °C, $\sim 17 \Omega\text{cm}^2$ at 463 °C) is even excelled by LBC ($\sim 0.18 \Omega\text{cm}^2$ at 604 °C, $\sim 6 \Omega\text{cm}^2$ at 463 °C). Furthermore, a very low activation energy of $R_{\text{surface exchange}}$ was calculated for both materials (LSC ~ 1.26 eV, LBC ~ 1.19 eV). A similar oxygen partial pressure dependency of the surface exchange resistance and degradation behavior suggests the same oxygen incorporation mechanism for both materials. The larger chemical capacitance of LBC was attributed to an increased reducibility of the perovskite lattice caused by the introduction of the larger Ba ion in comparison to Sr. The temperature dependence of the electronic conductivity was measured by van der Pauw method and revealed a maximum for LSC $\sigma_{\text{eon}} = 1028$ S/cm at ~ 382 °C and LBC 839

S/cm at ~442 °C. At all relevant temperatures, conductivity values were by far sufficient for application in SOFCs.

Finally, an AC impedance study on $\text{La}_{0.95}\text{Sr}_{0.05}\text{Ga}_{0.95}\text{Mg}_{0.05}\text{O}_{3-\delta}$ (LSGM) single crystals, a promising electrolyte material for intermediate temperature SOFC, was carried out. Impedance spectra obtained with ion blocking electrodes were quantitatively evaluated over the entire measured temperature (180 – 800 °C) and oxygen partial pressure ($p\text{O}_2$) range (0.21 to 1013 mbar) by a general equivalent circuit model applicable to mixed conductors. The excellent agreement between fit and experimental data allowed determination of the ionic and electronic conductivity, the chemical capacitance and the oxygen chemical diffusion coefficient from a single impedance spectrum. Activation energies for the electronic (0.89 eV) and ionic transport (0.95 eV at low and 0.56 eV at high temperatures) were calculated. Partial pressure as well as temperature dependence of the chemical capacitance suggest existence of trapped electronic defects and further defect chemical complexities. The p-type conductivity, on the other hand, was almost exactly proportional to $p\text{O}_2^{1/4}$ in the range of 10^{-4} to 1 bar oxygen partial pressure and thus shows impressive agreement with ideal dilute defect chemical models. Hebb-Wagner type DC polarization experiments yielded a p- and n-type conductivity of $\sim 2.2 \cdot 10^{-4} \text{ S} \cdot \text{cm}^{-1}$ and $\sim 4.0 \cdot 10^{-14} \text{ S} \cdot \text{cm}^{-1}$ respectively at 600 °C and 0.21 bar $p\text{O}_2$. DC results are in excellent agreement with those determined by the AC experiments under the same conditions. This supports the supposed reliability of the AC method to precisely determine electronic conductivities.

Bibliography

1. S. J. Davis, K. Caldeira, and H. D. Matthews, *Science*, **329** (5997), 1330-1333 (2010).
2. M. S. Dresselhaus and I. L. Thomas, *Nature*, **414** (6861), 332-337 (2001).
3. A. B. Stambouli and E. Traversa, *Renewable and Sustainable Energy Reviews*, **6** (5), 433-455 (2002).
4. E. D. Wachsman, C. A. Marlowe, and K. T. Lee, *Energy & Environmental Science*, **5** (2), 5498-5509 (2012).
5. A. Choudhury, H. Chandra, and A. Arora, *Renewable and Sustainable Energy Reviews*, **20** 430-442 (2013).
6. N. Mahato, A. Banerjee, A. Gupta, S. Omar, and K. Balani, *Progress in Materials Science*, **72** 141-337 (2015).
7. K. Huang and J. B. Goodenough, *Solid oxide fuel cell technology: principles, performance and operations*, Elsevier (2009).
8. S. C. Singhal, *The Electrochemical Society Interface*, **16** (4), 41 (2007).
9. M. Bertoldi, O. Bucheli, S. Modena, D. Larrain, and A. Ravagni, *ECS Transactions*, **35** (1), 127-138 (2011).
10. T. Ishikawa, in "23rd World Gas Conference, Amsterdam", 2006.
11. S. Shaffer, in "Ninth Annual SECA Workshop, Pittsburgh, PA", 2008.
12. P. Singh and R. A. George. Google Patents, 1997.
13. O. Posdziech, B. Mai, C. Wunderlich, and S. Voss, in "International Gas Union Research Conference", p. 1 - 17, 2011.
14. K. Huang and S. C. Singhal, *Journal of Power Sources*, **237** 84-97 (2013).
15. N. Brandon, A. Blake, D. Corcoran, D. Cumming, A. Duckett, K. El-Koury, D. Haigh, C. Kidd, R. Leah, and G. Lewis, *Journal of Electrochemical Energy Conversion and Storage*, **1** (1), 61-65 (2004).
16. R. Barfod, A. Hagen, S. Ramousse, P. V. Hendriksen, and M. Mogensen, *Fuel Cells*, **6** (2), 141-145 (2006).
17. T. M. Huber, M. Kubicek, A. K. Opitz, and J. Fleig, *Journal of The Electrochemical Society*, **162** (3), F229-F242 (2015).
18. B. Yildiz, S. McEuen, and Y. Shao-Horn, *Journal of The Electrochemical Society*, **154** (4), B427-B438 (2007).
19. F. S. Baumann, J. Fleig, H. U. Habermeier, and J. Maier, *Solid State Ionics*, **177** (35-36), 3187-3191 (2006).
20. A. Weber and E. Ivers-Tiffée, *Journal of Power Sources*, **127** (1-2), 273-283 (2004).
21. F. S. Baumann, J. Fleig, G. Cristiani, B. Stuhlhofer, H.-U. Habermeier, and J. Maier, *Journal of The Electrochemical Society*, **154** (9), B931-B941 (2007).

22. S. Kogler, A. Nenning, G. M. Rupp, A. K. Opitz, and J. Fleig, *Journal of The Electrochemical Society*, **162** (3), F317-F326 (2015).
23. W. Jung and H. L. Tuller, *ECS Transactions*, **35** (1), 2129-2136 (2011).
24. S. J. McPhail, L. Leto, and C. Boigues-Muñoz, *The Yellow Pages of SOFC Technology* ENEA - Italian National Agency for New Technologies, Energy and Sustainable Economic Development (2013).
25. S. Miyoshi, A. Takeshita, S. Okada, and S. Yamaguchi, *Solid State Ionics*, **285** 202-208 (2016).
26. L. Wang, R. Merkle, and J. Maier, *Journal of The Electrochemical Society*, **157** (12), B1802-B1808 (2010).
27. S. B. Adler, X. Y. Chen, and J. R. Wilson, *Journal of Catalysis*, **245** (1), 91-109 (2007).
28. L. Wang, R. Merkle, Y. A. Mastrikov, E. A. Kotomin, and J. Maier, *Journal of Materials Research*, **27** (15), 2000-2008 (2012).
29. A.-K. Huber, M. Falk, M. Rohnke, B. Luerssen, M. Amati, L. Gregoratti, D. Hesse, and J. Janek, *Journal of Catalysis*, **294** 79-88 (2012).
30. W. Wang and S. P. Jiang, *Solid State Ionics*, **177** (15–16), 1361-1369 (2006).
31. M. Kubicek, A. Limbeck, T. Fromling, H. Hutter, and J. Fleig, *Journal of The Electrochemical Society*, **158** (6), B727-B734 (2011).
32. Z. Cai, M. Kubicek, J. Fleig, and B. Yildiz, *Chemistry of Materials*, **24** (6), 1116-1127 (2012).
33. F. S. Baumann, J. Fleig, M. Konuma, U. Starke, H. Habermeyer, and J. Maier, *Journal of The Electrochemical Society*, **152** (10), A2074-A2079 (2005).
34. Y. Chen, W. Jung, Z. Cai, J. J. Kim, H. L. Tuller, and B. Yildiz, *Energy & Environmental Science*, **5** (7), 7979-7988 (2012).
35. W. Jung and H. L. Tuller, *Energy & Environmental Science*, **5** (1), 5370-5378 (2012).
36. Y.-M. Kim, X. Chen, S. P. Jiang, and J. Bae, *Journal of The Electrochemical Society*, **159** (2), B185-B194 (2011).
37. E. Bucher, W. Sitte, F. Klauser, and E. Bertel, *Solid State Ionics*, **208** 43-51 (2012).
38. E. Bucher, C. Gspan, F. Hofer, and W. Sitte, *Solid State Ionics*, **238** 15-23 (2013).
39. Y. Yu, H. Luo, D. Cetin, X. Lin, K. Ludwig, U. Pal, S. Gopalan, and S. Basu, *Applied Surface Science*, **323** 71-77 (2014).
40. E. Bucher, C. Gspan, F. Hofer, and W. Sitte, *Solid State Ionics*, **230** 7-11 (2013).
41. E. Bucher, M. Yang, and W. Sitte, *Journal of The Electrochemical Society*, **159** (5), B592-B596 (2012).
42. W. Lee, J. W. Han, Y. Chen, Z. Cai, and B. Yildiz, *Journal of the American Chemical Society*, **135** (21), 7909-7925 (2013).
43. W. Lee and B. Yildiz, *ECS Transactions*, **57** (1), 2115-2123 (2013).
44. Y.-L. Lee and D. Morgan, *ECS Transactions*, **25** (2), 2769-2774 (2009).

45. E. Mutoro, E. J. Crumlin, M. D. Biegalski, H. M. Christen, and Y. Shao-Horn, *Energy & Environmental Science*, **4** 3689-3696 (2011).
46. P. A. W. van der Heide, *Surface and Interface Analysis*, **33** (5), 414-425 (2002).
47. C. R. Kreller, T. J. McDonald, S. B. Adler, E. J. Crumlin, E. Mutoro, S. J. Ahn, G. J. la O', Y. Shao-Horn, M. D. Biegalski, H. M. Christen, R. R. Chater, and J. A. Kilner, *Journal of The Electrochemical Society*, **160** (9), F931-F942 (2013).
48. H. Tellez, J. Druce, J. A. Kilner, and T. Ishihara, *Faraday Discussions*, **182** 145-157 (2015).
49. H. Wang, K. J. Yakal-Kremiski, T. Yeh, G. M. Rupp, A. Limbeck, J. Fleig, and S. A. Barnett, *Journal of The Electrochemical Society*, **163** (6), F581-F585 (2016).
50. G. M. Rupp, A. Limbeck, M. Kubicek, A. Penn, M. Stoger-Pollach, G. Friedbacher, and J. Fleig, *Journal of Materials Chemistry A*, **2** (19), 7099-7108 (2014).
51. W. Lee, Z. Cai, and B. Yildiz, *ECS Transactions*, **45** (1), 405-412 (2012).
52. Q.-H. Wu, M. Liu, and W. Jaegermann, *Materials Letters*, **59** (16), 1980-1983 (2005).
53. S. P. Simner, M. D. Anderson, M. H. Engelhard, and J. W. Stevenson, *Electrochemical and Solid-State Letters*, **9** (10), A478-A481 (2006).
54. K. Szot, M. Pawelczyk, J. Herion, C. Freiburg, J. Albers, R. Waser, J. Hulliger, J. Kwapulinski, and J. Dec, *Appl. Phys. A*, **62** (4), 335-343 (1996).
55. P. Hjalmarsson, M. Søgaaard, and M. Mogensen, *Solid State Ionics*, **179** (27), 1422-1426 (2008).
56. M. Kubicek, G. M. Rupp, S. Huber, A. Penn, A. K. Opitz, J. Bernardi, M. Stoger-Pollach, H. Hutter, and J. Fleig, *Physical Chemistry Chemical Physics*, **16** (6), 2715-2726 (2014).
57. M. R. Baklanov, K. P. Mogilnikov, V. G. Polovinkin, and F. N. Dultsev, *Journal of Vacuum Science & Technology B: Microelectronics and Nanometer Structures*, **18** (3), 1385-1391 (2000).
58. P. Gilbert, *Journal of Theoretical Biology*, **36** (1), 105-117 (1972).
59. L. Dieterle, P. Bockstaller, D. Gerthsen, J. Hayd, E. Ivers-Tiffée, and U. Guntow, *Advanced Energy Materials*, **1** (2), 249-258 (2011).
60. P. Plonczak, A. Bieberle-Hütter, M. Søgaaard, T. Ryll, J. Martynczuk, P. V. Hendriksen, and L. J. Gauckler, *Advanced Functional Materials*, **21** (14), 2764-2775 (2011).
61. J. Fleig, F. S. Baumann, V. Brichzin, H. R. Kim, J. Jamnik, G. Cristiani, H. U. Habermeier, and J. Maier, *Fuel Cells*, **6** (3-4), 284-292 (2006).
62. M. P. Pechini, (S. E. Co, ed.), Vol. US3330697 A, USA, 1967.
63. J. Januschewsky, M. Ahrens, A. K. Opitz, F. Kubel, and J. Fleig, *Advanced Functional Materials*, **19** (19), 3151-3156 (2009).
64. A. K. Opitz and J. Fleig, *Solid State Ionics*, **181** (15-16), 684-693 (2010).
65. F. S. Baumann, J. Fleig, H. Habermeier, and J. Maier, *Solid State Ionics*, **177** (11-12), 1071-1081 (2006).
66. A. Ringuedé and J. Fouletier, *Solid State Ionics*, **139** (3-4), 167-177 (2001).
67. J. Jamnik and J. Maier, *Physical Chemistry Chemical Physics*, **3** (9), 1668-1678 (2001).

68. A. Penn, in "Transmission Electron Microscopic Analysis of $\text{La}_{0.6}\text{Sr}_{0.4}\text{CO}_{3-\delta}$ Thin Film Cathodes for Solid Oxide Fuel Cells, Deposited with Pulsed Laser Deposition Technique", p. 83 master thesis. Vienna University of Technology, Vienna, Austria, 2012
69. J. A. Thornton, *Journal of Vacuum Science and Technology*, **11** (4), 666-670 (1974).
70. A. Infortuna, A. S. Harvey, and L. J. Gauckler, *Advanced Functional Materials*, **18** (1), 127-135 (2008).
71. L. Dong, R. W. Smith, and D. J. Srolovitz, *Journal of Applied Physics*, **80** (10), 5682-5690 (1996).
72. A. Limbeck, G. M. Rupp, M. Kubicek, H. Tellez, J. Druce, T. Ishihara, J. A. Kilner, and J. Fleig, *Journal of Analytical Atomic Spectrometry*, (2016).
73. A. S. Bhalla, R. Guo, and R. Roy, *Mat Res Innovat*, **4** (1), 3-26 (2000).
74. M. B. Gawande, R. K. Pandey, and R. V. Jayaram, *Catalysis Science & Technology*, **2** (6), 1113-1125 (2012).
75. I. E. Wachs, *Catalysis Today*, **100** (1-2), 79-94 (2005).
76. S. Royer, D. Duprez, F. Can, X. Courtois, C. Batiot-Dupeyrat, S. Laassiri, and H. Alamdari, *Chemical Reviews*, **114** (20), 10292-10368 (2014).
77. G. Friedbacher and H. Bubert, *Surface and Thin Film Analysis: A Compendium of Principles, Instrumentation, and Applications, Second Edition*, (2011).
78. T. Nelis and J. Pallosi, *Applied Spectroscopy Reviews*, **41** (3), 227-258 (2006).
79. B. Fernández, R. Pereiro, and A. Sanz-Medel, *Analytica Chimica Acta*, **679** (1-2), 7-16 (2010).
80. J. Pisonero, J. Koch, M. Wälle, W. Hartung, N. D. Spencer, and D. Günther, *Analytical Chemistry*, **79** (6), 2325-2333 (2007).
81. B. Hattendorf, J. Pisonero, D. Günther, and N. Bordel, *Analytical Chemistry*, **84** (20), 8771-8776 (2012).
82. S. B. Desu and D. A. Payne, *Journal of the American Ceramic Society*, **73** (11), 3391-3397 (1990).
83. H. Wang, Y. Zhu, R. Tan, and W. Yao, *Catalysis Letters*, **82** (3-4), 199-204 (2002).
84. A. Yan, V. Maragou, A. Arico, M. Cheng, and P. Tsiakaras, *Applied Catalysis B: Environmental*, **76** (3-4), 320-327 (2007).
85. Y. Nishihata, J. Mizuki, T. Akao, H. Tanaka, M. Uenishi, M. Kimura, T. Okamoto, and N. Hamada, *Nature*, **418** (6894), 164-167 (2002).
86. W. Kobsiriphat, B. D. Madsen, Y. Wang, M. Shah, L. D. Marks, and S. A. Barnett, *Journal of The Electrochemical Society*, **157** (2), B279-B284 (2010).
87. S. B. Adler, *Chemical reviews*, **104** (10), 4791-4844 (2004).
88. R. M. Ormerod, *Chemical Society Reviews*, **32** (1), 17-28 (2003).
89. F. Zhao, R. Peng, and C. Xia, *Fuel Cells Bulletin*, **2008** (2), 12-16 (2008).
90. H. Yokokawa, H. Tu, B. Iwanschitz, and A. Mai, *Journal of Power Sources*, **182** (2), 400-412 (2008).

91. V. I. Sharma and B. Yildiz, *Journal of The Electrochemical Society*, **157** (3), B441-B448 (2010).
92. A. Limbeck, C. Wagner, B. Lendl, and A. Mukhtar, *Analytica Chimica Acta*, **750** 111-119 (2012).
93. J. Druce, H. Tellez, M. Burriel, M. D. Sharp, L. J. Fawcett, S. N. Cook, D. S. McPhail, T. Ishihara, H. H. Brongersma, and J. A. Kilner, *Energy & Environmental Science*, **7** (11), 3593-3599 (2014).
94. J. Buanuam, K. Tiptanasup, J. Shiowatana, M. Miro, and E. Harald Hansen, *Journal of Environmental Monitoring*, **8** (12), 1248-1254 (2006).
95. D. Das, M. Dutta, M. L. Cervera, and M. de la Guardia, *TrAC Trends in Analytical Chemistry*, **33** 35-45 (2012).
96. P. Galler, A. Limbeck, S. F. Boulyga, G. Stingeder, T. Hirata, and T. Prohaska, *Analytical Chemistry*, **79** (13), 5023-5029 (2007).
97. J. Pisonero, N. Bordel, C. Gonzalez de Vega, B. Fernández, R. Pereiro, and A. Sanz-Medel, *Anal Bioanal Chem*, **405** (17), 5655-5662 (2013).
98. J. S. Fletcher and J. C. Vickerman, *Analytical Chemistry*, **85** (2), 610-639 (2013).
99. A. Gutierrez-Gonzalez, C. Gonzalez-Gago, J. Pisonero, N. Tibbetts, A. Menendez, M. Velez, and N. Bordel, *Journal of Analytical Atomic Spectrometry*, **30** (1), 191-197 (2015).
100. G. M. Rupp, H. Tellez, J. Druce, A. Limbeck, T. Ishihara, J. Kilner, and J. Fleig, *Journal of Materials Chemistry A*, **3** (45), 22759-22769 (2015).
101. E. J. Crumlin, E. Mutoro, Z. Liu, M. E. Grass, M. D. Biegalski, Y.-L. Lee, D. Morgan, H. M. Christen, H. Bluhm, and Y. Shao-Horn, *Energy & Environmental Science*, **5** (3), 6081-6088 (2012).
102. F. S. Baumann, J. Maier, and J. Fleig, *Solid State Ionics*, **179** (21–26), 1198-1204 (2008).
103. H. Fukunaga, M. Koyama, N. Takahashi, C. Wen, and K. Yamada, *Solid State Ionics*, **132** (3–4), 279-285 (2000).
104. J. Druce, T. Ishihara, and J. Kilner, *Solid State Ionics*, **262** 893-896 (2014).
105. H. Téllez, J. Druce, Y.-W. Ju, J. Kilner, and T. Ishihara, *International Journal of Hydrogen Energy*, **39** (35), 20856-20863 (2014).
106. M. de Ridder, R. G. van Welzenis, and H. H. Brongersma, *Surface and Interface Analysis*, **33** (4), 309-317 (2002).
107. H. Ullmann, N. Trofimenko, F. Tietz, D. Stöver, and A. Ahmad-Khanlou, *Solid State Ionics*, **138** (1–2), 79-90 (2000).
108. A. J. Jacobson, *Chemistry of Materials*, **22** (3), 660-674 (2009).
109. J. H. Lee, G. Luo, I. C. Tung, S. H. Chang, Z. Luo, M. Malshe, M. Gadre, A. Bhattacharya, S. M. Nakhmanson, J. A. Eastman, H. Hong, J. Jellinek, D. Morgan, D. D. Fong, and J. W. Freeland, *Nature Materials*, **13** (9), 879-883 (2014).
110. D. E. E. Deacon-Smith, D. O. Scanlon, C. R. A. Catlow, A. A. Sokol, and S. M. Woodley, *Advanced Materials*, **26** (42), 7252-7256 (2014).

111. E. Bucher, A. Egger, G. B. Caraman, and W. Sitte, *Journal of The Electrochemical Society*, **155** (11), B1218-B1224 (2008).
112. A. Berenov, A. Atkinson, J. Kilner, M. Ananyev, V. Eremin, N. Porotnikova, A. Farlenkov, E. Kurumchin, H. J. M. Bouwmeester, E. Bucher, and W. Sitte, *Solid State Ionics*, **268, Part A** 102-109 (2014).
113. M. Kubicek, T. M. Huber, A. Welzl, A. Penn, G. M. Rupp, J. Bernardi, M. Stöger-Pollach, H. Hutter, and J. Fleig, *Solid State Ionics*, **256** 38-44 (2014).
114. P. M. Raccach and J. B. Goodenough, *Physical Review*, **155** (3), 932-943 (1967).
115. M. Sjøgaard, P. V. Hendriksen, M. Mogensen, F. W. Poulsen, and E. Skou, *Solid State Ionics*, **177** (37-38), 3285-3296 (2006).
116. M. Lankhorst and J. Ten Elshof, *Journal of Solid State Chemistry*, **130** (2), 302-310 (1997).
117. B. Hu, M. K. Mahapatra, and P. Singh, *Journal of the Ceramic Society of Japan*, **123** (1436), 199-204 (2015).
118. D. Oh, D. Gostovic, and E. D. Wachsman, *Journal of Materials Research*, **27** (15), 1992-1999 (2012).
119. N. Tsvetkov, Q. Lu, L. Sun, E. J. Crumlin, and B. Yildiz, *Nat Mater*, **advance online publication** (2016).
120. G. M. Rupp, A. Schmid, A. Nennung, and J. Fleig, *Journal of The Electrochemical Society*, **163** (6), F564-F573 (2016).
121. J. Maier, *Physical chemistry of ionic materials: ions and electrons in solids*, John Wiley & Sons (2004).
122. M. Kubicek, Z. Cai, W. Ma, B. Yildiz, H. Hutter, and J. Fleig, *ACS Nano*, **7** (4), 3276-3286 (2013).
123. Y. Chen, H. Téllez, M. Burriel, F. Yang, N. Tsvetkov, Z. Cai, D. W. McComb, J. A. Kilner, and B. Yildiz, *Chemistry of Materials*, **27** (15), 5436-5450 (2015).
124. M. B. Mogensen, C. Chatzichristodoulou, C. Graves, K. V. Hansen, K. K. Hansen, A. Hauch, T. Jacobsen, and K. Norrman, *ECS Transactions*, **72** (7), 93-103 (2016).
125. A. Tarancón, M. Burriel, J. Santiso, S. J. Skinner, and J. A. Kilner, *Journal of Materials chemistry*, **20** (19), 3799-3813 (2010).
126. D. J. Brett, A. Atkinson, N. P. Brandon, and S. J. Skinner, *Chemical Society Reviews*, **37** (8), 1568-1578 (2008).
127. C. Endler-Schuck, in "Schriften des Instituts für Werkstoffe der Elektrotechnik", Vol. PhD, p. 187. Karlsruher Institut für Technologie, Karlsruhe, 2011.
128. M. Kuhn, Y. Fukuda, S. Hashimoto, K. Sato, K. Yashiro, and J. Mizusaki, *Journal of The Electrochemical Society*, **160** (1), F34-F42 (2013).
129. J. Mizusaki, J. Tabuchi, T. Matsuura, S. Yamauchi, and K. Fueki, *Journal of The Electrochemical Society*, **136** (7), 2082-2088 (1989).
130. J. W. Stevenson, T. R. Armstrong, R. D. Carneim, L. R. Pederson, and W. J. Weber, *Journal of The Electrochemical Society*, **143** (9), 2722-2729 (1996).
131. Y. Shao-Horn, *Journal of The Electrochemical Society*, **156** (7), B816-B824 (2009).

132. J. Mizusaki, T. Sasamoto, W. R. Cannon, and H. Bowen, *Journal of the American Ceramic Society*, **66** (4), 247-252 (1983).
133. K. Yashiro, I. Nakano, M. Kuhn, S. Hashimoto, K. Sato, and J. Mizusaki, *ECS Transactions*, **35** (1), 1899-1907 (2011).
134. J. A. Kilner, R. A. De Souza, and I. C. Fullarton, *Solid State Ionics*, **86–88, Part 2** 703-709 (1996).
135. R. Shannon, *Acta Crystallographica Section A*, **32** (5), 751-767 (1976).
136. J. J. Kim, M. Kuhn, S. R. Bishop, and H. L. Tuller, *Solid State Ionics*, **230** 2-6 (2013).
137. M. Kuhn, J. J. Kim, S. R. Bishop, and H. L. Tuller, *Chemistry of Materials*, **25** (15), 2970-2975 (2013).
138. M. Koyama, C. j. Wen, and K. Yamada, *Journal of The Electrochemical Society*, **147** (1), 87-91 (2000).
139. R. Amin and K. Karan, *Journal of The Electrochemical Society*, **157** (2), B285-B291 (2010).
140. C. Setevich, F. Prado, and D. Z. de Florio, *International Journal of Hydrogen Energy*, **39** (16), 8738-8743 (2014).
141. C. Setevich, L. Mogni, A. Caneiro, and F. Prado, *Journal of The Electrochemical Society*, **159** (1), B72-B79 (2011).
142. T. Ishihara, S. Fukui, H. Nishiguchi, and Y. Takita, *Solid State Ionics*, **152–153** 609-613 (2002).
143. S. Pang, X. Jiang, X. Li, Q. Wang, and Z. Su, *International Journal of Hydrogen Energy*, **37** (3), 2157-2165 (2012).
144. L. J. van der Pauw, *Philips Res. Rep.*, **13** 1-9 (1958).
145. S.-i. Hashimoto, Y. Fukuda, M. Kuhn, K. Sato, K. Yashiro, and J. Mizusaki, *Solid State Ionics*, **186** (1), 37-43 (2011).
146. V. M. Goldschmidt, *Naturwissenschaften*, **14** (21), 477-485 (1926).
147. G. J. la O' and Y. Shao-Horn, *Journal of The Electrochemical Society*, **156** (7), B816-B824 (2009).
148. J. R. Wilson, M. Sase, T. Kawada, and S. B. Adler, *Electrochemical and Solid-State Letters*, **10** (5), B81-B86 (2007).
149. Y. L. Yang, C. L. Chen, S. Y. Chen, C. W. Chu, and A. J. Jacobson, *Journal of The Electrochemical Society*, **147** (11), 4001-4007 (2000).
150. M. Gerstl, E. Navickas, G. Friedbacher, F. Kubel, M. Ahrens, and J. Fleig, *Solid State Ionics*, **185** (1), 32-41 (2011).
151. P. S. Manning, J. D. Sirman, R. A. De Souza, and J. A. Kilner, *Solid State Ionics*, **100** (1–2), 1-10 (1997).
152. W. Sitte, E. Bucher, and W. Preis, *Solid State Ionics*, **154–155** 517-522 (2002).
153. J. Mizusaki, Y. Mima, S. Yamauchi, K. Fueki, and H. Tagawa, *Journal of Solid State Chemistry*, **80** (1), 102-111 (1989).

154. D. Marrocchelli, S. R. Bishop, H. L. Tuller, and B. Yildiz, *Advanced Functional Materials*, **22** (9), 1958-1965 (2012).
155. M. H. Lankhorst, H. Bouwmeester, and H. Verweij, *Journal of Solid State Chemistry*, **133** (2), 555-567 (1997).
156. T. Kawada, J. Suzuki, M. Sase, A. Kaimai, K. Yashiro, Y. Nigara, J. Mizusaki, K. Kawamura, and H. Yugami, *Journal of The Electrochemical Society*, **149** (7), E252-E259 (2002).
157. M. Kuhn, S. Hashimoto, K. Sato, K. Yashiro, and J. Mizusaki, *Journal of Solid State Chemistry*, **197** 38-45 (2013).
158. T. Z. Ding, Y. M. Wang, and S. H. Shi, *Journal of Materials Science Letters*, **22** (1), 1-3 (2003).
159. J. H. Joo, R. Merkle, J.-H. Kim, and J. Maier, *Advanced Materials*, **24** (48), 6507-6512 (2012).
160. K. Huang, R. S. Tichy, and J. B. Goodenough, *Journal of the American Ceramic Society*, **81** (10), 2576-2580 (1998).
161. C. Zuo, S. Zha, M. Liu, M. Hatano, and M. Uchiyama, *Advanced Materials*, **18** (24), 3318-3320 (2006).
162. B. C. H. Steele and A. Heinzl, *Nature*, **414** (6861), 345-352 (2001).
163. T. Ishihara, H. Matsuda, and Y. Takita, *Journal of the American Chemical Society*, **116** (9), 3801-3803 (1994).
164. J.-H. Kim and H.-I. Yoo, *Solid State Ionics*, **140** (1), 105-113 (2001).
165. C. Oncel, B. Ozkaya, and M. A. Gulgun, *Journal of the European Ceramic Society*, **27** (2-3), 599-604 (2007).
166. M. Kurumada, E. Iguchi, and D. I. Savytskii, *Journal of Applied Physics*, **100** (1), 014107 (2006).
167. L. Cong, T. He, Y. Ji, P. Guan, Y. Huang, and W. Su, *Journal of Alloys and Compounds*, **348** (1-2), 325-331 (2003).
168. B. Rambabu, S. Ghosh, W. Zhao, and H. Jena, *Journal of Power Sources*, **159** (1), 21-28 (2006).
169. Z.-C. Li, H. Zhang, B. Bergman, and X. Zou, *Journal of the European Ceramic Society*, **26** (12), 2357-2364 (2006).
170. V. Thangadurai and W. Weppner, *Electrochimica Acta*, **50** (9), 1871-1877 (2005).
171. L. Vasylechko, V. Vashook, D. Savytskii, A. Senyshyn, R. Niewa, M. Knapp, H. Ullmann, M. Berkowski, A. Matkovskii, and U. Bismayer, *Journal of Solid State Chemistry*, **172** (2), 396-411 (2003).
172. T. Van Dijk and A. Burggraaf, *physica status solidi (a)*, **63** (1), 229-240 (1981).
173. J. C. C. Abrantes, J. A. Labrincha, and J. R. Frade, *Journal of the European Ceramic Society*, **20** (10), 1603-1609 (2000).
174. J. Fleig and J. Maier, *Physical Chemistry Chemical Physics*, **1** (14), 3315-3320 (1999).
175. W. Lai and S. M. Haile, *Journal of the American Ceramic Society*, **88** (11), 2979-2997 (2005).
176. J.-S. Lee, J. Jamnik, and J. Maier, *Monatshefte für Chemie - Chemical Monthly*, **140** (9), 1113-1119 (2009).

177. A. K. Opitz, A. Lutz, M. Kubicek, F. Kubel, H. Hutter, and J. Fleig, *Electrochimica Acta*, **56** (27), 9727-9740 (2011).
178. D. I. Savytskii, D. M. Trots, L. O. Vasylechko, N. Tamura, and M. Berkowski, *Journal of Applied Crystallography*, **36** (5), 1197-1203 (2003).
179. V. Stancovski, S. Sridhar, and U. B. Pal, *Journal of Electroceramics*, **3** (3), 279-299 (1999).
180. R. J. Berry, *Surface Science*, **76** (2), 415-442 (1978).
181. J. Fleig, *Solid State Ionics*, **150** (1-2), 181-193 (2002).
182. K. Huang, R. S. Tichy, and J. B. Goodenough, *Journal of the American Ceramic Society*, **81** (10), 2565-2575 (1998).
183. M. Saiful Islam, *Journal of Materials chemistry*, **10** (4), 1027-1038 (2000).
184. J. Maier, *Berichte der Bunsengesellschaft für physikalische Chemie*, **90** (1), 26-33 (1986).
185. R. T. Baker, B. Gharbage, and F. M. B. Marques, *Journal of The Electrochemical Society*, **144** (9), 3130-3135 (1997).
186. P. S. Anderson, F. M. B. Marques, D. C. Sinclair, and A. R. West, *Solid State Ionics*, **118** (3-4), 229-239 (1999).
187. V. Kharton, A. Yaremchenko, A. Viskup, G. Mather, E. Naumovich, and F. Marques, *Solid State Ionics*, **128** (1), 79-90 (2000).
188. J. Jamnik and J. Maier, *Journal of The Electrochemical Society*, **146** (11), 4183-4188 (1999).
189. C. Wagner, *Zeitschrift für Elektrochemie, Berichte der Bunsengesellschaft für physikalische Chemie*, **60** (1), 4-7 (1956).
190. M. H. Hebb, *The Journal of Chemical Physics*, **20** (1), 185-190 (1952).
191. J. H. Jang and G. M. Choi, *High Temperature Materials Proceedings*, **5** 97-105 (2002).

List of abbreviations

450 ^{0.4} / 450 ^{0.04}	polycrystalline dense La _{0.6} Sr _{0.4} CoO _{3-δ} thin films deposited at 450 °C in 0.4 mbar or 0.04 mbar oxygen partial pressure, respectively
AC	alternating current
AES	Auger electron spectroscopy
AFM	atomic force microscopy
APU	auxiliary power unit
BSCF	Ba _{1-x} Sr _x Co _{1-y} Fe _y O _{3-δ}
CE	counter electrode
CHP	combined heating and power
CMO	Complex metal oxide
DC	direct current
DHM	digital holographic microscopy
FESEM	field emission scanning electron microscopy
FI	flow injection
GADDS	general area detector diffraction system
GDC	Ce _x Gd _{1-x} O _{2-δ} (with x = 0.2 in most specific cases)
GDMS	glow discharge mass spectrometry
HAADF	high angle annular dark field
ICP-OES	inductively coupled plasma – optical emission spectrometry
ICP-MS	inductively coupled plasma – mass spectrometry
IPLD	in-situ Impedance Spectroscopy inside a pulsed laser deposition chamber
IS	impedance spectroscopy
LA-ICP-MS	laser ablation – inductively coupled plasma – mass spectrometry
LEIS	low energy ion scattering
LBC	La _{1-x} Ba _x CoO _{3-δ} (with x = 0.4 in most specific cases)
LSC	La _{1-x} Sr _x CoO _{3-δ} (with x = 0.4 in most specific cases)

LSCF	$\text{La}_x\text{Sr}_{1-x}\text{Co}_y\text{Fe}_{1-y}\text{O}_{3-\delta}$ (LSCF)
LSGM	$\text{La}_{1-x}\text{Sr}_x\text{Ga}_{1-y}\text{Mg}_y\text{O}_{3-\delta}$ (with $x = 0.05$ and $y = 0.05$ in most specific cases)
LSM	$\text{La}_{1-x}\text{Sr}_x\text{MnO}_{3-\delta}$
MIEC	mixed ionic and electronic conductor
ORR	oxygen reduction reaction (= oxygen exchange reaction in AC experiments)
PLD	pulsed laser deposition
PTFE	polytetrafluoroethylene
rms	root mean square
RBS	Rutherford backscattering
SIMS	secondary ion mass spectrometry
SFO	$\text{SrFeO}_{3-\delta}$
SOEC	solid oxide electrolysis cells
SOFC	solid oxide fuel cell
SSC	$\text{Sm}_{1-x}\text{Sr}_x\text{CoO}_{3-\delta}$
STF	$\text{SrTi}_{1-y}\text{Fe}_y\text{O}_{3-\delta}$
SZM	structure zone model
TEM	transmission electron microscopy
WE	working electrode
XPS	X-ray photoelectron spectroscopy
YSZ	yttria stabilized zirconia (9.5 mol% Y_2O_3)

List of symbols

$(100), (xxx)$	plane orthogonal to crystal lattice vector
2θ	scattering angle in diffraction experiments (source – detector)
a, b, c	lattice parameter
a_{pc}	pseudo cubic lattice parameter
A, B-site	A or B site of the perovskite ABO_3 lattice
A	area
C_o	oxygen lattice concentration in LSC
C_e, C_h	electron and electron hole concentration
C	capacitance
C^{dielec}	geometrical capacitance
C^{chem}	chemical capacitance
C^{int}	interfacial capacitance
CPE	constant phase element
d	thickness
D	chemical diffusion coefficient
δ	oxygen non-stoichiometry
e^-	electron
e_0	elementary charge
ϵ_0	vacuum permittivity
ϵ_r	relative permittivity
F	Faraday's constant
h^+	electron hole
I	current
λ	wavelength
ω	angular frequency
k^q	surface exchange coefficient
$O_o^x, [O_o^x]$	oxygen on regular oxygen site and its concentration

q_{\perp}, q_{\parallel}	orthogonal and in-plane component of the reciprocal space vector
r_x	ionic radii of component x
R	resistance
R_b	bulk resistance
R_{hf}	high frequency resistance
R_{ion}, R_{eon}	ionic and electronic resistance respectively
$R_s, R_{surf\ exch}, R_{surface\ exchange}$	surface exchange resistance
R_g	gas constant
R_W	Warburg resistance
σ_n, σ_p	n-type and p-type conductivity
$\sigma_{eon}, \sigma_{ion}$	electronic and ionic conductivity
t_{eon}, t_{ion}	electronic and ionic transference number
t_f	Goldschmidt's tolerance factor
T	temperature
μ_O, μ_V, μ_{eon}	chemical potential of oxygen, vacancies and electronic charge carriers
U	voltage
V	volume
V_M	molar volume of LSC
$V_{O^{\cdot\cdot}}, [V_{O^{\cdot\cdot}}]$	oxygen vacancy and its concentration
Z_x	impedance of component x (e.g. CPE, C, R)
Z', Z''	real and imaginary part of the complex number Z

Scientific publications

14. **G. M. Rupp**, A. K. Opitz, M. Kubicek, J. Fleig
Defect chemistry and oxygen exchange kinetics of growing MIEC – studied by impedance spectroscopy during pulsed laser deposition
in preparation
13. **G. M. Rupp**, A. K. Opitz, A. Nenning, A. Limbeck, J. Fleig
In-situ impedance spectroscopy revealing the strong effect of minor Sr and Co decorations on the oxygen exchange of $\text{La}_{0.6}\text{Sr}_{0.4}\text{CoO}_{3-\delta}$
Nature materials, **submitted**
12. **G. M. Rupp**, M. Glowacki, J. Fleig
Electronic and ionic conductivity of $\text{La}_{0.95}\text{Sr}_{0.05}\text{Ga}_{0.95}\text{Mg}_{0.05}\text{O}_{3-\delta}$ (LSGM) single crystals
Journal of the Electrochemical Society, **revised manuscript in review**
11. **G. M. Rupp**, A. Schmid, A. Nenning, J. Fleig
The Superior Properties of $\text{La}_{0.6}\text{Ba}_{0.4}\text{CoO}_{3-\delta}$ Thin Film Electrodes for Oxygen Exchange in Comparison to $\text{La}_{0.6}\text{Sr}_{0.4}\text{CoO}_{3-\delta}$
Journal of the Electrochemical Society, **163 (2016)**, 6; 564 – 573
10. A. Limbeck[†], **G. M. Rupp**[†], M. Kubicek, H. Téllez, J. Druce, T. Ishihara, J. A. Kilner, J. Fleig
†equal contribution
Dynamic etching of soluble surface layers with on-line inductively coupled plasma mass spectrometry detection – a novel approach for determination of complex metal oxide surface cation stoichiometry
Journal of Analytical Atomic Spectrometry, **(2016)** in press
9. J. Fleig, A. Schmid, **G. M. Rupp**, C. Slouka, E. Navickas, L. Andrejs, H. Hutter, L. Volgger, A. Nenning
The Chemical Capacitance as a Fingerprint of Defect Chemistry in Mixed Conducting Oxides
Acta Chimica Slovenica, **61 (2016)**, 1 – 10
8. H. Wang, Kyle J. Yakal-Kremiski, T. Yeh, **G. M. Rupp**, A. Limbeck, J. Fleig, W. Barnett, Scott A. Barnett
Mechanisms of Performance Degradation of $(\text{La,Sr})(\text{Co,Fe})\text{O}_{3-\delta}$ Solid Oxide Fuel Cell Cathodes
Journal of the Electrochemical Society, **163 (2016)**, 6; 581 - 585
7. S. Volkov, V. Vonk, N. Khorshidi, D. Franz, M. Kubicek, V. Kilic, R. Felici, T. M. Huber, E. Navickas, **G.M. Rupp**, J. Fleig, A. Stierle^{†‡}
Operando X-ray Investigation of Electrode/Electrolyte Interfaces in Model Solid Oxide Fuel Cells
Chemistry of Materials, **28 (2016)**, 11; 3727–3733.

6. **G. M. Rupp**, H. Tellez, J. Druce, A. Limbeck, T. Ishihara, J. Kilner, J. Fleig
Surface Chemistry of $La_{0.6}Sr_{0.4}CoO_{3-\delta}$ Thin Films and Impact on the Oxygen Surface Exchange Resistance
Journal of Materials Chemistry A, 3 (2015), 22759 - 22769.
5. E. Navickas, T. Huber, Y. Chen, W. Hetaba, G. Holzlechner, **G. M. Rupp**, M. Stöger-Pollach, G. Friedbacher, H. Hutter, B. Yildiz, J. Fleig
Fast oxygen exchange and diffusion kinetics of grain boundaries in Sr-doped $LaMnO_3$ thin films
Physical Chemistry Chemical Physics, 17 (2015), 12; 7659 - 7669.
4. S. Kogler, A. Nenning, **G. M. Rupp**, A.K. Opitz, J. Fleig
Comparison of Electrochemical Properties of $La_{0.6}Sr_{0.4}FeO_{3-\delta}$ Thin Film Electrodes: Oxidizing vs. Reducing Conditions
Journal of the Electrochemical Society, 162 (2015), 3; 317 - 326.
3. **G. M. Rupp**, A. Limbeck, M. Kubicek, A. Penn, M. Stöger-Pollach, G. Friedbacher, J. Fleig
Correlating surface cation composition and thin film microstructure with the electrochemical performance of lanthanum strontium cobaltite (LSC) electrodes
Journal of Materials Chemistry A, 2 (2014), 7099 - 7108.
2. M. Kubicek, T. Huber, A. Welzl, A. Penn, **G. M. Rupp**, J. Bernardi, M. Stöger-Pollach, H. Hutter, J. Fleig
Electrochemical properties of $La_{0.6}Sr_{0.4}CoO_{3-\delta}$ thin films investigated by complementary impedance spectroscopy and isotope exchange depth profiling
Solid State Ionics, 256 (2014), 38 - 44.
1. M. Kubicek, **G. M. Rupp**, S. Huber, A. Penn, A.K. Opitz, J. Bernardi, M. Stöger-Pollach, H. Hutter, J. Fleig
Cation diffusion in $La_{0.6}Sr_{0.4}CoO_{3-\delta}$ below 800 °C and its relevance for Sr segregation
Physical Chemistry Chemical Physics, 16 (2014), 6; 2715 - 2726.

Conference contributions

8. G. M. Rupp, H. Tellez, J. Druce, A. Limbeck, T. Ishihara, J. Kilner, J. Fleig
Surfaces Chemistry of $\text{La}_{0.6}\text{Sr}_{0.4}\text{CoO}_{3-\delta}$ Thin Films and Impact on the Oxygen Surface Exchange resistance
Oral, 20th International Conference on Solid State Ionics, **Keystone, Colorado, USA**
14.06.2015 - 19.06.2015
7. G. M. Rupp, M. Glowacki, J. Fleig
Impedance Study on LSGM Single Crystals
Poster, 20th International Conference on Solid State Ionics, **Keystone, Colorado, USA**
14.06.2015 - 19.06.2015
6. G. M. Rupp, A. Limbeck, J. Fleig
The correlation of cation segregation, film morphology and oxygen reduction reaction of $\text{La}_{0.6}\text{Sr}_{0.4}\text{CoO}_{3-\delta}$ thin films
Oral, E-MRS Spring Meeting 2014, **Lille, France**
26.05.2014 - 30.05.2014
5. G. M. Rupp, A. Limbeck, J. Fleig
 $\text{La}_{0.6}\text{Sr}_{0.4}\text{CoO}_{3-\delta}$ Fuel Cell Model Cathodes - Surface Chemistry vs. Performance
Oral, 15th Austrian Chemistry Days 2013, **Graz, Austria**
23.09.2013 - 26.09.2013
4. G. M. Rupp, M. Kubicek, A. Limbeck, J. Fleig
Influence of varying surface compositions of $\text{La}_{0.6}\text{Sr}_{0.4}\text{CoO}_{3-\delta}$ thin films on the electrochemical activity of the oxygen reduction reaction investigated by EIS and ICP-OES
Poster, E-MRS Spring Meeting 2012, **Strasbourg, France**
14.05.2012 - 18.05.2012
3. G. M. Rupp, M. Kubicek, A. Limbeck, J. Fleig
 $\text{La}_{0.6}\text{Sr}_{0.4}\text{CoO}_{3-\delta}$ Fuel Cell Model Cathodes - Surface Chemistry vs. Performance
Oral, International Forum – Topical Issues of Rational Use of Natural Resources, **St. Petersburg, Russia**
25.04.2012 - 27.04.2012
2. G. M. Rupp, M. Kubicek, A. Limbeck, J. Fleig
Fuel Cell Model Cathodes - Surface Chemistry vs. Performance
Poster/Oral, 110th Bunsentagung 2011, **Berlin, Germany**
02.06.2011 - 04.06.2011
1. G. M. Rupp, M. Kubicek, A. Limbeck, J. Fleig
Effect of varying surface compositions of dense $\text{La}_{0.6}\text{Sr}_{0.4}\text{CoO}_{3-\delta}$ thin films on the electrochemical activity of the oxygen reduction in solid oxide fuel cells
Poster, 5th Junior Scientist Conference, **New York, USA**
13.04.2011 - 15.04.2011

Curriculum vitae

Ghislain Michel Rupp

Born on 19.10.1986 in Osnabrück, Germany
German and French citizenship

Hütteldorferstrasse 131/17
A-1140 Vienna
grupp@gmx.at / ghislain.rupp@tuwien.ac.at
+43 664 4112728

Education

PhD thesis 03/2012 – 08/2016	Vienna University of Technology, Vienna, Austria Institute of Chemical Technologies and Analytics Solid State Electrochemistry and Electroceramics Laboratory
Proj. Assistant 03/2016 – 08/2016	<i>“Oxygen transport and surface exchange kinetics in lanthanum based perovskite-type materials”</i>
Univ. Assistant 03/2012 – 03/2016	supervised by Univ. Prof. Dr. rer. nat. Jürgen Fleig

Master thesis 01/2011 – 02/2012	Vienna University of Technology, Vienna, Austria Institute of Chemical Technologies and Analytics Solid State Electrochemistry and Electroceramics Laboratory
	<i>“Relation between surface composition of (La, Sr)CoO_{3-δ} thin film electrodes and oxygen reduction kinetics”</i>
	supervised by Univ. Prof. Dr. rer. nat. Jürgen Fleig
	Master degree with distinction (1.0 \emptyset)

University 10/2005 – 02/2012	Vienna University of Technology, Vienna, Austria Faculty of Technical Chemistry (275 ECTS - 1.57 \emptyset)

High school 09/2001 – 06/2005	BORG Polgarstraße, Vienna, Austria Higher school certificate with distinction (Matura 1.0 \emptyset)

Undergraduate Internships

08/2010 – 10/2010	Tsinghua University, Beijing, China <i>“Shape controlled synthesis and electrochemical characterization of Pd nanocrystals”</i> supervised by Univ. Prof. Dr. Yadong Li
08/2009 – 10/2009	Vienna University of Technology, Vienna, Austria <i>“Synthesis of ionic liquids”</i> supervised by Univ. Prof. Dr. Peter Gärtner
06/2008	Vienna University of Technology, 1060 Vienna, Austria <i>“Electrochemical Investigations on platinum microelectrodes”</i> supervised by Univ. Prof. Dr. Jürgen Fleig
08/2007	ETH Zurich, Switzerland <i>“Preparation and characterization of micro solid oxide fuel cells”</i> supervised by Univ. Prof. Dr. Ludwig Gauckler

Grants, awards and memberships

2012 – 2016	Member of Solids4Fun Doctoral School of Vienna University of Technology
2013	Scholarship grant for PhD thesis from the chemistry faculty
2012	Master thesis award from Austrian’s chemical society (GÖCH)
2011	Best Poster Award of 110 th Bunsentagung 2011, Berlin, Germany
2011	Travelling scholarship competition to New York, USA from the Vienna University of Technology
2010	Merit-based grant (1.2 Ø) from Vienna University of Technology

Teaching Experience

2012 - 2016	Supervised 12 lab courses, including oral exams of ~400 students
2015 - 2016	Supervised master thesis of Alexander Schmid
2014	Supervised bachelor thesis of Clemens Kauffmann
2012 - 2014	Supervised project theses of 3 more students

Acknowledgments

Endlich auf Seite 145 angekommen – werden all jene denken die nicht die Arbeit von hinten aufgeschlagen, sondern den beschwerlichen Weg durch meine letzten 4 Jahre genommen haben. Zu wenig bunte Bilder, zu viel Text wird das Resümee wohl lauten und bei jenen mit einer Halbkreisphobie möchte ich mich auch direkt entschuldigen. Diese Arbeit besteht aber aus viel mehr als einem schwarz-weißen Mosaik an Wörtern und Datenpunkten. In jeder Abbildung verstecken sich Tage, Wochen manchmal sogar Monate an Arbeit, die mich für immer an all die Höhen und Tiefen meiner Dissertation erinnern werden. Freunde, Familie und Kollegen halfen durch die Durststrecken und sorgten dafür dass mein ewiger Optimismus erhalten blieb. Jetzt ist es zu Ende – es war eine unglaublich schöne und spannende Zeit mit Konferenzen, Notreparaturen (Stichwort „Gaffaband“) und Suderseminaren – ein neuer Regallückenfüller ist geschrieben.

Als erstes möchte ich mich bei dir bedanken, Jürgen. Dein ansteckender Enthusiasmus für die Elektrochemie und deine menschliche Größe und Bescheidenheit haben ein einzigartiges Arbeitsumfeld geschaffen. Danke für deine stets offene Tür, die Kilos an Graphit auf meinen Manuskripten, die zahlreichen Konferenzbesuche und vor allem die Freiheit meine Arbeit selbst zu Gestalten.

Bedanken möchte ich mich auch bei Andreas Limbeck für die tatkräftige Unterstützung während der ICP Experimente, beim Schreiben der Publikationen und seinem staubtrockenen Humor. Ein großer Dank geht auch an Werner Artner, dem guten Geist des Röntgenzentrums; Klaudia Hradil, der einzigen auf der Uni die meinen Namen richtig aussprechen konnte; Elisabeth Eitenberger, für die unzähligen gemeinsamen Stunden am SEM; John Druce, Helena Téllez und John Kilner für einen der wichtigsten Erfolge in meiner Dissertationszeit.

Ein großes Dankeschön natürlich an meine gesamte Arbeitsgruppe: Meine Bürokollegen Andreas und Alex, mit denen nie ein Auge trocken blieb; Edvinas, meinem Synchrotron Leidensgenossen; Markus dem halb-ironischen Grantler, der wohl auch über diese Zeile motschkern wird; Sandra der Laborfee, die für Recht und Ordnung unter Androhung von Kurt gesorgt hat; Kurt, der die drei Gewalten in einer Person vereint; Udo fürs Gasflaschen wechseln; Papa Alex und Mama Steffi, die das Piratenschiff auch im Sturm auf Kurs halten und für regelmäßigen Matrosennachwuchs sorgen; Christoph, weil er Christoph ist; Andreas, der verfrühten Reinkarnation des J. Maiers; Tobi, der Endgegner im neuen Plastic Planet 2, Matthias, dem es egal ist, ob jemand seine genialen

Witze versteht; Till, der wieder den Weg auf die gute Seite der Macht gefunden hat; Alex und Lukas, mit denen ich fast den TCH-Cup gewonnen hätte; David, mit dem ich den TCH-Cup gewonnen habe (lag also nicht an mir); Michi, dessen Forschung wohlriechender sein könnte; Julia, für das ein oder andere kulinarische und rhetorische Schmankerl und Gregor, Georg und Hamed, den Hütern des Lichts.

Ansonsten möchte ich mich bei all meinen Freunden, insbesondere Günther, für die immerwährende Unterstützung oder Ablenkung von der Arbeit bedanken. Ihr seid großartig. Einen großen Verdienst an dieser Arbeit und meiner Ausbildung tragen natürlich meine beiden Eltern, Marthe und Romano. Ihr habt mich zu dem wissbegierigen Menschen erzogen der ich heute bin, egal wie oft ich euch als Kind mit einem „warum?“ wohl genervt habe. Danke auch an dich Schwesterchen, unsere gemeinsamen Konferenzen werden mir wohl für immer in Erinnerung bleiben.

Mit meinen letzten Worten möchte ich dir danken, Julijana. Für deine Unterstützung, deine Geduld und dein unerschütterliches Vertrauen in mich.